Since 1955

Strojniški vestnik

Journal of Mechanical Engineering

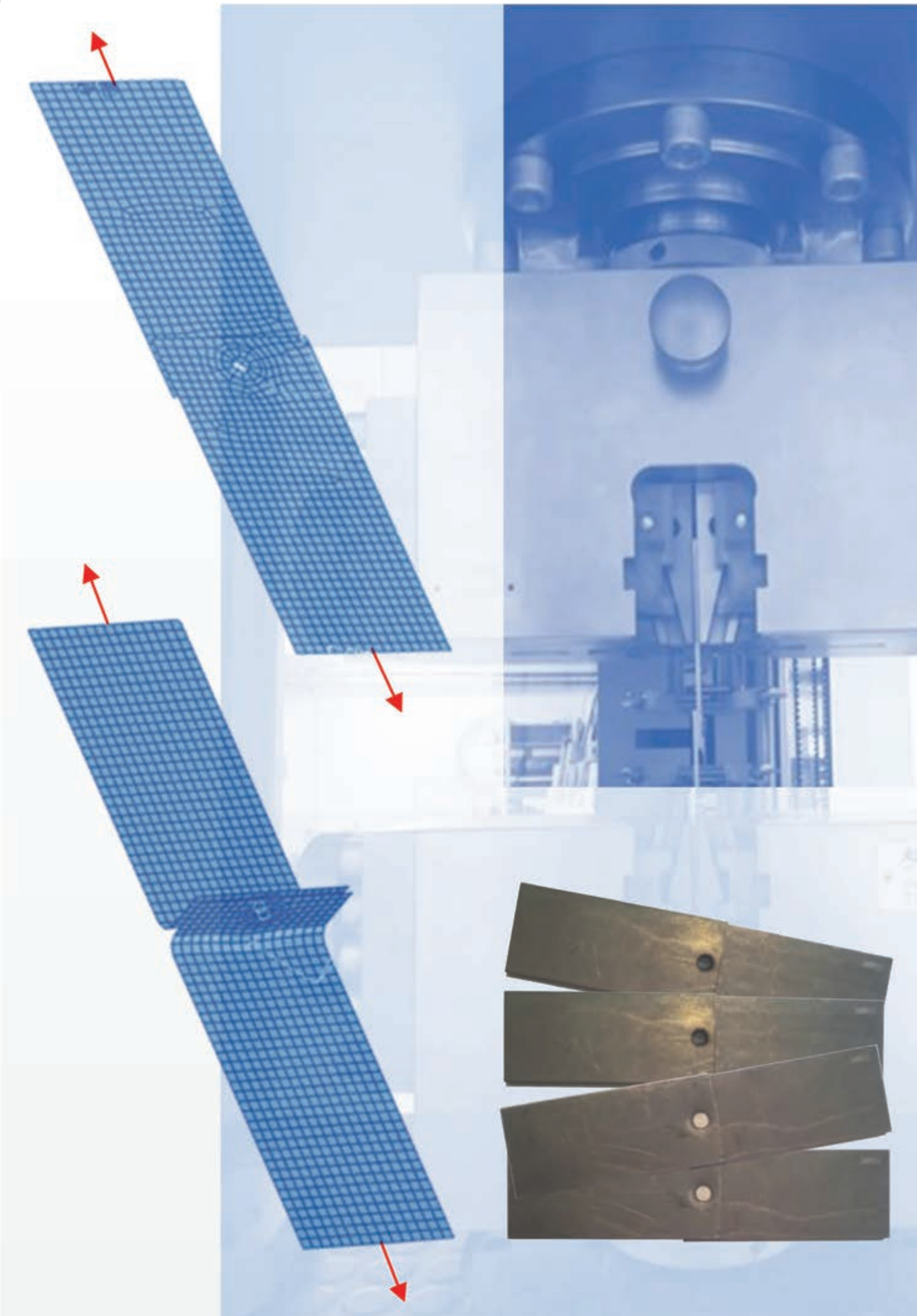

no. 1
year 2022
volume 68

Strojniški vestnik – Journal of Mechanical Engineering (SV-JME)

Aim and Scope

The international journal publishes original and (mini)review articles covering the concepts of materials science, mechanics, kinematics, thermodynamics, energy and environment, mechatronics and robotics, fluid mechanics, tribology, cybernetics, industrial engineering and structural analysis.

The journal follows new trends and progress proven practice in the mechanical engineering and also in the closely related sciences as are electrical, civil and process engineering, medicine, microbiology, ecology, agriculture, transport systems, aviation, and others, thus creating a unique forum for interdisciplinary or multidisciplinary dialogue.

The international conferences selected papers are welcome for publishing as a special issue of SV-JME with invited co-editor(s).

Editor in Chief
Vincenc Butala
University of Ljubljana, Faculty of Mechanical Engineering, Slovenia

Technical Editor
Pika Škraba
University of Ljubljana, Faculty of Mechanical Engineering, Slovenia

Founding Editor
Bojan Kraut
University of Ljubljana, Faculty of Mechanical Engineering, Slovenia

Editorial Office
University of Ljubljana, Faculty of Mechanical Engineering
SV-JME, Aškerčeva 6, SI-1000 Ljubljana, Slovenia
Phone: 386 (0)1 4771 137
Fax: 386 (0)1 2518 567
info@sv-jme.eu, http://www.sv-jme.eu

Print: Demat d.o.o., printed in 250 copies

Founders and Publishers
University of Ljubljana, Faculty of Mechanical Engineering, Slovenia
University of Maribor, Faculty of Mechanical Engineering, Slovenia
Association of Mechanical Engineers of Slovenia
Chamber of Commerce and Industry of Slovenia, Metal Processing Industry Association

President of Publishing Council
Mihael Sekavčnik
University of Ljubljana, Faculty of Mechanical Engineering, Slovenia

Vice-President of Publishing Council
Bojan Dolšak
University of Maribor, Faculty of Mechanical Engineering, Slovenia

Cover:
Numerical and physical models of specimens with self-pivoting rivet joints and clinch joints before the simulation/testing for the determination of static properties.

Image Courtesy:
Šeruga, D., Glavan, M., Malnarič, V. & Klemenc, J., University of Ljubljana, Faculty of Mechanical Engineering, Slovenia

ISSN 0039-2480, ISSN 2536-2948 (online)

General information

Strojniški vestnik – Journal of Mechanical Engineering is published in 11 issues per year (July and August is a double issue).

Institutional prices include print & online access: institutional subscription price and foreign subscription €100,00 (the price of a single issue is €10,00); general public subscription and student subscription €50,00 (the price of a single issue is €5,00). Prices are exclusive of tax. Delivery is included in the price. The recipient is responsible for paying any import duties or taxes. Legal title passes to the customer on dispatch by our distributor. Single issues from current and recent volumes are available at the current single-issue price. To order the journal, please complete the form on our website. For submissions, subscriptions and all other information please visit: *http://www.sv-jme.eu*.

You can advertise on the inner and outer side of the back cover of the journal. The authors of the published papers are invited to send photos or pictures with short explanation for cover content.

We would like to thank the reviewers who have taken part in the peer-review process.

SV-JME is indexed / abstracted in: SCI-Expanded, Compendex, Inspec, ProQuest-CSA, SCOPUS, TEMA. The list of the remaining bases, in which SV-JME is indexed, is available on the website.

The journal is subsidized by Slovenian Research Agency.

Strojniški vestnik - Journal of Mechanical Engineering is available on *https://www.sv-jme.eu*.

Contents

Strojniški vestnik - Journal of Mechanical Engineering
volume 68, (2022), number 1
Ljubljana, January 2022
ISSN 0039-2480

Published monthly

Papers

Strojniški vestnik - Journal of Mechanical Engineering 68(2022)1, 3-13
© 2022 The Authors. CC BY-NC 4.0 Int. Licensee: SV-JME
DOI:10.5545/sv-jme.2021.7329

Original Scientific Paper

Received for review: 2021-07-14
Received revised form: 2021-09-29
Accepted for publication: 2021-12-16

Incorporation of a Simplified Mechanical Joint Model into Numerical Analysis

Mitja Glavan[1] – Jernej Klemenc[2] – Vili Malnarič[1] – Domen Šeruga[2],*
[1] TPV Automotive, Slovenia
[2] University of Ljubljana, Faculty of Mechanical Engineering, Slovenia

In the development of new joining technologies, incorporation of mechanical joints in computer analyses for the evaluation of structures can be carried out by a practical, simplified mechanical joint model. Here, two most frequently used joining technologies were analysed, a self-piercing rivet joint and a clinch joint. Physical tests of static load capacity of the joints were performed and numerical models for simulations were set-up. An optimization method was designed for estimating the material parameters of the mechanical joint for the needs of numerical analyses. For optimization purposes during the plan of experiments, a range of possible parameter values was investigated using a response surface method, results of simulations, results of physical tests and a genetic algorithm. The results of simulations using the optimal values of the material parameters are comparable to the experimental observations for the both joints.

Keywords: mechanical joints, self-piercing riveting, clinch joint, FEM of mechanical joints, parameter optimization, simplified FE model, response surface, genetic algorithm

Highlights

- *Numerical model for modelling a mechanical joint has been defined.*
- *Methodology of defining the properties of material parameters in numerical analysis has been developed.*
- *The material parameters of the mechanical joint for 2 mm thick S500MC material have been defined.*
- *The developed methodology is fast and easy to use and represents a universal tool for industrial needs.*

0 INTRODUCTION

The current trend in the automotive, aerospace, nautical and other similar industries is primarily a decrease in material consumption and indirectly a reduction in the mass of these means of transportation. In this respect, today, the so-called lightweight materials such as high-strength steel, aluminium, composite materials and the use of magnesium are increasingly emerging as construction materials [1] to [3]. However, due to the different properties of these materials their joining with the traditional welding process is not possible. Today, a large number of alternative joining technologies is emerging, or is already in use, to meet the growing need in joining such materials [4] to [9]. A review of such technologies and their use can be seen in [10] to [12]. A wide range of technologies is thus in use, each with its advantages and disadvantages. The use of a particular technology hence depends on the strength requirements of the finished product, materials, the possibility of integration into production facilities and prices. Two joining technologies have been compared in our research, which possess the appropriate characteristics to represent an alternative to spot-welding. Self-piercing riveting is a technology that provides adequate static strength, i.e. load-bearing capacity of the joint and a slightly higher dynamic strength in contrast to spot welding, while the advantage of the clinch joint is a significantly higher dynamic load-bearing capacity, with the loss of a significant proportion of static load capacity [13] to [16]. Table 1 presents the comparison of the above technologies [17]. However, for a proper consideration of these technologies in numerical analyses during the pre-development and development phases of a research and development (R&D) cycle, it is necessary to develop appropriate numerical models of these joints. Moreover, knowing the exact parameters of joints contributes to reducing development costs, shorter development time and optimization of geometry before the first prototype is manufactured [18].

As numerical structural analyses are carried out way before the production of prototypes and their physical testing, accurate knowledge of material parameters of the joint plays a key role in the quality of the simulations. For example, Bouchard et al. [19] used an approach with exact modelling of the actual rivet, which produced encouraging results even in the local area around the joint. Thus, following this approach, the numerical results are well comparable to physical testing, but such a model is not suitable for large structures and serves more for the purpose of understanding what happens in the joint and its surroundings. The disadvantages of such an approach are time-consuming simulations and possible

---

*Corr. Author's Address: University of Ljubljana, Faculty of Mechanical Engineering, Slovenia, domen.seruga@fs.uni-lj.si

Table 1. *An overview and comparison of self-piercing riveting (SPR) technology and clinch joint technology (adapted from [17])*

Property	SPR	Clinching
Positioning on boreholes	No	No
Joining different materials	Yes	Yes
Joining three or more boards	Good	Poor
Sealing joint	Yes	Yes
Corrosion resistance	Good	Good
Visuality of the joint	Good	Medium
Access with the tool	Bilateral	Bilateral
Energy consumption	Low	Low
Environmental impact	Small	Small
Dynamic Strength	Good	Medium
Cycle time	Short	Short
Price	High	Low

computational difficulties. For use in large structures, a reliable simplified numerical model is needed. Today, commercial software tools already offer various integrated numerical models that can be used for simulation of mechanical joints. Such an approach was used by e.g., Porcaro et al. [10], Yang et al. [20] or Kulawik and Wrobel [21]. Porcaro et al. [10] used a pre-set spot-weld model in LS-Dyna software, which joined the sheet metal with a simple line element that connected it on the sheet through contact conditions that ensured a transfer of forces and torques between the two sheets. The material parameters, which influenced the result of numerical analyses, were adjusted and modified iteratively by the researchers based on matching the results of simulations to the results of physical tests. In a similar way, Sommer and Maier [22] and Hanssen et al. [23], who were dealing with this issue using a more complex approach, used a calibration method in combination with physical tests to define the necessary joint parameters. Sommer and Maier [22] compared both several different geometric models of connecting elements and several different material models. They built various combinations of both geometric and material models and compared the results of numerical analyses with physical testing at chosen load cases. The material parameters were estimated on the basis of the calibration process that was based on the numerical force-displacement curve fitting to the curve obtained from the test. The results were promising and proved a good match with the experimental observations. Similarly, Hanssen et al. [23] focused on a numerical model and developed an algorithm to identify parameters of a numerical model, again based on physical testing. According to this methodology, the user defines the point between the sheets where the riveted joint is located and defines the cross-section of that joint. The algorithm searches for all the relevant nodes in the cross-section area of the rivet and connects the sheet metal. Through these nodes the loads are transferred and the joint response is calculated by the algorithm. However, for the operation of the model and the algorithm, it is necessary to define a wide range of parameters, which must be estimated through physical testing in various load cases. Nevertheless, the results obtained from such a model match well with the actual state.

In this study, the mechanical joint has also been modelled in a simplified way, whilst the number of the necessary material parameters has been minimised to the lowest possible amount which still ensured comparable results of the simulations and experimental observations. This way a high computational efficiency for analyses of large structures can be preserved. Mechanical joints have been modelled with a line element that is connected to the two sheet metals. A bilinear material model has been assigned to both the sheet metal and the joint, as the results of physical tests show an extreme bilinearity until the point of failure. Nevertheless, the material parameters of the sheet metal and the joint have been separately considered in the simulations. Namely, the physical features of the joint have been incorporated into its bilinear behaviour. Thus, both the set and the range of the material parameters for the joint have first been defined. Next, using an optimization method based on the full factorial test and application of the response surface method in combination with a real-valued genetic algorithm, an optimal combination of the values of the material parameters has been determined. Finally, the numerical model of the mechanical joint for a 2 mm thick sheet metal of S500MC material has been validated.

1 METHODOLOGY

1.1 Experimental Set-up

Two types of joints of a 2 mm thick sheet metal made of S500MC material were tested, a self-piercing rivet joint and a clinch joint. Self-piercing rivets with diameter of 5 mm were manufactured and mechanical clinching tool with 8 mm diameter was used for clinch joints. Static tests have been performed on the joints during experimental validation.

Furthermore, two specimen types have been manufactured, the shapes of which were in compliance with the standard DVS/EFB 3480-1 [24], see Fig. 1. The width of the specimens was 45 mm.

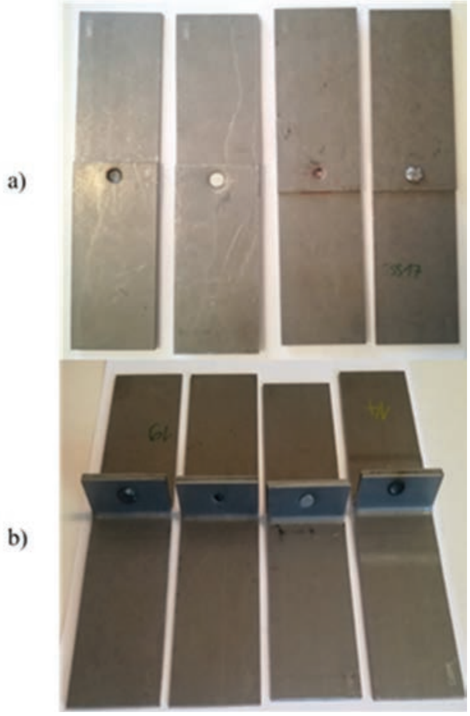

Fig. 1. *The specimens for physical tests: a) overlapping joint and b) flanged joint for peel tests*

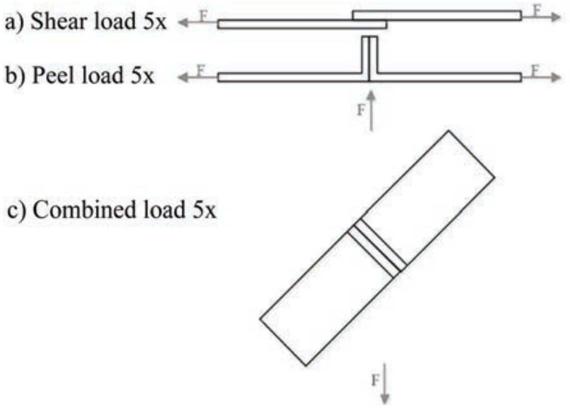

Fig. 2. *Loading conditions: a) for shear strength test; b) for the peel test; c) for the combined test; clamps of the test rig and the compensation tabs are pointed out during application of the combined load*

Specimen types corresponded to two load cases, which are also prescribed by the standard DVS/EFB 3480-1 [24], and an additional combination of these two load cases, see Fig. 2:

- Static shear strength test for an overlapping joint.
- Static peel strength test for a flanged joint.
- Static combined tensile-shear test for a flanged joint, with a load at an angle of 45°. Additionally, compensation tabs to accommodate the misalignments of the specimens were adopted during the of tensile-shear test.

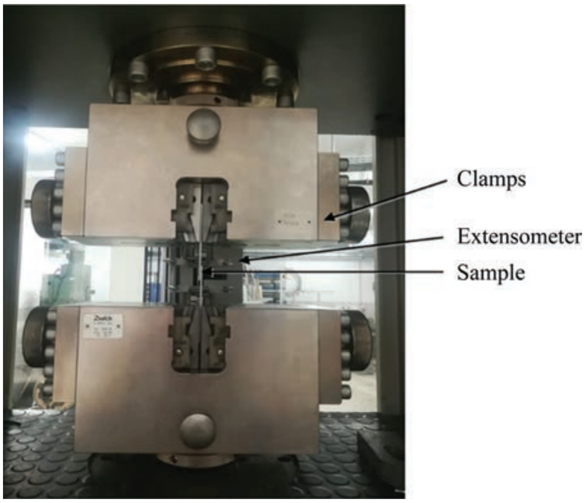

Fig. 3. *Layout of the test rig*

Each loading condition was repeated five times, for both types of joints. In total, 15 specimens for each type of the joint were tested. The tests were carried out on a certified Zwick/Roell Z150 test rig, see Fig. 3. The specimens were inserted in the clamps in the length of 40 mm. The load was applied by means of the clamp displacement at a rate of 10 mm/s with monitoring the force on the clamp at a given displacement. The results of each five repetitions were averaged, and the resulting force-displacement curve served as the basis for comparison with numerical simulations.

1.2 Numerical Model

Simulia Abaqus software was used to build the simplified finite-element model. The sheet metals were modelled with shell elements. The joint was modelled as a line connecting sheets by a kinematic or distributing connection as shown in Fig. 4. The size and the quality of the finite element mesh was generated according to the industrial requirements for crash simulations. Specifically, Timoshenko beams designated as B32 type in Abaqus were used to represent either the self-piercing rivet or the clinch joint. One beam connected the centres of the holes and several beams connected each centre of the hole with the circumferential nodes (Fig. 4).

A structured and denser mesh was created around the joint. Rectangular S4 type shell elements and triangular S3R type shell elements were applied. The size of the bore was equal to the diameter of the connecting element representing the joint. A general contact was assigned between the sheets taking into account the friction between the sheets by a coefficient μ = 0.6 [25]. The boundary conditions represented the clamping of the sheets into the test rig. This involved fixed nodes on one sheet metal and application of prescribed displacement to the nodes on the other sheet metal to mimic the experimental setup as depicted in Fig. 2. The prescribed displacement was applied in a series of steps. The size of each step was limited upwards with 10 % of the final value of the displacement.

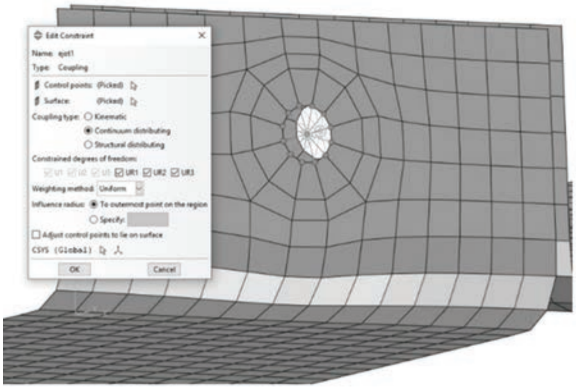

Name: ejot1
Type: Coupling
Control points: (Picked)
Surface: (Picked)
Coupling type: ○ Kinematic ● Continuum distributing ○ Structural distributing
Constrained degrees of freedom: ☑ U1 ☑ U2 ☑ U3 ☑ UR1 ☑ UR2 ☑ UR3
Weighting method: Uniform
Influence radius: ● To outermost point on the region ○ Specify:
☐ Adjust control points to lie on surface
CSYS (Global)

Fig. 4. *Model of the mechanical joint*

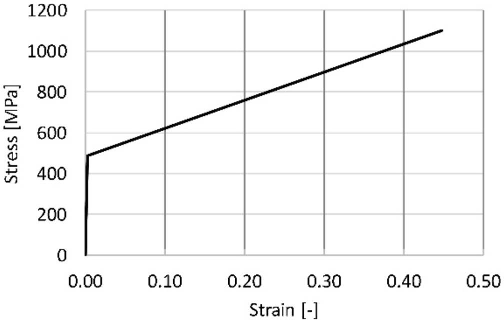

Fig. 5. *Bilinear true stress-strain curve used to model S500 MC sheet metal behaviour*

A bilinear true stress-strain curve for S500 MC is given in Fig. 5. The sheet metal was modelled using these properties. A bilinear material model and round cross-sections were also assigned to the line elements, which were used to model the joint. The diameter of the cross-section was equal to the cross-section of the connecting element. However, the parameters of the bilinear elastoplastic properties of the joint differed from the true material properties for S500 MC and rather represented its physical response under the loading. All the peculiarities of the joint were hence integrated and represented by the bilinear characteristic of the joint. The goal of the simulations was then to determine the optimal values of the parameters of the modelled joint. In doing so, a constant value of Poisson's ratio and a constant material density were assumed. Optimal values of the following parameters were searched for, which fully described the behaviour of the joint:

- elastic modulus, E [MPa],
- tangent modulus, E_T [MPa], and
- yield stress, $R_{p0.2}$ [MPa].

To define the optimal values of these parameters, a full factorial test was performed which used the response surface method in combination with genetic algorithm. In the first step, domain limits were defined within which the parameter values were searched for and these domains were then further divided into multiple values within the search area. In the next step, possible combinations p of the parameter values were defined. For each of the combinations, a numerical analysis of the tensile test was then performed including each of the three load cases. In total, $3p$ simulations for each type of joint were performed. The numerically calculated force-displacement curves for each parameter combination and load case were compared to the experimental results. The agreement between the measured and the modelled response of a joint was then estimated using the sum of the squared distances ($SSQD$) for the force differences at a certain displacement:

$$SSQD^{(j)} = \sum_{i=1}^{K_j} \left(F_{\mathrm{sim}}(x_i) - F_{\mathrm{exp}}(x_i)\right)^2, \qquad (1)$$

where F_{exp} represents the measured force from the tensile test, F_{sim} is the calculated force as a result of numerical simulations, j is the associated load case, K_j is the number of repetitions of a load case, and x represents the displacement. Since the main objective was to determine the material parameters that would optimally fit all three load cases, a multi-criteria objective function was defined as:

$$F_{\mathrm{C}} = \sum_{j=1}^{n_{\mathrm{T}}} w_j \cdot SSQD^{(j)}, \qquad (2)$$

where w_j represents a weight by which the significance or impact of each load case is attributed and n_{T} stands for the number of load cases. For each combination of parameters defined in Table 2, the value of the objective function was calculated as:

$$F_{\mathrm{C}}^{(m,n,o)} = F_{\mathrm{C}}(E^{(m)}, E_{\mathrm{T}}{}^{(n)}, R_{\mathrm{p0.2}}{}^{(o)}); \\ m = 1,\ldots,k;\;\; n = 1,\ldots,l;\;\; o = 1,\ldots,r, \qquad (3)$$

where m, n, and o are the running indices through the levels of the material parameters, which are listed in Table 2. The most suitable values of the material parameters are those that give the lowest value of the objective function F_C. The known values of combinations of parameters, together with the associated value of the objective function, represent the points in a four-dimensional space. These points are distributed relatively evenly throughout the space. Since the optimal combination of parameters lies within this range, it is not necessary for the optimal combination to be one of the combinations that were defined initially; the optimal combination might lie between the chosen points. Therefore, a response surface method was used, which enables an approximation of the surface through the calculated points in the four-dimensional space. This step then makes possible to determine the value of the objective function for any combination of material parameters, even for that combination which was not used during the numerical analysis.

The response surface for the objective function F_C was modelled as the sum of global trend $F_\mathrm{C,glob}$ and local specifics $F_\mathrm{C,loc}$ of the objective function **[10]**, **[15]**, and **[26]**. The local deviations of the objective function from the global trend were modelled using a mixture of multivariate elliptical Gaussian functions whereas the whereas the global trend was modelled using a third-degree polynomial for the three independent variables (E, E_T and $R_\mathrm{p0.2}$) and one dependent variable (objective function F_C):

$$\begin{aligned} F_\mathrm{C,glob}(x_1,x_2,x_3) &= a_0 + \sum_{r=1}^{3}\sum_{q=1}^{3} a_{r,q}x_q^r + a_{2,4}x_1x_2 \\ &+ a_{2,5}x_1x_3 + a_{2,6}x_2x_3 + a_{3,4}x_1^2x_2 \\ &+ a_{3,5}x_1x_2^2 + a_{3,6}x_1^2x_3 + a_{3,7}x_1x_3^2 \\ &+ a_{3,8}x_2^2x_3 + a_{3,9}x_2x_3^2 + a_{3,10}x_1x_2x_3, \end{aligned} \tag{4}$$

where:

$$x = \begin{bmatrix} x_1 \\ x_2 \\ x_3 \end{bmatrix} = \begin{bmatrix} E \\ E_\mathrm{T} \\ R_\mathrm{p0.2} \end{bmatrix}. \tag{5}$$

Parameters a_0 and $a_{r,q}$ are the parameters of the polynomials determined by the polynomial approximation for the p points from Eq. (3). The coefficients of the polynomial were estimated from the experimental data using the pseudo-inverse matrix as follows:

$$\mathbf{a} = (\mathbf{X}^\mathrm{T}\cdot\mathbf{X})^{-1}\cdot\mathbf{X}^\mathrm{T}\cdot\mathbf{y}, \tag{6}$$

where the individual vectors and the matrix are the following:

$$\mathbf{a} = \begin{bmatrix} a_0 \\ a_{1,1} \\ \vdots \\ a_{3,10} \end{bmatrix}, \quad \mathbf{y} = \begin{bmatrix} F_C^{(1,1,1)} \\ F_C^{(1,1,2)} \\ \\ F_C^{(k,l,r)} \end{bmatrix},$$

$$\mathbf{x} = \begin{bmatrix} 1 & E^{(1)} & E_\mathrm{T}^{(1)} & R_\mathrm{p0.2}^{(1)} & \cdots & E^{(1)} & E_\mathrm{T}^{(1)} & R_\mathrm{p0.2}^{(1)} \\ 1 & E^{(1)} & E_\mathrm{T}^{(1)} & R_\mathrm{p0.2}^{(2)} & \cdots & E^{(1)} & E_\mathrm{T}^{(1)} & R_\mathrm{p0.2}^{(2)} \\ \vdots & \vdots & \vdots & \vdots & \ddots & \vdots & \vdots & \vdots \\ 1 & E^{(k)} & E_\mathrm{T}^{(l)} & R_\mathrm{p0.2}^{(r)} & \cdots & E^{(k)} & E_\mathrm{T}^{(l)} & R_\mathrm{p0.2}^{(r)} \end{bmatrix}. \tag{7}$$

The displacement points, in which the forces were compared, were selected based on the physical test results. As different load cases withstood different breakage forces at different final displacements, there was no possibility to choose exactly the same displacement points for all load cases. Based on the displacement-force diagram from the physical tests, the breakage point was established for each load case. This displacement was then used in numerical simulation as a maximum displacement by which the samples were loaded. The whole displacement range was divided equidistantly into 10 points, the final point being the breakage point from physical test. Those points were the displacement points in which the measured and the calculated forces were compared and used in Eq. (1).

Having determined the parameters of the polynomials that describe the global trend of the response surface, the residual R_C between the actual value of the objective function F_C and the value of its global trend of the $F_\mathrm{C,glob}$ could be determined for each point from Eq. (3) as:

$$R_\mathrm{C}^{(m,n,o)} = F_\mathrm{C}^{(m,n,o)} - F_\mathrm{C,glob}^{(m,n,o)},$$
$$m = 1,\ldots,k, \quad n = 1,\ldots,l, \quad o = 1,\ldots,q. \tag{8}$$

Then, the R_C values were integrated into a conditional-average estimator using local multidimensional Gaussian functions to obtain a model of local specifics of the objective function $F_\mathrm{C,loc}$ **[10]**, **[15]**, and **[25]**:

$$F_\mathrm{C,loc} = \frac{\sum_{m=1}^{k}\sum_{n=1}^{l}\sum_{o=1}^{q} R_\mathrm{C}^{(m,n,o)}\cdot W\left(X - X^{(m,n,o)};\Sigma^{(m,n,o)}\right)}{\sum_{m=1}^{k}\sum_{n=1}^{l}\sum_{o=1}^{q} W\left(X - X^{(m,n,o)};\Sigma^{(m,n,o)}\right)}, \tag{9}$$

where $R_\mathrm{C}^{(m,n,o)}$ stands for residuals from Eq. (8), $\mathbf{x}$ are vectors from Eq. (5), W represent multidimensional Gaussian functions with median values vector in points $\mathbf{x}^{(m,n,o)}$ and $\mathbf{\Sigma}^{(m,n,o)}$ are covariant matrices of individual Gaussian functions. The individual multidimensional Gaussian functions W were hence defined as:

$$W\left(\mathbf{x}-\mathbf{x}^{(m,n,o)};\Sigma^{(m,n,o)}\right)=\frac{\sqrt{\det\left[\left(\Sigma^{(m,n,o)}\right)^{-1}\right]}}{\left(2\cdot\pi\right)^{d/2}}$$

$$\cdot\exp\left[-\frac{1}{2}\cdot\left(\mathbf{x}-\mathbf{x}^{(m,n,o)}\right)^{\mathrm{T}}\cdot\left(\Sigma^{(m,n,o)}\right)^{-1}\cdot\left(\mathbf{x}-\mathbf{x}^{(m,n,o)}\right)\right],(10)$$

where d is the dimension of the vector of independent variables, in this case the number of load cases ($d = 3$). Covariance matrices are diagonal with their variances equal to the distances to the nearest adjacent point in the direction of the individual components of vector **x**. In order to facilitate the data processing, individual variables (independent and dependent) were converted to logarithmic values before the process of global-local modelling of the objective function.

In the last step, the objective function surface was calculated and the response surface was defined:

$$\widehat{F}_{\mathrm{C}}(X)=F_{\mathrm{C,glob}}(X)+F_{\mathrm{C,loc}}(X). \qquad (11)$$

This way it was possible to model a multi-dimensional surface that arbitrarily approaches any actual value of the measured point or, in this case, the result of the numerical analysis for each combination of parameters, while maintaining the trend without local deviations even outside of the measurement range [18]. The response surface thus assists in finding the domain of the optimal parameter values, but it is still difficult to accurately determine the actual optimum. Here, a real-valued genetic algorithm was hence utilised, which enabled the determination of the optimal combination of material parameters of the joint, minimizing Eq. (11). The in-house genetic algorithm used in this study combined the classic single-point crossover and linear crossover. The mutation-with-momentum of the child chromosomes enabled a better fine-tuning of the later generations of chromosomes to the optimal solution [26] to [28]. A population size of m = 20 randomly selected starting points on the response surface was used with the probability of crossover p_{cr} = 0.5, fraction of linear crossover f_{lin} = 0.6 and probability of mutation p_{mut} = 0.05. The algorithm was stopped after 10000 generations which is usually sufficient for a satisfactory optimum [26]. The above-described procedure for determining the optimum values of the parameters E, E_T and $R_{p0.2}$ was repeated for both joint types.

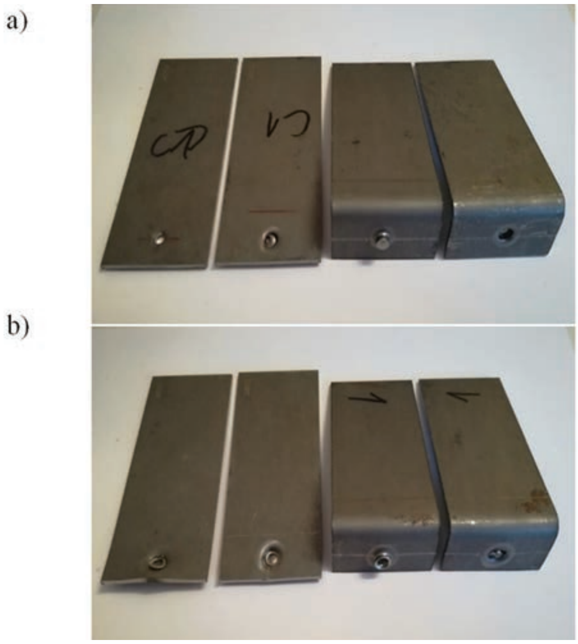

Fig. 6. *Broken-down specimens of: a) SPR joint, and b) clinch joint*

2 RESULTS

During the test, the force-displacement dependence was monitored and recorded until failure. In Fig. 6, the broken specimens are shown. The results of the measurements were filtered and represented in diagrams for all test repetitions of each load case, and then, based on the curves obtained, the average force-displacement curve was defined. This curve later served as the comparative indicator in the objective function. The average curve was generated to the point where the joint started to loosen and the value of the force began to decline, which is also seen in Figs. 7 and 8. The measurements showed good repeatability for both joint types and all three load cases. Only one of the results of the clinch joint measurements for the shear load case was later excluded as that specific measurement deviated incomparably from the other measurements. The final displacement of the average curve was also the displacement value up to which the numerical model of the joint was loaded.

Using the developed methodology, an optimal combination of the material parameters of the joint was generated, which on average can simulate the force-displacement responses best for all the three load cases, so they are hence suitable to use in a general model for any other load case. Additionally, the methodology was used to determine the material parameters considering only a single load case. This served for verification purposes and confirmation of

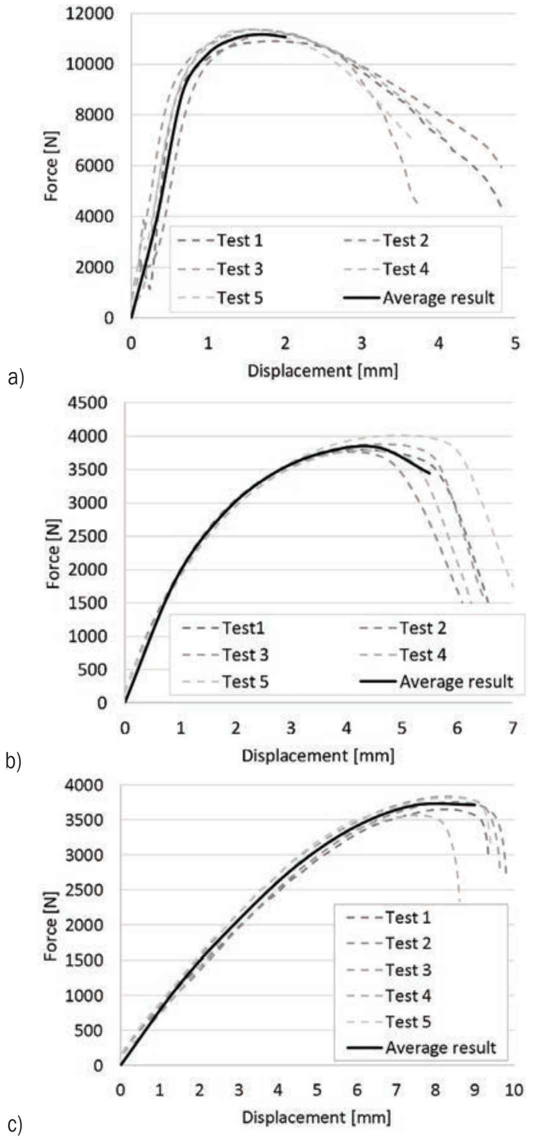

Fig. 7. *Measurement results for SPR joint: a) shear load case, b) peel load case, and c) combined load case*

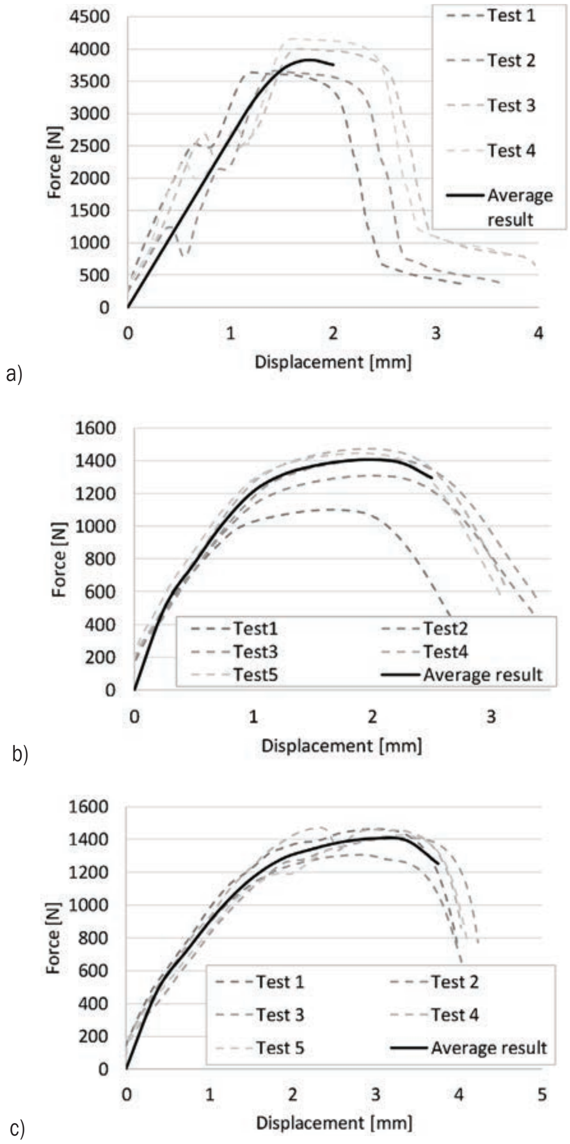

Fig. 8. *Measurement results for clinch joint: a) shear load case, b) peel load case and c) combined load case*

the best-fit ability of the method itself. During the parameter-estimation process, a starting point in the set of parameters was defined and a range of values within the algorithm performed its operation.

The range of values of the material parameters was divided approximately equidistantly in the logarithmic scale within the defined range. Table 2 shows the values and the range of parameters. In total, p = 175 combinations of material parameters from Table 2 are possible for a single load case, which results in a total of $3p$ = 525 numerical analyses.

Table 2. *Values of parameters E [MPa], E_T [MPa] and $R_{p0.2}$ [MPa]*

Parameter	Search domain	The values of the parameters taken into account						
Elastic modulus - E	200-300000	200	500	1000	3000	10000	30000	300000
Tangent modulus - E_T	0.1·E- 0.001·E	0.1·E	0.0286·E		0.01·E	0.00286·E		0.001·E
Flow limit - $R_{p0.2}$	50-1000	50	100		200	500		1000

3 DISCUSSION

The force-displacement results of the measurements indicated that the response of each joint had a pronounced bilinear characteristic. Accordingly, the stress-strain behaviour of the connecting element in the joint was hence modelled using a bilinear material model. The failure of both the SPR and the clinch joint occurred in the very connection or in the connective element (Fig. 6). In the case of the SPR joint, the rivet was pulled out, and in the case of the clinch joint, the mechanical connection between the two sheets was broken. From this point of view, attention could be paid only to the connective element and its modelling, whilst the base material was modelled with a simple elastic-plastic material model.

It can be noted that in the case when each load case is treated separately (Figs. 9 and 10 – specific result), it is possible to accurately predict the combination of parameters that produce a numerical response of the joint almost identical to the measured response. By changing the range of the input parameters or even the type of the material model, a better agreement might also be possible to achieve. However, the method is primarily intended to determine the material parameters of the joints for general use in large structures with a large number of such joints whilst they are subjected to a random load. This response should therefore be the best approximation of the observed response of the joint regardless of the size and the direction of the applied load.

The method thus enables consideration of the agreement between the numerical and experimental response of the joint for several load cases. Consequently, the resulting values of the material parameters are always a compromise for several load cases and the deviation between the numerical response and the experimental response. A better agreement is hence always observed when only a single load case is considered during the estimation of the optimal material parameters.

Furthermore, other types of joints will have other properties therefore it is necessary to perform some initial tests under shear, peel and combined tensile-shear load conditions to be able to search for the optimal values of the parameters in the numerical model. After these have been performed however, the numerical model of a complex structure with such a joint can be used under arbitrary load conditions.

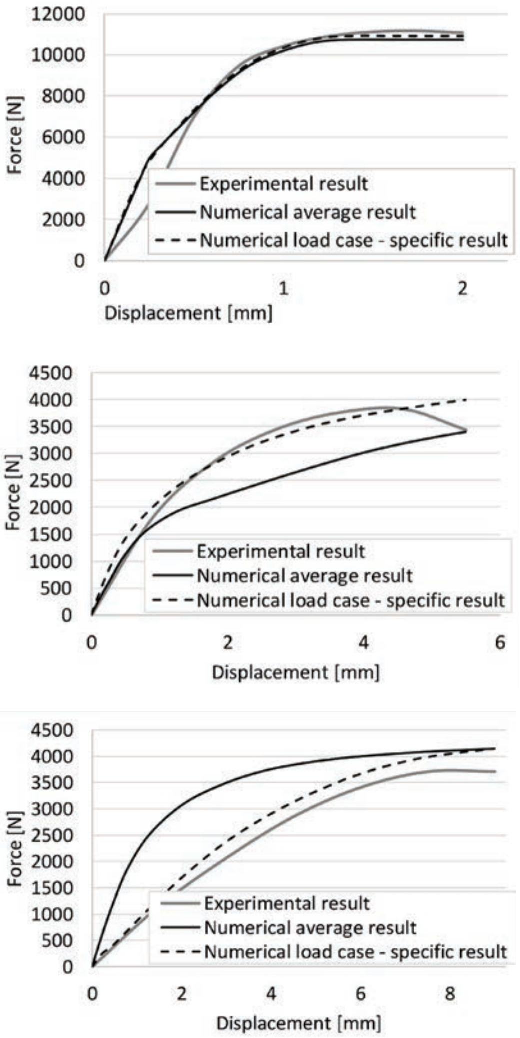

a)
b)
c)

Fig. 9. *Comparison of numerical and actual response of SPR joint: a) shear load case, b) peel load case, c) combined load case*

For the correct performance of the method, it is essential to correctly define the material model, the range of possible values of associated material parameters and to perform accurate measurements which serve as a comparative value for numerical simulations. Choosing a more complex material model might lead to a more accurate understanding of the joint behaviour, while on the other hand, results in a more complex definition of the objective function and extends the numerical calculation time, which is of crucial importance in practice. Likewise, it is not possible to accurately determine the values of the material parameters if the search area is too wide or too narrow. If the search domain differs from the final area presented in Table 2, it may happen that the positions of the optimal parameter values lie outside of the defined search range. An example of such an inadequately defined search range is presented for the SPR joint in Fig. 11. The comparison of the results between the inadequately and adequately defined

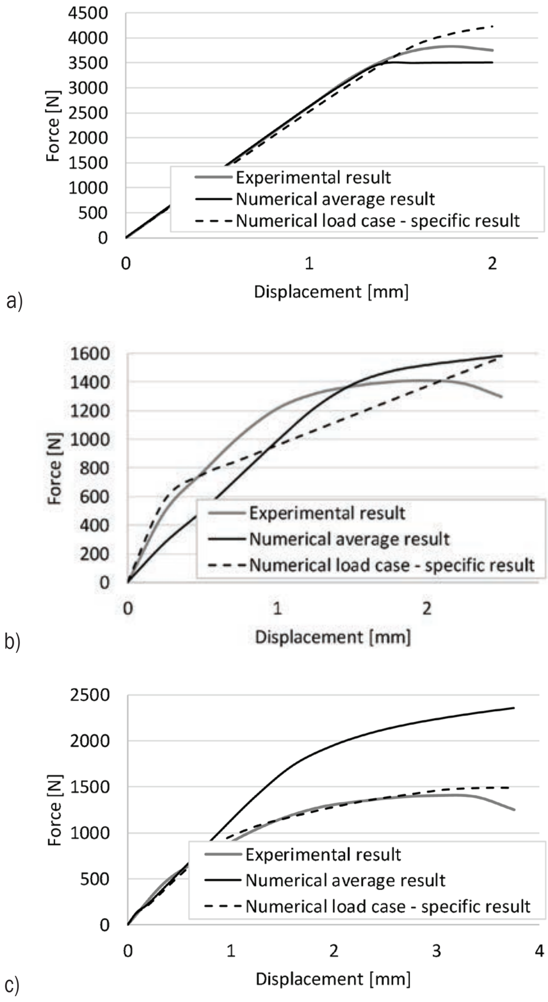

Fig. 10. *Comparison of numerical and actual clinch joint response: a) shear load case, b) peel load case, c) combined load case*

search ranges reveals that the force-displacement description can drastically differ if the initial search domain of the parameters is too wide.

The material model of the joint used in this study succeeds in describing the force-displacement response as long as the force increases with increasing displacement and shows a pronounced bilinearity. When the maximum force is achieved in practice, the joint begins to loosen, the force begins to decline, and the joint then gradually breaks down. In numerical analyses however, such behaviour of the joint cannot be modelled using a bilinear material model. Hence, only the "functional" part of the joint behaviour can be simulated, i.e., the increasing part of the force-displacement characteristics until the maximum force. For the correct performance of the developed methodology this fact has to be taken into account in numerical simulations so that the final simulated displacement coincides with the experimental displacement at the maximum value of the force. If the displacements exceeding this limit are considered during the optimization of the material parameters, the error of the method will increase as a consequence of the diverging experimental and simulated curves.

The final values of the material parameters can also be influenced by weights assigned to the load cases in the objective function. The importance of a specific load case can hence be considered. This is most easily explained if the values of forces that occur in individual load case are observed. The force in the case of the shear test is approximately twice as high as in the other load cases. Consequently, at higher force values, the relative difference of the numerical and the experimental result will be comparable to other load cases, whilst the absolute value of the difference will be significantly higher than for the other load cases.

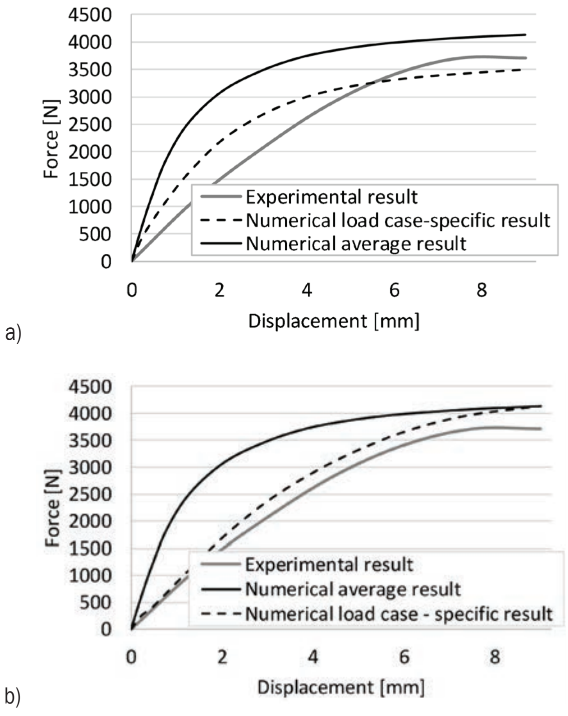

Fig. 11. *Force-displacement results for: a) inadequately defined search range, and b) adequately defined search range*

Hence, the value of the objective function strongly depends on the tensile case and less on the other two cases. Thus, by using weights, individual contributions of various load cases to the objective function can be balanced and their importance for the final result can be evenly distributed. Nevertheless, the above-mentioned differences did not provide a significant impact on the final result during this study, therefore equal weights were attributed to the various load cases. The optimal values of the parameters to simulate the response of the self-piercing rivet joint were determined as E = 8980 MPa, E_T = 260 MPa and $R_{p0.2}$ = 217 MPa. Similarly, the optimal values of the parameters for the clinch joint were determined as E = 1042 MPa, E_T = 1.5 MPa and $R_{p0.2}$ = 195 MPa. Nevertheless, these values of the parameters represent synthetic properties of the joint and not the material properties of the assembly.

4 CONCLUSIONS

The force-displacement response of both the self-piercing rivet joint and the clinch joint tested during this study exhibited distinctly bilinear characteristics up to the highest measured force before failure. The presented methodology could be applied to determine optimal values of material parameters for the bilinear material model. Numerical analyses of large structures with a number of such joints, each having the same values of the material parameters, can thus be performed to simulate their stress-strain or force-displacement behaviour under variable loading. The optimal values of the material parameters represent a compromise between the quality of fit and the variety of load cases.

5 ACKNOWLEDGEMENTS

The authors acknowledge financial support from the Slovenian Research Agency (research core funding No. P2-0182 entitled Development evaluation).

6 REFERENCES

[1] Barimani-Varandi, A., Aghchai, A.J., Lambiase, F. (2021). Failure behavior in electrically-assisted mechanical clinching joints. *Journal of Manufacturing Processes*, vol. 68 p. 1683-1693, **DOI:10.1016/j.jmapro.2021.06.072**.

[2] Mori, K., Abe, Y. (2018). A review on mechanical joining of aluminium and high strength steel sheets by plastic deformation. *International Journal of Lightweight Materials and Manufacture*, vol. 1, no. 1, p. 1-11, **DOI:10.1016/j.ijlmm.2018.02.002**.

[3] Yang, Y., Xiong, X., Chen, J., Peng, X., Chen, D., Pan, F. (2021). Research advances in magnesium and magnesium alloys worldwide in 2020. *Journal of Magnesium and Alloys*, vol. 9, no. 3, p. 705-747, **DOI:10.1016/j.jma.2021.04.001**.

[4] Abe, Y., Kato, T., Mori, K. (2007). Joining of aluminium alloy and mild steel sheets using mechanical clinching. *Material Science Forum*, vol. 561 1043-1046, **DOI:10.4028/www.scientific.net/MSF.561-565.1043**.

[5] He, X., Zhao, L., Yang, H., Xing, B., Wang, Y., Deng, C., Gu, F., Ball, A. (2014). Investigations of strength and energy absorption of clinched joint. *Computational Materials Science*, vol. 94, p. 58-65, **DOI:10.1016/j.commatsci.2014.01.056**.

[6] Maiwald, M., Thiem, J. (2012). Joining without a pilot hole using friction welding. *ATZ Production Worldwide*, vol. 5 10-17, **DOI:10.1365/s38312-012-0045-0**.

[7] Tozaki, Y., Uematsu, Y., Tokaji, K. (2010). A newly developed tool without probe for friction stir spot welding and its performance. *Journal of Materials Processing Technology*, vol. 210, no. 6-7, p. 844-851, **DOI:10.1016/j.jmatprotec.2010.01.015**.

[8] Özdemir, U., Sayer, S., Yeni, Ç. (2012). Effect of pin penetration depth on the mechanical properties of friction stir spot welded aluminium and copper. *Material Testing*, vol. 54, no. 4, p. 233-239, **DOI:10.3139/120.110322**.

[9] Perrett, J.G., Martin, J., Threadgill, P.L., Ahmed, M.M. (2007). Recent Developments in Friction Stir Welding of Thick Section Aluminium Alloys. *6th World Congress, The aluminium Two Thousand*. p. 1-11.

[10] Porcaro, R., Hanssen, A.G., Aalberg, A., Langseth, M. (2004). Joining of aluminium using self-piercing riveting: Testing, modeling and analysis. *International Journal of Crashworthiness*, vol. 9, no. 2, p. 141-154, **DOI:10.1533/ijcr.2004.0279**.

[11] Abe, Y., Kato, T., Mori, K. (2006). Joinability of aluminium alloy and mild steel sheets by self piercing rivet. *Journal of Materials Processing Technology*, vol. 177, no. 1-3, p. 417-421, **DOI:10.1016/j.jmatprotec.2006.04.029**.

[12] Li, D., Chrysanthou, A., Patel, I., Williams, G. (2017). Self-piercing riveting-a review. *The International Journal of Advanced Manufacturing Technology*, vol. 92, p. 1777-1824, **DOI:10.1007/s00170-017-0156-x**.

[13] Di Franco, G., Fratini, L., Pasta, A., Ruisi, V.F. (2013). On the self piercing riveting of aluminium blanks and carbon fibre composite panels. *International Journal of Materials Forming*, vol. 6, p. 137-144, **DOI:10.1007/s12289-011-1067-2**.

[14] Su, Z.-M., Lin, P.-C., Ali, W.-J., Pan, J. (2015). Fatigue analyses of self-piercing rivets and clinch joints in lap-shear specimens of aluminum sheets. *International Journal of Fatigue*, vol. 72, p. 53-65, **DOI:10.1016/j.ijfatigue.2014.09.022**.

[15] Abe, J., Mori, K., Kato,T. (2012). Joining of high strength steel and aluminium alloy sheets by mechanical clinching with dies for control of metal flow. *Journal of Materials Processing Technology*, vol. 212, no. 4, p. 884-889, **DOI:10.1016/j.jmatprotec.2011.11.015**.

[16] Martinsen, K., Hu, S.J., Carlson, B.E. (2015). Joining of dissimilar materials. *CIRP Annals*, vol. 64, no. 2, p. 679-699, **DOI:10.1016/j.cirp.2015.05.006**.

[17] Kaščak, L., Spišak, E. (2013). Mechanical joining methods in car body construction. *Transfer inovacii*, vol. 28, p. 168-171.

[18] Škrlec, A., Klemenc, J. (2017). Parameter identification for a Cowper-Symonds material model using a genetic algorithm combined with a response surface. *Engineering Computations*, vol. 34, no. 3, p. 921-940, **DOI:10.1108/EC-03-2016-0099**.

[19] Bouchard, P.O., Laurent, T., Tollier,L. (2008). Numerical modeling of self-pierce riveting-From riveting process modeling down to structural analysis. *Journal of Materials Processing Technology*, vol. 202, no. 1-3, p. 290-300, **DOI:10.1016/j.jmatprotec.2007.08.077**.

[20] Yang, L., Yang, B., Yang, G. W., Xiao, S. N., Zhu, T., Wang, F. (2020). S-N Curve and Quantitative Relationship of Single-Spot and Multi-Spot Weldings. *International Journal of Simulation Modelling*, vol. 3, p. 482-493, **DOI:10.2507/IJSIMM19-3-CO11**.

[21] Kulawik, A., Wrobel, J. (2020). Numerical Study of Stress Analysis for the Different Widths of Padding Welds. *Strojniški vestnik - Journal of Mechanical Engineering*, vol. 66, p. 567-580, **DOI:10.5545/sv-jme.2020.6771**.

[22] Sommer, S., Maier, J. (2011). Failure modeling of a self-piercing riveted joint using LS-DYNA. *8th European LS-DYNA Conference*, Strasbourg.

[23] Hanssen, A.G., Oolsson, L., Porcaro, R., Langseth, M. (2010). A large-scale finite element point-connector model for self-piercing rivet connections. *European Journal of Mechanics-A/Solids*, vol. 29, no. 4, p. 484-495, **DOI:10.1016/j.euromechsol.2010.02.010**.

[24] DVS/EFB 3480-1:2010 (2010). Testing of Properties of Joints - Testing of Properties of Mechanical and Hybrid Joints. *DVS Media*, Düsseldorf.

[25] Wittel, H., Muhs, D., Jannasch, D., Voßiek, J. (2013). *Roloff/Matek Maschinenelemente*, Springer Fachmedien, Wiesbaden, **DOI:10.1007/978-3-658-02327-0**.

[26] Škrlec, A., Klemenc, J. (2020). Estimating the strain-rate-dependent parameters of the Johnson-Cook material model using optimisation algorithms combined with a response surface. *Mathematics*, vol. 8, no. 7, p. 1-18, **DOI:10.3390/math8071105**.

[27] Wright, A.H. (1991). Genetic Algorithms for Real Parameter Optimization. *Foundations of Genetic Algorithms*, Rawlins, G.J.E. (ed.), vol. 1, Morgan Kaufman, San Mateo, **DOI:10.1016/B978-0-08-050684-5.50016-1**.

[28] Temby, L., Vamplew, P., Berry,A. (2005). Accelerating real-valued genetic algorithms using mutation-with-momentum. *The 18th Australian Joint Conference on Artificial Intelligence*, Sydney, p. 1108-1111, **DOI:10.1007/11589990_149**.

Strojniški vestnik - Journal of Mechanical Engineering 68(2022)1, 14-26
© 2022 The Authors. CC BY-NC 4.0 Int. Licensee: SV-JME
DOI:10.5545/sv-jme.2021.7361
Original Scientific Paper
Received for review: 2021-08-08
Received revised form: 2021-10-11
Accepted for publication: 2021-11-29

Research on the Traction and Obstacle-Surmounting Performance of an Adaptive Pipeline-Plugging Robot

Hongwei Yan[1,*] – Jian Li[1] – Ziming Kou[2] – Yi Liu[1] – Pengcheng Li[1] – Lu Wang[1]
[1]North University of China, School of Mechanical Engineering, China
[2]Taiyuan University of Technology, College of Mechanical and Transport Engineering, China

To solve a series of problems, such as damage, increased impurities and obstacles caused by medium corrosion, and erosion in the long-term use of the pipeline, a multi-body distributed adaptive pipeline plugging and repairing robot with good driving performance and strong reliability is proposed by using the modular design method. By establishing the obstacle-crossing model of the robot, the traction equation and obstacle-crossing equation of the driving wheel and supporting wheel are studied. It can be seen from the equation that reducing the deflection angle of the driving wheel or reducing the speed of the motor spindle can improve the obstacle-crossing ability. The driving unit model is established in ADAMS software, and its running speed, driving force, and obstacle-crossing height are simulated and analysed. The model prototype is established and verified with experiments. When the deflection angle of the robot driving wheel is set to 20° to 35°, it meets the design requirements. When the deflection angle of the driving wheel is set to 20°, the robot has large traction, good running stability and high obstacle-crossing height. The maximum obstacle-crossing height is 6 mm. At this time, the robot reaches the best running state. The design of an adaptive leakage plugging robot for buried pipelines provides an important reference for the research and development of pipeline emergency prevention and control equipment.

Keywords: pipeline leakage, plugging robot, obstacle crossing, optimum driving angle, simulation analysis

Highlights

- *A pipeline leakage self-adaptive sealing robot was designed to realize pipeline leakage detection, rapid plugging and repair, and stable and reliable operation.*
- *This robot has a certain degree of self-adaptive ability, sufficient driving force, better blocking ability, and good obstacle-crossing ability.*
- *The optimum deflection angle of the driving wheel is obtained by analysis. The influence of the change of deflection angle on the obstacle-crossing performance of the robot. Under the optimal deflection angle, the pipeline robot runs smoothly and has a good ability to pass over obstacles.*

0 INTRODUCTION

As the fifth-largest transportation method, pipeline transportation has the advantages of low cost, safety, and reliability and is widely used [1] to [3]. With the large-scale use of pipelines and the increase in their service time, they can be affected by internal corrosion and human intervention, and thus pipelines will always be prone to rupture and erosion [4] to [6]. Buried pipelines will transport oil and natural gas to avoid the interference of external factors and save space [7] to [9]. When there is a leak in a buried pipeline, it is usually excavated directly to find the leakage point and then treated by sectional plugging and repair [10] and [11]. Both pipe wells and buried pipelines encounter difficulties locating leaks and a working environment that is too small, which is not conducive to manual operation [12] to [14]. Therefore, this paper proposes a multi-body distributed pipeline leak self-adaptive plugging robot composed of a pipeline robot and a leak-plugging unit. The driving unit provides a dynamic for the adaptive pipeline-plugging robot to detect the location of pipeline leaks. The leak-plugging unit seals and repairs the pipeline leaks. Numerous in-depth studies have examined this problem. In terms of pipeline robots, the Brazilian CLIDADE team designed an oil and gas pressure-driven robot based on the principle of medium pressure difference. It has built-in ultrasonic flaw detection equipment to detect pipeline leaks and leak point sizes [15]. At Shandong University, Han Meng designed a four-wheeled robot that adopts a modular tandem design and is connected by two robots with universal coupling [16] and [17]. Liu of Southwest Petroleum University in China designed a spiral-driven pipeline robot. He reduced the torque of the spindle motor through the bevel gear and acted on the robot driving wheel. Theoretically, he deduced the relationship between the helical inclination of the driving wheel, the load and the moving speed [18] to [20]. The Canadian company Inuktun developed a crawler robot that can smoothly pass through complex pipelines and is suitable for pipelines with more damage or severe corrosion [21] and [22]. Woongsun Jeon et al. in the United States developed a four-link peristaltic robot, in which the front and rear bodies

---

*Corr. Author's Address: School of Mechanical Engineering, North University of China, Taiyuan, China, aweigeyan@nuc.edu.cn

can be locked or moved relative to the soft axis, and the relative movement between the two bodies can achieve the purpose of moving in the pipe [23] to [25]. Zagler et al. at the Technical University of Munich, Germany, developed the eight-legged robot MORITZ, which is equipped with precision instruments such as angle sensors, microgravity sensors and five-axis acceleration sensors. Although it has good adaptability, its structure is complex, and control is difficult [26] and [27]. A spiral robot makes use of a driving wheel to create spiral motions on the inner wall of the pipeline and transform the circumferential rotation force into axial forward power. It has the characteristics of a high driving force, stable operation, and a simple control mode and is suitable for running in complex pipelines, which has become the focus of this paper. In terms of leakage and plugging, the Oil-States Hydro Tech company was the first to use a device for plugging pipeline leakage points by external pressure, which used the fixture to compress the pipeline leakage point to achieve the purpose of plugging and repairing, mainly for small single-point leakage [28] and [29]. The in-pipe intelligent plugging mechanism designed by Bowie et al. is an in-pipe repair platform composed of a drive system, a plugging system and a carrying system [30]. The United States Furman-Ite company was the first to develop a perforated plugger that integrates perforation, plugging, and transmission, which is widely used in deep-sea high-pressure pipeline leakage [31]. Many scholars have studied different pipeline leakage situations and proposed different plugging and repair methods to achieve the effect of rapid plugging and repair, but at present, few combine pipeline robots with plugging and repair devices. In this context, this paper focuses on the single-point leakage, multipoint leakage, and multipoint long-spacing scattered section leakage of diameter 150 mm buried pipeline, aiming to design a new type of pipeline leakage adaptive plugging robot that integrates in-pipe plugging and quick repair. This article aims to study and analyse the walking stability and obstacle-crossing performance of the robot device, which can lay a theoretical foundation for the in-depth research of a future blockage repair robot.

1 DESIGN OF A PLUGGING ROBOT STRUCTURE

1.1 Overall Structure

The buried pipeline leak self-adaptive plugging robot is primarily intended for pipeline leakage and plugging operations. The buried pipeline environment is complex; the space is small, and over time, various impurities will accrue in the pipe. Therefore, the designed device must have the following characteristics: operability in a complex environment, a certain degree of self-adaptive ability, sufficient traction and driving force, accurate identification of pipeline leakage points and leakage patterns, good operational stability, good plugging ability, and a defined operating speed.

This article intends to design a pipeline emergency plugging and repairing robot that can work smoothly under various complex working conditions to meet the above requirements. According to the previous research results of pipeline robots, the overall structure design needs to meet the design indicators in Table 1. Since the materials transported by buried pipelines are generally flammable and explosive, such as oil and natural gas, and may be corrosive, the mechanical structure of the buried pipeline leakage self-adaptive plugging robot is designed with a protective shell. The buried pipeline leak self-adaptive plugging robot consists of two self-adaptive plugging robots connected by electromagnetic adsorption modules, which can realize docking and separation according to actual working conditions.

Table 1. *Design index of the adaptive plugging robot for buried pipeline leakage*

Serial number	Design indicators	
1	Pipe diameter fitting range	ϕ140 mm to ϕ160 mm
2	The radius of minimum curvature that can pass through the bend	$p \geq 550$ mm
3	Plugging pressure range	0.1 MPa
4	Walking speed in straight pipe	0.01 m/s to 0.04 m/s
5	Walking speed in curved pipe	0.005 m/s to 0.01 m/s
6	Drive unit mass	$m_1 \leq 5$ kg
7	Drive unit length	$L_1 \leq 300$ mm
8	System traction	$F \geq 20$ N
9	Mass of plugging unit	$m_2 \leq 5$ kg
10	Plug unit length	$L_2 \leq 300$ mm

The adaptive plugging robot comprises a drive unit, a leak-plugging unit, and a control unit. The driving unit is the power source of the whole system and provides the driving force for the system; the control components of the whole robot are integrated into the control unit box; and the leakage plugging unit is the working unit of the system, which can plug and repair the leakage point. The parallel coupling connects each unit into a whole, and the structure of the self-adaptive plugging robot for buried pipeline leakage is shown in Fig. 1. The pipeline robot can be

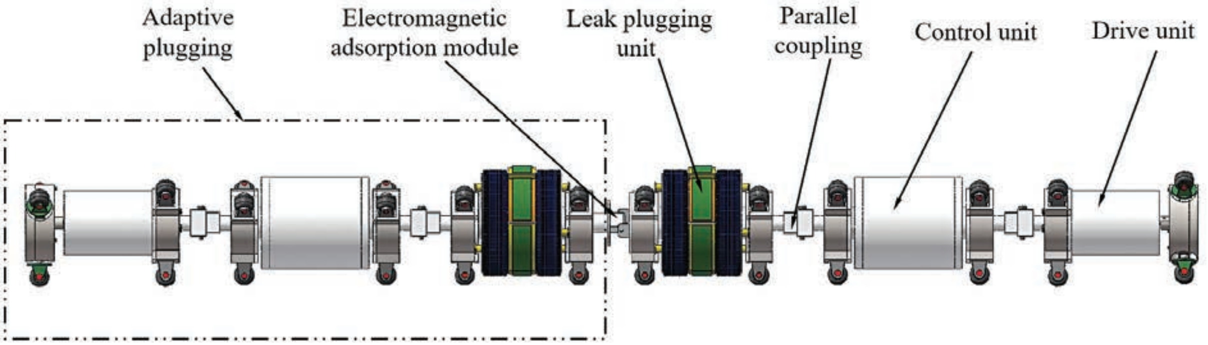

Fig. 1. *Structure diagram of a buried pipeline leak self-adaptive plugging robot*

applied to pipeline leakage detection and intelligent emergency treatment. In case of leakage, the leakage point can be quickly blocked and repaired, and the uninterrupted oil and gas transmission and leakage port cannot be expanded. Only one is selected for analysis because the main structures of the two adaptive plugging robots are exactly the same.

1.2 Drive Unit

The drive unit adopts a closed design, as shown in Fig. 2. It comprises a screwdriver mechanism, a drive motor, and a supporting mechanism. The drive unit adopts a screw-drive as the main transmission mode, and the support mechanism adopts the telescopic spring support. The drive motor provides torque for the screw drive mechanism.

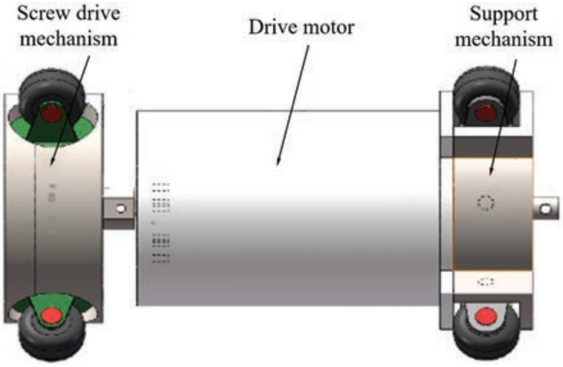

Fig. 2. *Drive unit structure diagram*

The components of the screw drive mechanism include a fixed shell, a driving wheel, a wheel frame, an angle steering gear, a wheel axle, a spring, a fixed frame, and a protective shell, as shown in Fig. 3.

The shell of the screw drive mechanism is composed of a fixed shell and a protective shell. The fixed frame is connected with an adjustable angle steering gear, a wheel frame, and a driving wheel. The fixed housing is connected with the drive motor. The fixed shell is connected with the drive motor. When the drive motor rotates, the motor shaft drives the fixed housing to rotate. At the same time, the fixed shell can rotate the angle-adjusting steering gear, wheel carrier and driving wheel. The driving wheel is installed on the wheel frame, and the wheel frame is fixedly connected with the steering gear axis, so the steering gear can be used to control the wheel frame deflection. The wheel frame limits the position of the angle-adjusting steering gear in the drive unit, and the wheel frame is designed to ensure that the angle-adjusting steering gear can only move up and down. A spring is installed on the bottom of the angle-adjusting steering gear, and the spring is used to connect the steering gear to the wheel frame. The spring plays an adjustment role so that the driving wheel and the steering gear can move up and down with the expansion and contraction of the spring, thereby completing the robot’s self-control adaptation. The drive motor is the power core of the entire system and provides torque for the drive unit.

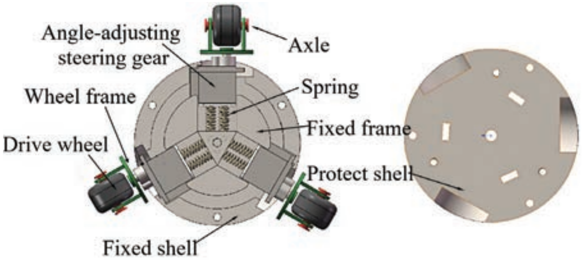

Fig. 3. *Structural diagram of the screw drive mechanism*

The supporting mechanism is composed of nine parts: a supporting wheel, a supporting wheel frame, an inner shell, a supporting wheel shaft, a connecting rod, a spring fixing shell, a spring, an assembly shell, and an outer shell, as shown in Fig. 4. The outer shell structure of the supporting mechanism is composed of an inner shell and an outer shell, which guide the direction of the supporting wheel. The lower end of the connecting rod is connected with a spring, and the upper end is connected with the supporting wheel frame. The spring fixing shell restricts the connecting rod in a circumferential direction so that it can only move up and down. The inner shell is designed with a notch that matches the outer structure of the supporting wheel frame so that the supporting wheel frame can only move up and down. The expansion and contraction of the spring act on the support wheel through the connecting rod so that it can expand and contract within a certain range to enable the functions of support and obstacle crossing. The two parts of the screw drive mechanism and the support mechanism work in coordination so that the entire robot can run adaptively and smoothly in complex pipelines.

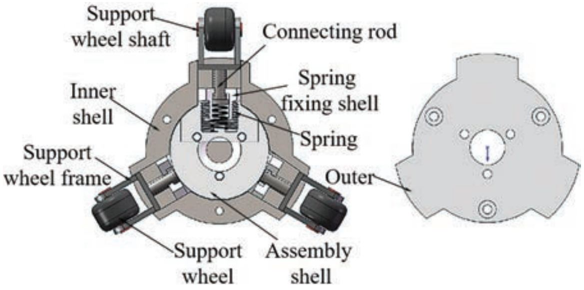

Fig. 4. *Schematic diagram of support mechanism*

1.3 Leak Plugging

The leakage plugging unit primarily comprises seven parts: an electromagnetic adsorption plate, a fixed ring, a plugging airbag, a drainage valve, a support mechanism, an airbag support ring, a plugging layer, and a repairing airbag. The overall structure is shown in Fig. 5.

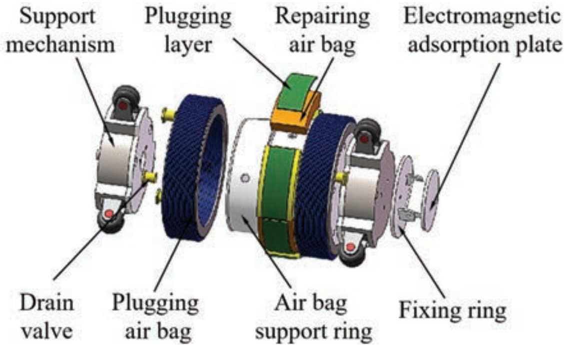

Fig. 5. *Schematic diagram of the leak-plugging unit*

The plugging airbag and the repairing airbag are installed on the airbag support ring, and the airbag support ring has vent holes through which the airbag can be inflated and deflated. When inflating the repairing airbag, the plugging layer connected to the outside of the airbag will be tightly pressed to the leak point of the pipeline for plugging repair work. A drainage valve is installed at both ends of the airbag. When the drainage valve is opened, the medium in the pipeline can pass through the leakage plugging unit through the drainage valve, reducing the resistance to the robot.

2 ANALYSIS OF ROBOT MOTION CHARACTERISTICS

2.1 Robot Traction Analysis

The driving unit provides power for the adaptive pipeline plugging robot. The driving mode of the driving unit is a screw drive. Assuming that the working condition of the robot is ideal, there will be no relative sliding between the driving wheel and the pipe wall, and a force analysis is performed on one of the driving wheels, as shown in Fig. 6.

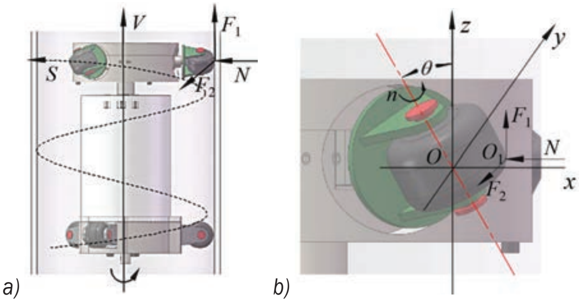

a) b)

Fig. 6. *Traction analysis model diagram;*
a) vertical crawling analysis, and b) driving wheel force analysis

In Fig. 6a, V is the direction of movement of the drive unit, S is the trajectory when the single wheel is in spiral operation, N is the positive pressure between the pipe and the drive wheel, and F_1 is the upward friction of the driving wheel of the driving unit under the action of positive pressure. F_2 is the friction force generated by the driving wheel in the direction of the spiral movement, and f_1 is the dynamic friction coefficient; then, $F_1=f_1 \cdot N$, and θ is the deflection angle of the driving wheel. When the drive unit spirals forward in the pipeline, the traction force can be expressed as Eq. (1):

$$F = 3f_1 \cdot N - 3F_2 \cdot \sin\theta. \tag{1}$$

In Fig. 6b, the force of a single driving wheel in the pipeline is analysed, and according to the static balance equation $\Sigma Fy = 0$, Eq. (2) is obtained:

$$f_2 \cdot \frac{R}{2R} \cdot N + f_3 \cdot \frac{r}{2R} \cdot N - F_2 \cdot R = 0. \tag{2}$$

This is simplified as Eq. (3):

$$F_2 = N \cdot \frac{f_2 \cdot R + f_3 \cdot r}{2R^2}, \tag{3}$$

where f_2 is the rolling friction coefficient of the driving wheel in the pipeline, f_3 is the rolling friction coefficient of the driving wheel on the axle, r is the radius of the axle, and R is the radius of the driving wheel.

Simultaneously solving Eqs. (1) and (3) can solve the driving force F, as shown in Eq. (4):

$$F = 3N\left(f_1 - \frac{f_2 \cdot R + f_3 \cdot r}{2R^2} \sin\theta \right). \tag{4}$$

According to Eq. (4), when the drive unit runs in an ideal non-slippery pipe, the supporting force provided by the pipe to the drive unit is constant. In this case, the magnitude of traction force is only affected by the deflection angle of the drive wheel, and the relationship between the magnitude of traction force and the sine value of the rotation angle of the drive wheel is negatively correlated. In the range of 0° to 90°, when the traction force needs to be increased to complete the climb or pass obstacles in the system, the driving force can be increased by reducing the deflection angle of the drive wheel. To increase the availability of the data, the angle range still needs to be tested by experiment and simulation in the subsequent process.

2.2 Analysis of the Robot's Ability to Surmount Obstacles

A pipeline environment is complex, and obstacles are unavoidable during the robot's operation [32] and [33]. When the adaptive plugging robot passes through obstacles, the changes of speed and force between its driving wheel and the whole robot are complex, and many factors affect its motion. Constructing obstacle-crossing equations from the main influencing factors helps to improve the robot's ability to operate in the pipeline. There are many types of obstacles in a pipeline, and a circular weld is set as the research object here in [34] to [36]. The following is a force analysis of the robot's obstacle-crossing ability under this working condition, as shown in Fig. 7.

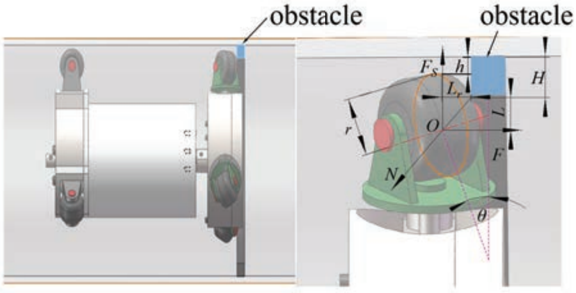

Fig. 7. *Analysis diagram of driving wheel obstacle*

When the robot crosses obstacles, point O is assumed to be the geometric centre of the driving wheel. The convex height of the welding seam is H. Only when the height of the driving wheel lift is h can the driving wheel pass the obstacle smoothly. When the driving wheel touches the welding seam, it will receive a reaction force N given to it by the welding seam. The direction of the reaction force passes through the geometric centre of the wheel. This is the traction force F required by the driving wheel to cross obstacles. The elastic force given by the variable diameter spring on the driving wheel is F_S, the radius of the driving wheel is r, and the deflection angle of the driving wheel when crossing the obstacle is θ.

The spring force acts as resistance when the drive unit crosses the weld. To ensure that the drive unit passes by the welding seam smoothly, the relationship of Eqs. (5) to (10) must be satisfied:

$$M = F \cdot L \geq M_r = F_s \cdot L_r, \tag{5}$$

$$F = \frac{T}{3(R-h)\tan\theta}, \tag{6}$$

$$F_s = F_0 + kh, \tag{7}$$

$$L = r + h - H, \tag{8}$$

$$L_r = \sin\theta \sqrt{r^2 - (r+h-H)^2}, \tag{9}$$

$$T = \frac{9550P}{n}. \tag{10}$$

In Eq. (10), T is the motor torque and n the motor speed. Incorporating Eqs. (6) to (10) into Eq. (5) solves Eq. (11):

$$\frac{9550P}{3n(R-h)\sqrt{r^2-(r+h-H)}\tan\theta \cdot \sin\theta} \geq \frac{F_0 + kh}{r+h-H}. \tag{11}$$

In Eq. (11), P is the motor power, R is the inner diameter of the pipe, F_0 is the spring preload, and k is the spring stiffness coefficient. According to Eq. (11), during the process in which the driving unit crosses the welding seam, the spring is a standard part, and the spring preload and stiffness coefficient are only related to the properties of the selected spring. The parameters do not change when the attribute is determined, the pipe radius and the wheel's radius do not change, and the convex height of the welding seam remains unchanged. Under this working condition, the main factors that affect the obstacle passage of the robot are the motor torque and the deflection angle of the driving wheel.

During the obstacle-crossing operation of the drive unit, when the steering gear deflection angle is kept constant, the torque of the drive motor is reduced, and the obstacle passing performance is improved. This means that the motor speed can be reduced to increase the obstacle-crossing ability of the drive unit.

When keeping the motor speed constant, the deflection angle of the driving wheel can be adjusted to change the obstacle-crossing ability of the robot. tanθ increases monotonically in the range of 0° to 90°, and sinθ also increases monotonically in the 0° to 90° interval, so tanθ·sinθ increases in this interval. Therefore, the obstacle-climbing ability of the robot can be improved to a certain extent by appropriately reducing the deflection angle of the driving wheel.

When the supporting wheel crosses the welding seam barrier, the driving wheel has already passed the welding seam. The driving wheel provides traction for the supporting wheel to pass the obstacle, and the obstacle-crossing process of the supporting wheel is analysed. The diagram for model analysis is shown in Fig. 8. When the support wheel crosses the weld seam, it will contact the weld seam. The contact point is set as O_1. The weld will give the support wheel a corresponding support force N. The spring has a vertical downward force F_S on the support wheel. The friction between the support wheel and the pipe is F_f, and F is the traction force of the robot.

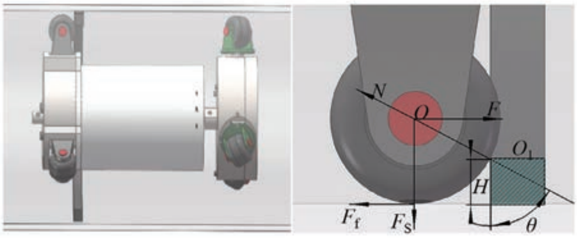

Fig. 8. *Analysis diagram of the supporting wheel obstacle-crossing process*

For the support wheel to cross the weld smoothly, the following conditions must be met, as shown in Eqs. (12) and (13):

$$\sum M(O_1) \ge 0, \tag{12}$$

$$F\cdot(R-H)+F_f\cdot H \ge F_s\cdot\sqrt{R^2-(R-H)^2}. \tag{13}$$

When the support wheel crosses the obstacle, the friction force of the pipe on it is 0, which is brought into Eq. (13) and simplified to obtain Eq. (14):

$$F \ge F_s\frac{\sqrt{R^2-(R-H)^2}}{R-H}. \tag{14}$$

According to Eq. (14), increasing the traction force can improve the robot's ability to cross the weld seam during the obstacle course of the support wheel. According to Eq. (6), when the deflection angle of the driving wheel decreases, the traction force will increase accordingly. According to Eqs. (11) and (14), when the deflection angle of the driving wheel is constant, reducing the motor speed can also increase traction.

In summary, when the robot crosses obstacles, the main factors that affect the robot's obstacle-crossing performance are motor speed and driving wheel deflection angle. During the work of the adaptive pipeline plugging repair robot, the passing performance of the robot at obstacles such as welds in the pipe can be increased by reducing the motor speed or reducing the deflection angle of the driving wheel.

3 SIMULATION ANALYSIS OF ROBOT DRIVER UNIT

3.1 Simulation Analysis of the Running Speed of the Drive Unit in a Straight Pipeline

A dynamic simulation analysis is performed with ADAMS software [37] and [38]. During the simulation, when the driving unit is running in a straight pipe, the deflection angle of the driving wheel is adjusted by the angle-adjusting steering gear, and the rotation angles of the three driving wheels need to be consistent. The selection range of the deflection angle is from 0° to 90°, every 5° is a sampling point, and the motor speed is set to 30 r/min. The simulation result is shown in Fig. 9.

When the deflection angle of the driving wheel is from 5° to 45°, the speed of the drive unit increases continuously. When the rotation angle is 45°, the travel speed is the highest, and the speed is 0.051 m/s. The speed increase gradually slows down from 30° to 45° because of the side of the driving wheel. The resistance to the pipeline will gradually increase, but the driving force is still greater than the resistance.

When the deflection angle is from 45° to 90°, the speed decreases continuously and is unstable. Due to the axial friction between the driving wheel and the pipe, the speed of the drive wheel gradually decreases within 45° to 90°. In this range, the resistance is greater than the traction provided by axial motion, resulting in a decrease in speed. When it is between 15° and 40°, the speed increases smoothly, and the running effect is the best.

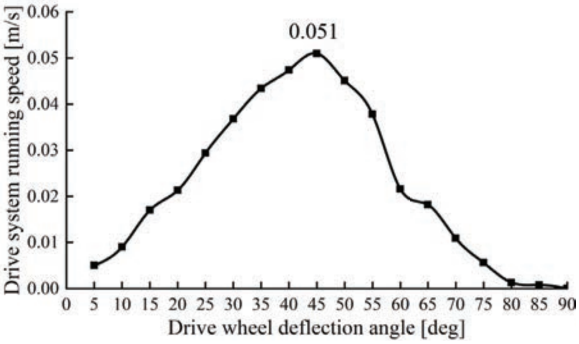

Fig. 9. *Simulation value of the running speed of the drive unit in a straight pipe*

To meet the design requirements, the operating speed of the robot should be within the range of 15° to 40°, and the actual operating index can also be higher than the design index. From the speed simulation diagram of the robot running in the straight pipe, it can be seen that the running speed of the robot increases with the increase of the deflection angle within a certain range. Therefore, based on the simulation results, it is better to adjust the deflection angle of the robot driving wheel in the range of 15° to 40° in the actual running process to reach a better working condition.

3.2 Simulation Analysis of the Traction Force of the Driving Unit Running in a Straight Pipeline

In the simulation analysis of the traction force experienced by the drive unit in straight pipe operation, it can be seen from the previous section that it is better to set the deflection angle of the drive wheel from 15° to 40° and simulate and fit the drive wheel angle and the traction force. The simulation diagram is shown in Fig. 10.

When the driving wheel angle of the driving unit is set between 15° and 45°, the simulation diagram shows that the relationship between the driving wheel angle and the traction force of the robot is negatively correlated. As the driving wheel angle increases, the traction force gradually decreases. The reason is that when the deflection angle increases, the axial friction force of the driving body increases, resulting in a smaller traction force along the pipe axis. When the deflection angle is 45°, the traction force is less than 20 N, which does not meet the actual design requirements. Therefore, by comparing with the deflection angle range obtained by simulation, it can be seen that setting the working deflection angle of the driving unit within the range from 15° to 40° has the best effect.

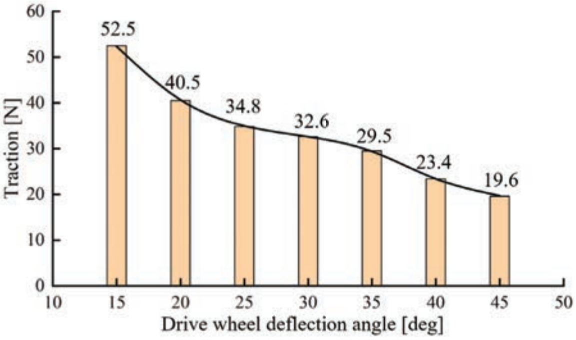

Fig. 10. *Traction simulation diagram of traction robot*

3.3 Simulation Analysis of Obstacle Surmounting Stability of the Drive Unit

In this simulation process, the weld of the pipe is set to 3 mm. Set the speed of the spindle motor of the drive unit to 30, and the range of deflection angle is from 15° to 40°. Taking the centroid of the driving unit as the reference point, the stability of obstacle crossing is judged by analysing the offset displacement of the centroid on the *y*-axis. Take points every 5° as a simulation value from the moment that the driving wheel contacts the weld to when the rear wheel completely leaves the weld. Starting from the driving wheel just contacting the weld, adjust the deflection angle of the driving wheel to 15°, and carry out a simulation to obtain the centroid offset displacement of the robot. Then, add 5° each time. The deflection angles of the driving wheel are selected as 20°, 25°, 30°, 35°, and 40° respectively for simulation. The simulation diagram is shown in Fig. 11.

Fig. 11 is analysed; Fig. 11a shows a running diagram with a deflection angle of 15° and a speed of 30 r/min. It can be seen that the *y*-axis displacement slowly climbs within 1 second to 1.7 seconds. In addition, Figs. 11b to f show all the crossed obstacles from 1 second to 1.5 seconds. The reason for the analysis is that under this working condition, the traction robot has too small a driving wheel deflection

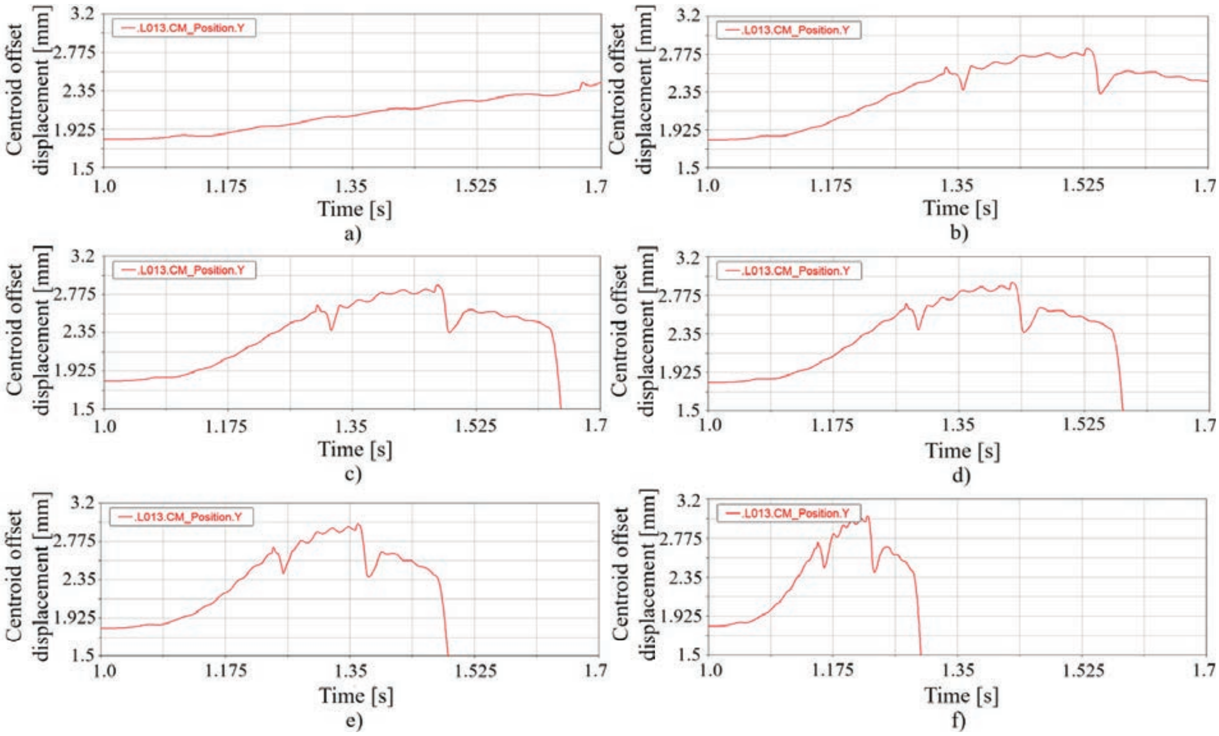

Fig. 11. *Simulation diagram of obstacle-crossing stability of traction robot with different rotation angles at the same speed 30 r/min; a) 15 deg, b) 20 deg, c) 25 deg, d) 30 deg, e) 35 deg, f) 40 deg*

angle, the wheel rim and the welding seam have large circumferential friction, and the axial traction is small. Although this approach can continuously improve the position of the centre of mass of the robot, it can never pass the welding seam. Therefore, it can be judged that the traction robot cannot cross the welding seam when the driving wheel angle is 15° and can pass the welding seam at 20° to 40°. Then, the obstacle-crossing stability is analysed when the driving wheel angle is 20° to 40°. It can be seen in the figure that as the deflection angle of the driving wheel increases, the fluctuation amount also increases, and the stability of obstacle crossing continues to deteriorate. When the deflection angle of the driving wheel is 20°, the obstacle crossing is the most stable.

3.4 Simulation Analysis of the Maximum Obstacle Surmounting Height of the Driving Unit

The internal environment of a pipeline is complex and diverse. When the drive unit traverses the pipeline, it may need to cross obstacles of different heights [39] and [40]. In the analysis of the previous section, we use a weld of 3 mm as an obstacle condition for analysis. By adjusting the deflection angle of the driving wheel, it is found that the driving unit can pass through the weld smoothly. This simulation takes a 150 mm pipeline as the object and sets the height of the weld to 5 mm for analysis to test the passability of the robot. The drive unit parameters are set as follows: the deflection angle of the drive wheel is 20°, and the motor speed is 30 r/min. The simulation is carried out when the driving wheel crosses the 5 mm weld seam, and the simulation result is shown in Fig. 12.

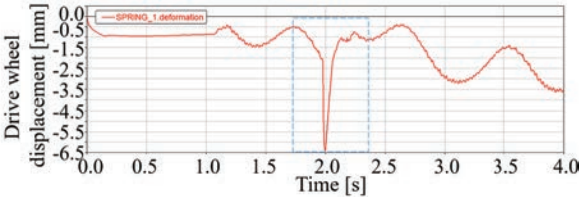

Fig. 12. *Simulation diagram of driving unit by 5 mm weld*

The process of crossing obstacles takes 1.5 s to 2.5 s. At this time, the spring is compressed and contracted, and the drive wheel shifts upward. The upward displacement of the driving wheel during the obstacle course is approximately 5.5 mm. Because the robot can be designed to meet the diameter change in the range of 20 mm, the drive unit can pass the 5 mm weld under this working condition to meet the design requirements. Second, under the condition that

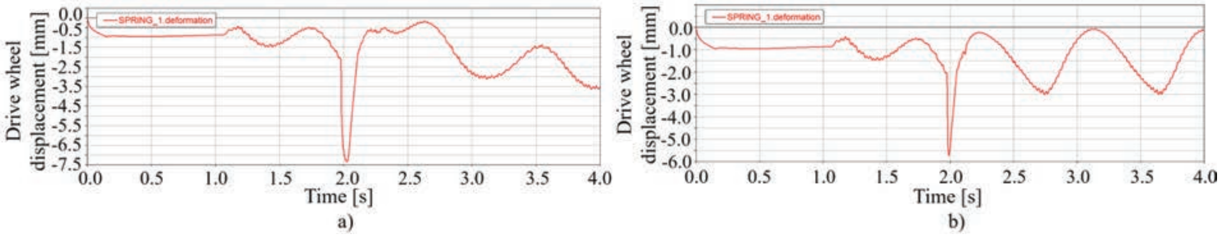

Fig. 13. *Simulation diagram of the driving unit through a) 6 mm, and b) 7 mm welds*

the parameter setting is unchanged and the working conditions are the same, the weld height is set to 6 mm and 7 mm. Under these two conditions, a simulation analysis of the drive unit's passability is performed. The simulation diagram is shown in Fig. 13.

It can be seen in Fig. 13a that when the drive unit passes through the 6 mm weld seam, the maximum displacement of the drive wheel is 6.5 mm. Therefore, the drive unit can pass the 6 mm weld seam smoothly. It can be seen in Fig. 13b that when the drive unit passes through the 7 mm weld seam, the maximum offset displacement cannot exceed 7 mm. Combined with the simulation, it can be seen that the 7 mm weld seam jams the drive unit driving wheel, and the drive body continues to rotate after being jammed, causing the displacement of the driving wheel to perform periodic motion under the action of spring force and gravity.

From the above analysis, it can be concluded that the maximum obstacle-crossing height that the drive unit can pass smoothly is 6 mm, which meets the design requirements.

4 EXPERIMENTAL VERIFICATION

A prototype of an adaptive plugging robot for buried pipeline leakage is manufactured and assembled in full accordance with the above design requirements, as shown in Fig. 14.

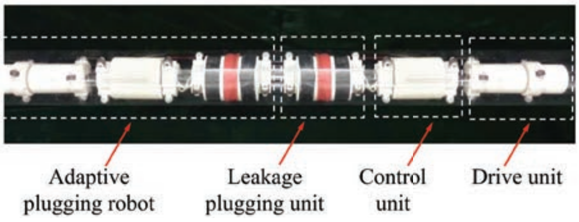

Fig. 14. *Prototype of an adaptive plugging robot for buried pipeline leakage*

The mass of the driving unit was measured to obtain 1.3 kg, the total mass of a single set of adaptive plugging robots was 3.5 kg, the overall mass of the two sets of robots was 7 kg, the length of the drive unit was 230 mm, the length of a single adaptive plugging robot was 765 mm, and the length of the combined robot was 1530 mm. The control unit mainly controls the steering gear of the driving wheel, the motor, the drainage valve, the airbag deflation valve and the airbag inflator.

The results of a speed test for the prototype are shown in Fig. 15. It can be seen in the figure that the running speed curve of the prototype obtained during the test is roughly the same as the curve of the simulation analysis, but the result of the simulation analysis is always greater than the experimental result.

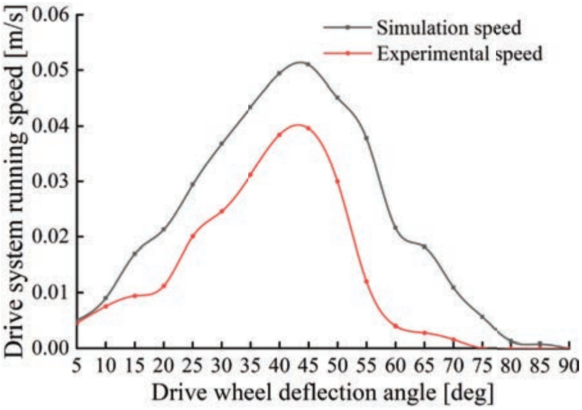

Fig. 15. *Comparison of running speed of test prototype*

It can be seen from the operating speed comparison chart that when the deflection angle is between 5° and 45°, the deflection angle of the drive wheel gradually increases, and the speed of the prototype also increases. The speed of the prototype reaches its peak at 45°, and the peak speed is approximately 0.039 m/s. This result also meets the design requirements.

When testing the traction force of the prototype, it is necessary to use a spring dynamometer for measurement. The spindle speed of the drive unit is set to 30 r/min, the drive wheel angle is set to 15° to 45°

in turn, the system is started, and the drive unit drags the leakage plugging unit and the control unit forward until it is completely pulled by the dynamometer, which reads the dynamometer and indicates the number. The comparison between the experimental result and the simulation is shown in Fig. 16.

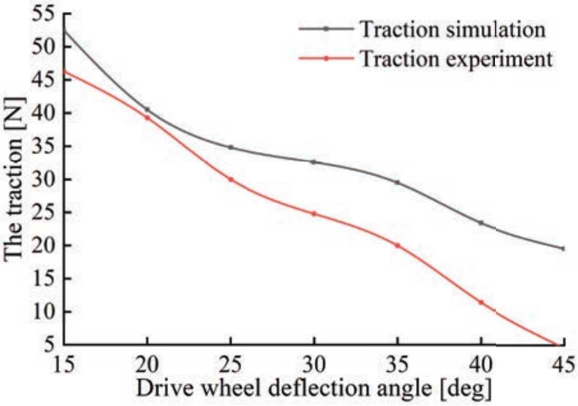

Fig. 16. *Comparison diagram of driving force test of prototype*

Comparing the simulation results with the experimental results, it can be concluded that the trends of the two curves are roughly the same, which proves the correctness of the simulation results. It can be seen in Fig. 16. that the experimental value is always lower than the simulation value. The reason for this phenomenon is that the simulation is moving under ideal conditions, and the design and installation of the experimental prototype and the experimental environment will have certain accuracy errors. After the deflection angle of the drive wheel is greater than 20°, the gap between the simulation results and the experimental results is larger than before, mainly because as the speed continues to increase, the impact of the assembly accuracy of the drive system on the operating state gradually appears. When the deflection angle is 35°, the traction force is 20 N, which is the most basic requirement of the design. In the simulation analysis, 20 N is reached at 40°. The assembly accuracy of the prototype has a significant impact on its specific operating state. Therefore, based on the original simulation conclusions, the upper limit of deflection angle during stable operation of the system shall be further reduced from 40° to 35°. The lower limit of deflection angle during stable operation of the system is 20°.

The obstacle-crossing ability test of the prototype adopts the driving unit test method. The obstacle-crossing ability test is carried out in a 2000 mm straight pipe. Several rubber sealing rings are bound and bonded on the inner wall of the pipeline to simulate obstacles, and the main protrusion heights are 5 mm, 6 mm, and 7 mm, respectively. Because the friction coefficient between the outer surface of the rubber seal ring and the inner wall of the experimental pipe is almost the same, the simulation as an obstacle is close to the real obstacle. The simulation results show that the drive unit can pass by 6 mm welds, so the test directly simulates 5 mm, 6 mm, and 7 mm welds to test the possibility of the prototype. The experimental environment is shown in Fig. 17.

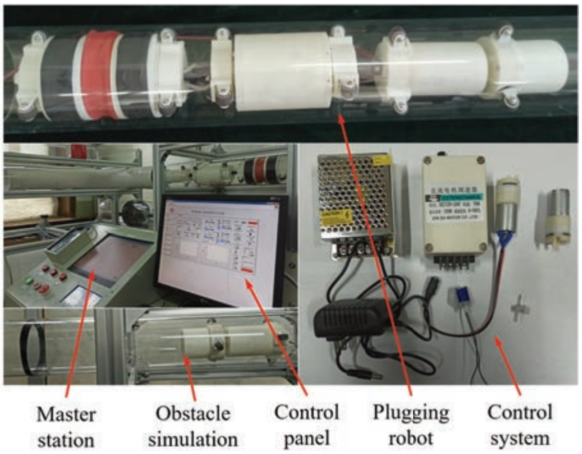

Fig. 17. *Test diagram of the obstacle-crossing ability of the test prototype*

The results of the prototype's obstacle-crossing capability are shown in Table 2.

An analysis of Table 2. shows that when the driving wheel rotation angle is set to 15°, the angle formed between the outer surface of the driving wheel and the obstacle is too small, which results in slipping and an inability to cross the obstacle. Therefore, 20° is the minimum passing angle when the driving wheel crosses the obstacle, which is consistent with the simulation results. When the driving wheel angle of the prototype is 20°, it can pass 6 mm obstacles but cannot pass 7 mm obstacles.

Table 2. *Obstacle clearance results for prototype*

Height Angle	5 mm	6 mm	7 mm
15°	Unpassable	Unpassable	Unpassable
20°	Accessible	Accessible	Unpassable
25°	Accessible	Accessible	Unpassable
30°	Accessible	Pass after multiple skidding	Unpassable
35°	Accessible	Unpassable	Unpassable

Although 25° can pass 6 mm obstacles, the exercise state is not good and cannot pass 7 mm obstacles. At 30°, the drive unit has difficulty passing the 6 mm obstacle. When the running speed increases, the manufacturing accuracy and installation accuracy of parts are low due to the assembly process of the prototype. The vibration and centroid fluctuation of the prototype robot for adaptive plugging and repairing pipeline are large, which reduce the ability to overcome obstacles. The camera shakes more severely at 35° and cannot pass 6 mm obstacles.

In the simulation results, when the prototype passes through the welding seam, the driving wheel deflection angle is set to 20°, and when the motor speed is 30 r/min, the maximum obstacle height that can be passed is 6 mm. The experiment is consistent with the simulation results.

5 CONCLUSIONS

(1) To meet the design requirements, the robot uses a multi-body distributed structure in which each unit is connected in series. The main body connects two sets of adaptive plugging robots with electromagnetic adsorption modules. The self-adaptive plugging robot is composed of a drive unit, a control unit, and a leak-plugging unit, and each unit is connected by a parallel coupling. The drive unit adopts the driving form of a motor drive and spiral travel, incorporates the expansion and contraction of the spring to match the diameter, and uses a corrugated airbag to complete the plugging.

(2) Through an analysis of the obstacle-crossing mechanism of the robot, it is concluded that reducing the rotational speed of the motor or reducing the deflection angle of the driving wheel can increase the passing performance of the robot at obstacles such as welds in the pipe.

(3) A prototype is assembled, and related experiments are conducted to determine that the overall structure of the prototype meets the design requirements. The traction force and obstacle-crossing ability of the prototype are verified experimentally. The results show that the running index meets the design requirements when the driving wheel deflection angle is set at 20° to 35°. The deflection angle of the driving wheel is in this range; the smaller the angle is, the better the running effect is, and the best running angle is 20°. Under the best operating conditions, the maximum obstacle height of the prototype is 6 mm.

(4) The design of the buried pipeline leakage self-adaptive plugging robot provides an important reference for the research and development of equipment in the field of pipeline leakage emergency prevention and control.

6 ACKNOWLEDGEMENTS

The work described in this paper was supported by a research project supported by the Shanxi Scholarship Council of China (2020-110), the Fundamental Research Program of Shanxi Province (20210302123038) and the National Natural Science Foundation of China (52174147). The authors would like to express their gratitude for the support of this study. Moreover, the authors sincerely thanks Professor Wu Wenge of North University of China for his critical discussion and Dr. Dahua Xie of Silicon Valley USA for linguistic assistance during the preparation of this manuscript. At the same time, we accepted the professional language editing service of American Journal Experts (AJE).

7 REFERENCES

[1] Witkowski, A., Rusin, A., Majkut, M., Stolecka, K. (2018). Analysis of compression and transport of the methane/hydrogen mixture in existing natural gas pipelines. *International Journal of Pressure Vessels and Piping*, vol. 166, p. 24-34, **DOI:10.1016/j.ijpvp.2018.08.002**.

[2] Zeng, J., Sun, C.X., Zhu, Z.J., Wu, J.L., Chen H.S. (2018). Uncertainty analysis for natural gas transport pipeline network layout: a new methodology based on Monte Carlo method. *Journal of Advanced Transportation*, vol. 2018, art. ID 9213648, **DOI:10.1155/2018/9213648**.

[3] Li, M., Liu, L.L., Li, Y., Xu Y.C. (2018). Evaluating the risk of natural gas pipeline operation management in intuitionistic fuzzy linguistic environments. *Mathematical Problems in Engineering*, vol. 2018, art. ID 3960496, **DOI:10.1155/2018/3960496**.

[4] Vasseghi, A., Haghshenas, E., Soroushian, A., Rakhshandeh, M. (2020). Failure analysis of a natural gas pipeline subjected to landslide. *Engineering Failure Analysis*, vol. 119, art. ID 105009, **DOI:10.1016/j.engfailanal.2020.105009**.

[5] Deng, Y.J., Hu, H.B., Yu, B., Sun, D.L., Hou, L., Liang, Y.T. (2017). A method for simulating the release of natural gas from the rupture of high-pressure pipelines in any terrain. *Journal of Hazardous Materials*, vol. 342, p. 418-428, **DOI:10.1016/j.jhazmat.2017.08.053**.

[6] Mahmoodzadeh, Z., Wu, K.Y., Droguett, E.L., Mosleh, A. (2020). Condition-Based maintenance with reinforcement learning for dry gas pipeline subject to internal corrosion. *Sensors*, vol. 20, no. 19, art. ID 5708, **DOI:10.3390/s20195708**.

[7] Dong, F.F., Bie, X.M., Tian, J.P., Xie, X.D., Du, GF. (2019). Experimental and numerical study on the strain behavior of buried pipelines subjected to an impact load. *Applied Sciences*, vol. I9, no. 16, art. ID 3284, **DOI:10.3390/app9163284**.

[8] Zhang, D.F., Bie, X.M., Zeng, X., Lei, Z., Du, G.F. (2020). Experimental and numerical studies on mechanical behavior of buried pipelines crossing faults. *Structural Engineering and Mechanics*, vol. 75, no. 1, p. 71-89, **DOI:10.12989/sem.2020.75.1.071**.

[9] Liang, Z.D., Jeng, D.S., Liu, J.W. (2020). Combined wave-current induced seabed liquefaction around buried pipelines: Design of a trench layer. *Ocean Engineering*, vol. 212, art. ID 107764, **DOI:10.1016/j.oceaneng.2020.107764**.

[10] Yan, H.W., Wang, L., Li, P.C., Wang, Z.J., Yang, X., Hou, X.R. (2020). Research on passing ability and climbing performance of pipeline plugging robots in curved pipelines. *IEEE Access*, vol. 8, p. 173666-173680, **DOI:10.1109/ACCESS.2020.3025560**.

[11] Wang, W.M., Liu, X., Wang, H., Fan, J.C., Zhu, X.X. (2018). Pose overshoot analysis of the marine spherical double plugging in twisting process. *Proceedings of The Institution of Mechanical Engineers Part M-Journal of Engineering for The Maritime Environment*, vol. 232, no. 2, p. 245-252, **DOI:10.1177/1475090217722307**.

[12] Cheng, F., Liu, J.P., Wang, J., Yang, Z.D., Abbasi S.S., Tian, Z.J., Xu. H. (2018). Locating leaking buried pipes based on ground micro seismic records in 3D space. *Surveys in Geophysics*, vol. 39, no. 5, p. 993-1007, **DOI:10.1007/s10712-018-9479-x**.

[13] Kakogawa, A., Nishimura, T., Ma, SG. (2016). Designing arm length of a screw drive in-pipe robot for climbing vertically positioned bent pipes. *ROBOTICA*, vol. 34, no. 2, p.306-327, **DOI:10.1017/S026357471400143X**.

[14] Kim, K.T., Kim, H.W., Sik, K.Y., Chang H.Y., Bu, T.B., Park, H. (2015). Real-time corrosion control system for cathodic protection of buried pipes for nuclear power plant. *Corrosion Science and Technology*, vol. 14, no. 1, p. 12-18, **DOI:10.14773/cst.2015.14.1.12**.

[15] Zhang, C.Y., Chen, G.Z., Miao, C.W., Tang, Y.J., Bai, N. (2020). Driving pulsation analysis of electro-hydraulic robot. *Journal of Advanced Mechanical Design Systems and Manufacturing*, vol. 14, no. 1, **DOI:10.1299/jamdsm.2020jamdsm0012**.

[16] Han, M., Zhao, F., San D., Zhai K.D., Wang D., Zhou, J. (2017). Structural design and driving force analysis of a nuclear pipeline robot. *Electromechanical Engineering*, vol. 34, no. 07, p. 696-701, **DOI:10.3969/j.issn.1001.4551.2017.07.002**.

[17] Zhao, W., Kamezaki, M., Yoshida, K., Yamaguchi, K., Konno, M., Onuki, A., Sugano, S. (2019). A coordinated wheeled gas pipeline robot chain system based on visible light relay communication and illuminance assessment. *Sensors*, vol. 19, no. 10, art. ID 2322, **DOI:10.3390/s19102322**.

[18] Liu Q.Y., Li, Y.J., Ren, T., Chen, Y.H. (2014). Active screw driven pipeline robot. *Robot*, vol. 36, no. 6, p. 711-718, **DOI:10.13973/j.cnki.robot.2014.0711**.

[19] Tu, Q., Liu, Q.Y., Ren, T., Li, Y.J. (2019). Obstacle crossing and traction performance of active and passive screw pipeline robots. *Journal of Mechanical Science and Technology*, vol. 33, no. 5, p. 2417-2427, **DOI:10.1007/s12206-019-0440-9**.

[20] Li, P., Tang, M., Lyu, C.Y., Fang, M.J., Duan, X.G., Liu, Y.H. (2018). Design and analysis of a novel active screw-drive pipe robot. *Advances in Mechanical Engineering*, vol. 10, no. 10, **DOI:10.1177/1687814018801384**.

[21] Kakogawa, A., Nishimura, T., Ma, S. (2016). Designing arm length of a screw drive in-pipe robot for climbing vertically positioned bent pipes. *Robotica*, vol. 34, no. 2, p. 306-327, **DOI:10.1017/S026357471400143X**.

[22] Nishimura, T., Kakogawa, A., Ma, S. (2013). Improvement of a screw drive in-pipe robot with pathway selection mechanism to pass through T-branches. Journal of Robotics and Mechatronics, vol. 25, no. 2, p. 340-346, **DOI:10.20965/jrm.2013.p0340**.

[23] Wang, Y.F., Pandit, P., Kandhari, A., Liu, Z.H., Daltorio, K.A. (2020). Rapidly exploring random tree algorithm-based path planning for worm-like robot. *Biomimetics*, vol. 5, no. 2, art. ID 26, **DOI:10.3390/biomimetics5020026**.

[24] Jeon, W., Kim, I., Park, J., Yang, H. (2013). Design and control method for a high-mobility in-pipe robot with flexible links. *The Industrial Robot*, vol. 40, no. 3, p. 261-274, **DOI:10.1108/01439911311309960**.

[25] Lu, X.J., Wang, K., Hu, T.T. (2020). Development of an annelid-like peristaltic crawling soft robot using dielectric elastomer actuators. *Bioinspiration & Biomimetics*, vol. 15, no. 4, **DOI:10.1088/1748-3190/ab8af6**.

[26] Mishra, D., Yadav, R.S., Agrawal, K.K. (2020). Kinematic modelling and emulation of robot for traversing over the pipeline in the refinery. *Microsystem Technologies*, vol. 26, no. 3, p. 1011-1020, **DOI:10.1007/s00542-019-04615-9**.

[27] Zagler, A., Pfeiffer, F. (2003). “MORITZ” a pipe crawler for tube junctions. *Proceedings - IEEE International Conference on Robotics and Automation*, vol. 3, p. 2954-2959, **DOI:10.1109/ROBOT.2003.1242044**.

[28] Aleksandersen, J., Tveit, E. (2001). The smart plug: A remotely controlled pipeline isolation system. *Proceedings of the International Offshore and Polar Engineering Conference*, vol. 2, p. 192-199.

[29] Yan, H.W., Yang, X., Hou, X.R., Wang, L., Li, P.C. (2020). Research on the performance of a new external occlusion device for pressure vessel leakage. *Strojniški vestnik - Journal of Mechanical Engineering*, vol. 66, no. 11, p. 668-676, **DOI:10.5545/sv-jme.2020.6810**.

[30] Bowie, A. (2012). A comparison of double block and bleed technologies. *Proceedings of the Biennial International Pipeline Conference*, vol 1, p. 425-439, p. 9780791845127, **DOI: 10.1115/IPC2012-90020**.

[31] An, Y., Wang, X.C., Yue, B., Qu, Z.G., Wu, L.Q., Chu, R.H. (2019). Compensation of sound velocity variation based on resampling algorithm for natural gas pipeline safety monitoring. *Measurement*, vol. 148, **DOI:10.1016/j.measurement.2019.106942**.

[32] Zhang, H.W., Zhang, S.T., Wang, Y.H., Liu, Y.H., Yang, Y.N., Zhou, T., Bian, H.Y. (2021). Subsea pipeline leak inspection by autonomous underwater vehicle. *Applied Ocean Research*, vol. 107, art. ID 102321, **DOI:10.1016/j.apor.2020.102321**.

[33] Cao, Y., Suzuki, S., Hoshino, Y. (2016). Uphill and level walking of a three-dimensional biped quasi-passive walking robot by torso control. *Robotica*, vol. 34, no. 3, p. 483-496, **DOI:10.1017/S0263574714001593**.

[34] Du, Q.L., Lu, X.P., Wang, Y.K., Liu, S.A. (2020). The obstacle-surmounting analysis of a pole-climbing robot. *International*

Journal of Advanced Robotic Systems, vol. 17, no. 6, **DOI:10.1177/1729881420979146**.

[35] Xi, F.Y., Jiang, Q.S. (2019). Dynamic obstacle-surmounting analysis of a bilateral-wheeled cable-climbing robot for cable-stayed bridges. *Industrial Robot: The International Journal of Robotics Research and Application*, vol. 46, no. 3, p. 431-443, **DOI:10.1108/IR-07-2018-0152**.

[36] Zhu, X.X., Wang, W., Zhang, S.M., Liu, S.H. (2017). Experimental research on the frictional resistance of fluid-driven pipeline robot with small size in gas pipeline. *Tribology Letters*, vol. 65, no. 2, **DOI:10.1007/s11249-017-0830-z**.

[37] Korayem, A.H., Irani, M., Babaee, H., Korayem, M.H. (2017). Maximum load of flexible joint manipulators using nonlinear controllers. *Robotica*, vol. 35, no. 1, p. 119-142, **DOI:10.1017/S0263574715000028**.

[38] Korayem, M.H., Dehkordi, S.F. (2018). Derivation of motion equation for mobile manipulator with viscoelastic links and revolute-prismatic flexible joints via recursive Gibbs-Appell formulations. *Robotics and Autonomous Systems*, vol. 103, p. 175-198, **DOI:10.1016/j.robot.2018.02.013**.

[39] Li, H., Li, R.Q., Zhang, J.W., Zhang, P.Y. (2020). Development of a pipeline inspection robot for the standard oil pipeline of China national petroleum corporation. *Applied Sciences*, vol. 10, no. 8, **DOI:10.3390/app10082853**.

[40] Ovalle-Magallanes, E., Aldana-Murillo, N.G., Avina-Cervantes, J.G., Ruiz-Pinales, J., Cepeda-Negrete, J., Ledesma, S. (2021). Transfer learning for humanoid robot appearance-based localization in a visual map. *IEEE Access*, vol. 9, p. 6868-6877, **DOI:10.1109/ACCESS.2020.3048936**.

Strojniški vestnik - Journal of Mechanical Engineering 68(2022)1, 27-38

DOI:10.5545/sv-jme.2021.7288
Original Scientific Paper
Received for review: 2021-06-11
Received revised form: 2021-11-06
Accepted for publication: 2021-12-06

Detection of Outer Wall Defects on Steel Pipe Using an Encircling Rotating Electromagnetic Field Eddy Current (RoFEC) Technique

Xiaokang Yin* – Zhuoyong Gu – Wei Wang – Xiaorui Zhang – Xin'an Yuan –Wei Li – Guoming Chen
Centre for Offshore Engineering and Safety Technology, China University of Petroleum (East China), China

In recent years, the rotating electromagnetic field eddy current (RoFEC) testing technique has attracted widespread attention due to its various advantages for inspecting tubular structures. However, most of the related work was focused on detecting inner wall defects on metal pipes using feed-through probes, which are often not applicable for outer wall defect detection. This work pushes forward the encircling RoFEC technique and demonstrates its feasibility for detecting outer wall defects. First, the basic principle of the encircling RoFEC technique is introduced. A three-dimensional finite element (FE) model was built in COMSOL to analyse the distribution of the rotating electromagnetic field and study the interaction between the defects and eddy currents. The axial component of the resultant magnetic field due to defects was selected as a characteristic signal and obtained from the FE models to study the factors, including pipe tilt, defect circumferential location, defect orientation and defect size, that influence the detection performance. An encircling RoFEC system using a probe with six excitation windings and a single bobbin pickup coil was constructed and used to inspect a steel pipe with one axial and one circumferential defect. The obtained voltage signal due to defects can form a Lissajous pattern in the impedance plane and be used for defect evaluation. The results showed that the encircling RoFEC technique can detect outer wall defects of both orientations and determine the circumferential location of the defect.

Keywords: non-destructive testing, rotating electromagnetic field, finite element, influencing factors

Highlights

- *An encircling rotating electromagnetic field eddy current (RoFEC) technique is proposed to detect outer wall defects on a steel pipe.*
- *The encircling RoFEC technique is capable of detecting defects of arbitrary orientations on a steel pipe and determining its circumferential location.*
- *Finite element models are used to study the effects of pipe tilt, defect location, defect orientation and defect size on the inspection performance.*
- *An encircling RoFEC system was developed and used to inspect a steel pipe with both axial and circumferential defects to verify the feasibility of the proposed technique.*

0 INTRODUCTION

Steel pipes are widely used in the petroleum industry. In the process of long-term service, steel pipes are prone to defects, such as deformation, corrosion, and cracks [1], leading to the possible leakage of the conveying medium and/or failure of the whole structure [2]. Extensive efforts have been presented into the non-destructive evaluation (NDE) techniques capable of detecting defects in steel pipes, such as eddy current inspection [3] to [5], magnetic flux leakage inspection [6] and [7], ultrasonic guided wave inspection [8] and [9], etc. The above-mentioned techniques have been widely used in steel pipe inspection, but some of them have inherent limitations, e.g., traditional eddy current can only detect defects in the area under the probe; thus, circumferential and axial scanning are required to achieve full coverage; Some detection techniques, such as magnetic flux leakage and alternating current field measurement (ACFM), are more sensitive to cracks in certain directions. There is an increasing need for electromagnetic NDE methods that can thoroughly detect cracks in arbitrary directions, and many novel techniques have been proposed recently, such as circumferential eccentric eddy current probe [10], the array eddy current testing probe [11], etc. In recent years, the rotating electromagnetic field eddy current (RoFEC) method [12] has emerged as a useful NDE technique for plate-like structures [13] to [15], tubular structures [16] to [18], and welding seams [19] and [20].

Due to its unique advantages, e.g., the RoFEC technique is sensitive to defects of all orientations, it relies on the rotation of the probing field rather than the mechanical scan of the sensor to implement circumferential scan, and the phase information of the resultant signal can be used to determine the circumferential location of the defect, the RoFEC technique is particularly suitable for tubular structure inspection. A literature review reveals that the majority of related research focused on the detection of inner wall defects on pipes using feed-through probes

---

*Corr. Author's Address: China University of Petroleum (East China), 66 West Changjiang Road, Qingdao, China, Xiaokang.yin@upc.edu.cn

[19] to [22] and using the RoFEC technique for the detection of outer wall defects on steel pipes can only be found sporadically in literature. It is thus necessary to embark in-depth research on the feasibility of encircling RoFEC technique on the detection of outer wall defect on steel pipes, as for some steel tubular structures, e.g., the widely used coiled tubing in the oil and gas industry, defects on the outer wall are commonly seen and need to be detected.

For the detection of outer wall defects on steel pipes, this paper pushes forward the encircling RoFEC technique by systematically studying the influential factors. The working principle of the encircling RoFEC technique is presented. Three-dimensional finite element (FE) models were constructed to demonstrate the perturbation of the probing field due to defects. The effects of different influencing factors on the detection results of the external penetrating rotating electromagnetic field detection sensor are explored, the encircling RoFEC system is built, and the detection test of a pipe with two typical flaws is carried out. The experimental results are consistent with the finite element simulation results and used to verify the feasibility of the proposed technique.

1 PRINCIPLE OF THE ENCIRCLING RoFEC TECHNIQUE

Unlike conventional feed-through RoFEC probes [23] to [25], the proposed encircling RoFEC probe comprises at least three external excitation windings and a single receiving coil. The three excitation windings are evenly distributed (120 degrees apart) around the pipe in space, as shown in Fig. 1a. The windings are driven by a three-phase sinusoidal current source. Currents in the three windings are identical in amplitude, but 120° apart in phase angle, as shown in Eq. (1),

$$\begin{cases} i_A = I\sin\omega t \\ i_B = I\sin\left(\omega t - \frac{2}{3}\pi\right) \\ i_C = I\sin\left(\omega t + \frac{2}{3}\pi\right), \\ i_X = -i_A \\ i_Y = -i_B \\ i_Z = -i_C \end{cases} \tag{1}$$

where i_A, i_B and i_C correspond to the incoming sinusoidal alternating current of winding A, winding B, and winding C in Fig. 1a, respectively. Their amplitudes are the same, but the phase angles are 120° apart. i_X, i_Y and i_Z are the outgoing currents of winding A, winding B and winding C, respectively. I is the amplitude of sinusoidal alternating current, in [A], and ω is the frequency of the sinusoidal alternating current, in [Hz].

The magnetic fields (*Ba*, *Bb*, and *Bc*) generated by the windings are perpendicular to the plane of each winding, as shown in Fig. 1a. According to Eq. (1), the magnetic fields vary sinusoidally with 120° apart in phase angle. The three components synthesize a magnetic field **B** with a constant amplitude and rotate circumferentially at a speed related to the excitation voltage frequency, similar to that found in a three-phase induction motor. The rotating magnetic field **B** can then induce eddy currents that flow circularly around the radial axis. As shown in Fig. 1b, defects in any direction can disturb the eddy currents, thereby perturbing the secondary magnetic field, which can then be measured and used for defect evaluation. Note that the eddy currents also rotate circumferentially, offering full coverage of the pipe wall circumference.

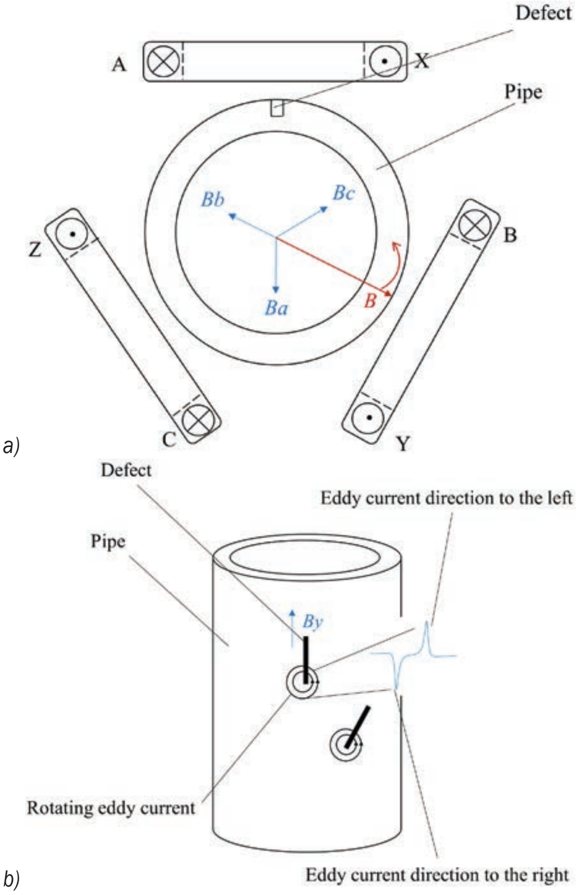

a)

b)

Fig. 1. *The FE model of rotating magnetic field; a) rotating magnetic field generation, and b) interaction of eddy currents and defects*

2 FE MODELLING OF THE ENCIRCLING RoFEC PROBE

2.1 The 3D FE Model

A three-dimensional FE model of the encircling RoFEC probe was built in COMSOL and shown in Fig. 2. In the FE model, six excitation windings were used for more evenly distributed rotating fields. The windings are evenly distributed around the pipe, and the material of the pipe is steel. The geometric parameters of the FE model and the characteristic parameters of the coil are shown in Tables 1 and 2. Fig. 3 shows the rotating magnetic field in the cross-section plane at different points in time ($T/6$, $T/3$, and $T/2$). T here refers to the time spent in a rotation cycle, that is, the time spent rotating the magnetic field around the tube, which is a fixed value.

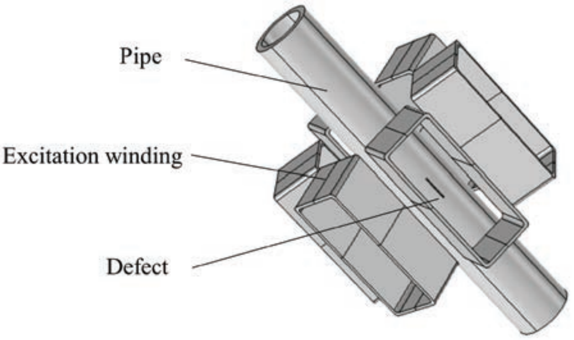

Fig. 2. *The FE model of rotating magnetic field*

Table 1. *Geometric parameters of the FE model*

Finite element model	Size [mm]
Inside and outside diameter of pipe	40/50
Length of pipe	150
Outer width of excitation winding	45
Inner width of excitation winding	40
Length of excitation winding	115
Thickness of excitation winding	40
Number of turns of the excitation windings	100
Length of defect	25
Width of defect	1
Air domain diameter	200

Table 2. *Characteristic parameters of the excitation windings*

Coil wire diameter [mm]	Coil turns	Excitation voltage [V]	Excitation frequency [kHz]
1	100	0.5	10

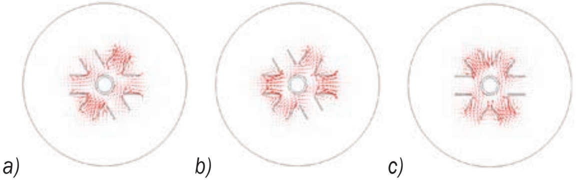
a) b) c)

Fig. 3. *Magnetic field in the x = 0 plane at different moments; a) time $T/6$, b) time $T/3$, and c) time $T/2$*

2.2 Characteristic Signal due to Defect

The excitation coil generates eddy current on the surface of the pipe, which also rotates around the axis at a certain speed depending on the frequency of the excitation. As shown in Fig. 4, when the eddy current encounters a defect (e.g., an axial crack), it will bypass each end of the defect and generate a secondary magnetic field. The resultant secondary magnetic field can then be measured and used to form indications of the defect. In theory, all components of the secondary magnetic field (axial, radial, and circumferential) can be used for defect detection and characterization. In this paper, the axial component was selected, as it can be easily measured by a single bobbin pickup coil. The advantages of such a measurement scheme will be further analysed in the experimental section.

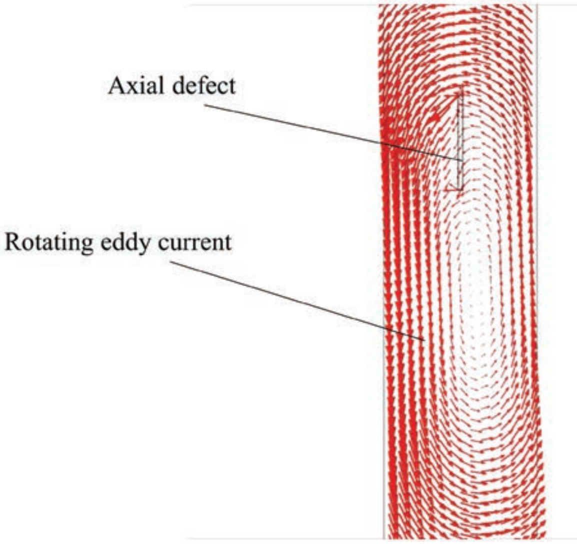

Fig. 4. *Interaction of eddy currents and defects*

In the FE model, the defect was moved across the windings to simulate an axial scan, and the axial magnetic field at 1mm above the defect is extracted and plotted as the characteristic signals, as shown in Fig. 5. It can be seen that when there is no defect in the pipe, the real and imaginary parts of the axial magnetic field are both near zero. When the annular

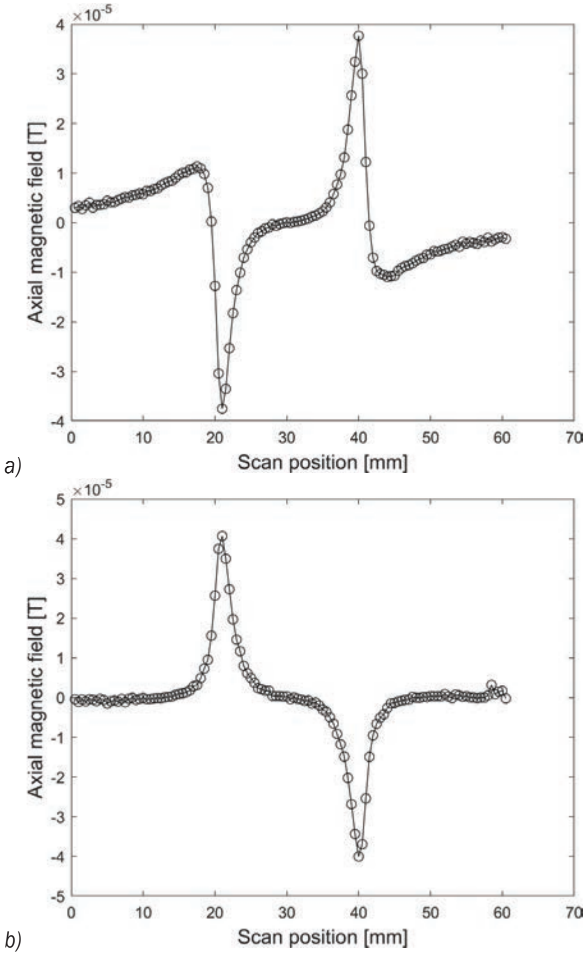

Fig. 5. *Real and imaginary parts of the characteristic signal; a) real part, and b) imaginary part*

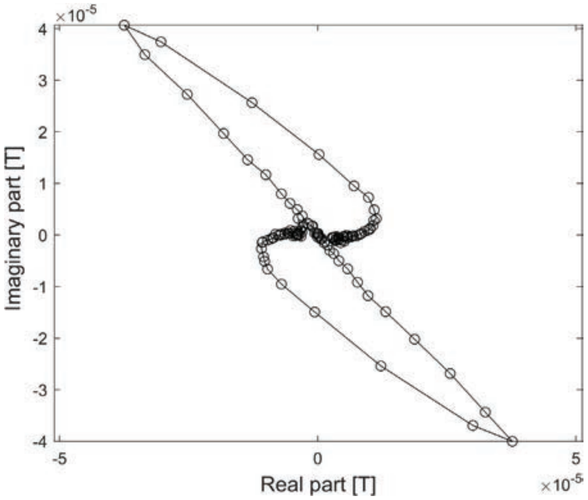

Fig. 6. *Real and imaginary part of the characteristic signal plotted as a Lissajous pattern in the impedance plane*

eddy current flows to the left, a wave trough is generated. When it flows to the right, a wave crest is generated. The real and imaginary parts of the axial magnetic field are plotted as a Lissajous pattern in the impedance plane, as shown in Fig. 6. Note that, as demonstrated in the experimental section, such a magnetic field can be measured by a circumferential bobbin coil around the pipe and used for defect evaluation.

3 FE MODEL-BASED ANALYSIS ON THE INFLUENCING FACTORS

Influencing factors of the RoFEC technique were then studied using the FE model, and the findings can be used to guide subsequent experiments.

3.1 Effects of Pipe Tilt

Considering that the pipe tilt during the actual inspection process, which will affect the inspection results, it is necessary to study the effects of the pipe tilt on defect detection. Fig. 7 shows the case in which the defective side of the pipe is inclined to the *x*-axis.

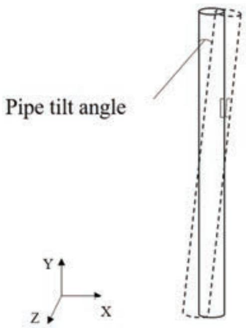

Fig. 7. *Schematic diagram of pipe inclining along the x-axis*

When the inclination angle of the pipe is set to 3°, 6°, 9°, 12° and 15°, the defects are detected and the characteristic signals (real part of the axial magnetic field 1mm above the defect) are extracted, as shown in Fig. 8. It can be seen from Fig. 8a that when the pipe is inclined to the x-axis, the value of the axial magnetic field peak is greater than the value of the trough because the defect is coming closer to the excitation windings. When the tilt angle is greater than 12°, the change is more significant. This is because the closer it is to the excitation windings, the more drastic the magnetic field changes. When the pipe is inclined to the z-axis, since the pipe is not inclined to the side of the inspection point, the peak value of the axial magnetic field is basically unchanged, as shown in Fig. 8b.

It can also be seen from both Figs. 8a and b that, no matter to which direction the pipe is tilted, the values of the axial magnetic field at defect-free positions (the starting point of each curve) are no longer zero. This is due to the change of the spatial background magnetic field caused by the inclination of the pipe, which generates the axial component of the magnetic field.

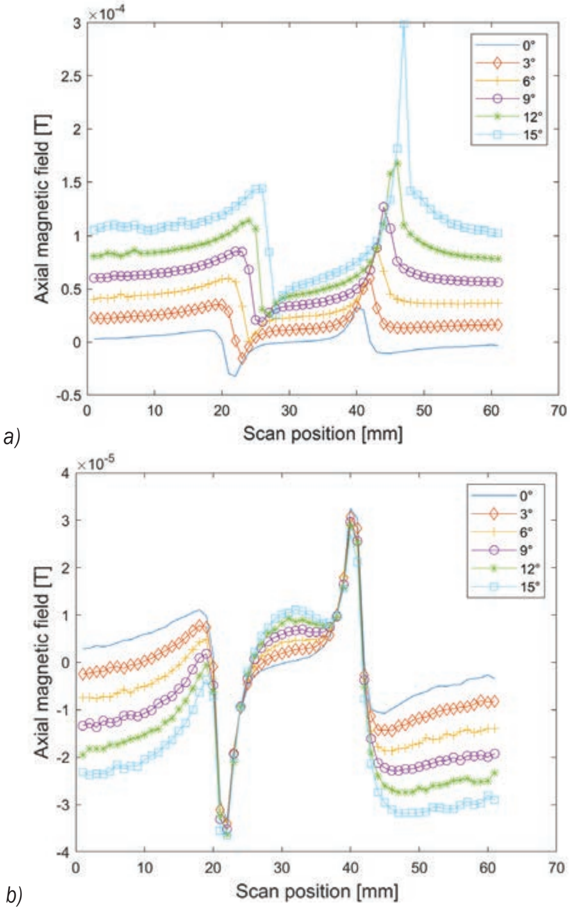

a)

b)

Fig. 8. *Characteristic signals (real part of the axial magnetic field) with different defect tilt angles; a) tilt towards the x-axis, and b) tilt towards the z-axis*

3.2 Effects of Circumferential Location of the Defect

Because possible defects may appear at any position of the pipe, it is necessary to study how the resultant magnetic field will vary with different circumferential locations of the defect. In the FE model, 8 axial defects with exactly the same size but at different circumferential locations (at angles of 0 degrees, 45 degrees, 90 degrees, 135 degrees, 180 degrees, 225 degrees, 270 degrees and 315 degrees with respect to the reference point) were scanned. The eight characteristic signals, due to the defects, are extracted and plotted as Lissajous patterns in the impedance diagram, as shown in Fig. 9. Note that, to avoid signal overlapping, only the first half of the characteristic signals are plotted for each Lissajous pattern. It can be seen from Fig. 9 that with the different circumferential locations of the defect on the outer wall of the pipe the angle of the Lissajous patterns also change accordingly, based on which the circumferential location of the defect can be determined. It can also be noted that all the Lissajous patterns are of similar size.

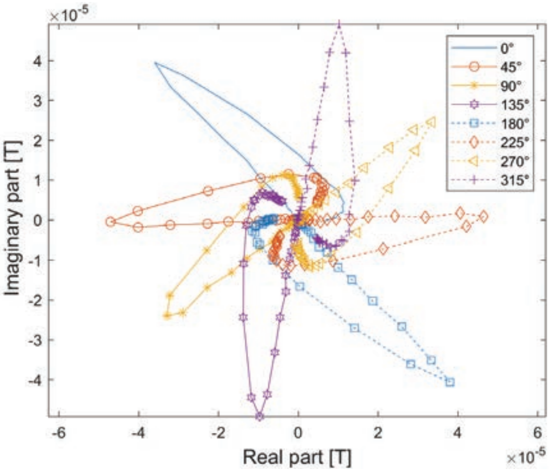

Fig. 9. *Lissajous Patterns for defects at different circumferential locations*

3.3 Effects of Defect Orientation

The effects of the orientations of the defect on the characteristic signal of the rotating electromagnetic field were also studied. Seven defects with 0-degree, 15-degree, 30-degree, 45-degree, 60-degree, 75-degree, and 90-degree orientations were introduced on the outer wall of the pipe in the FE model. As shown in Fig. 10, the defects are centred at the same point.

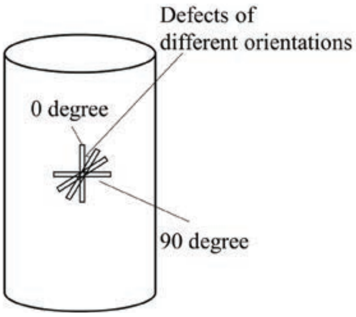

Fig. 10. *Schematic diagram of defects of different directions*

Fig. 11 shows the axial magnetic field of different defect orientations. It can be seen that only when the direction of the defect is 0 degrees or 90 degrees, the peak and trough of the axial magnetic field curve have the same absolute value. As the defect orientation changes from 0 degrees to 90 degrees, the absolute value of the peak of the axial magnetic field curve is greater than that of the trough. This phenomenon is most significant when the defect orientation is 45 degrees. The reason is that when the defect orientation is 45 degrees, the defect is affected by both the axial component and the circumferential component of the eddy current. At the same time, the distance between the peak and trough of the axial magnetic field keeps becoming closer. This set of FE models demonstrated that the encircling RoFEC technique is sensitive to defects of all orientations.

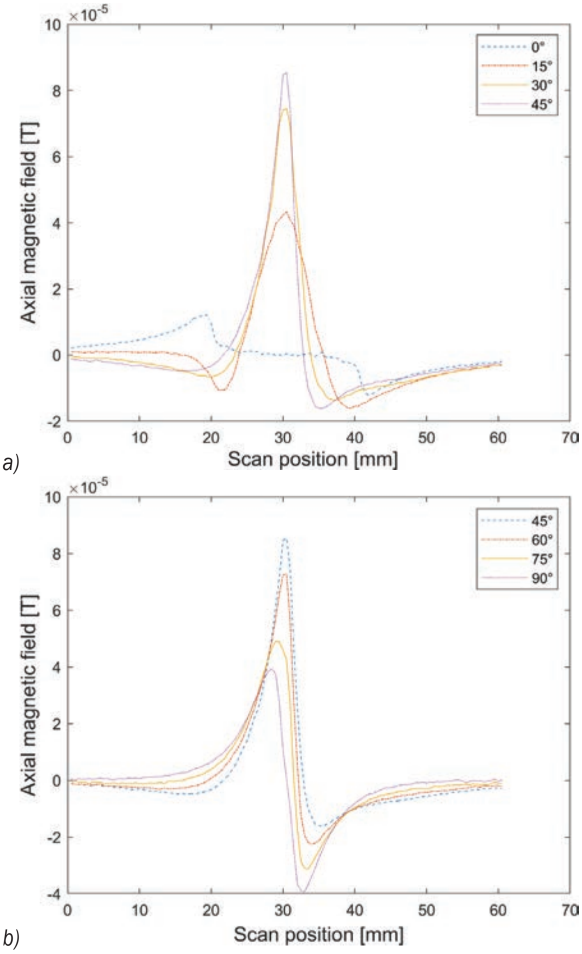

Fig. 11. *Axial magnetic field of defects in different directions; a) 0° to 45°, and b)45° to 90°*

3.4 Effects of Defect Size

The effects of the defect size on the characteristic signal, including the defect's length, width, and depth, are also studied to lay the foundation for the quantification method of defects in the future.

It can be seen from Fig. 12a that with the length of the defect varies from 10 mm to 50 mm, and the distance between the peak and trough of the axial magnetic field curve also changes. The Lissajous patterns are then drawn, as shown in Fig. 12b. The sizes of the Lissajous patterns are also related to the length of each defect.

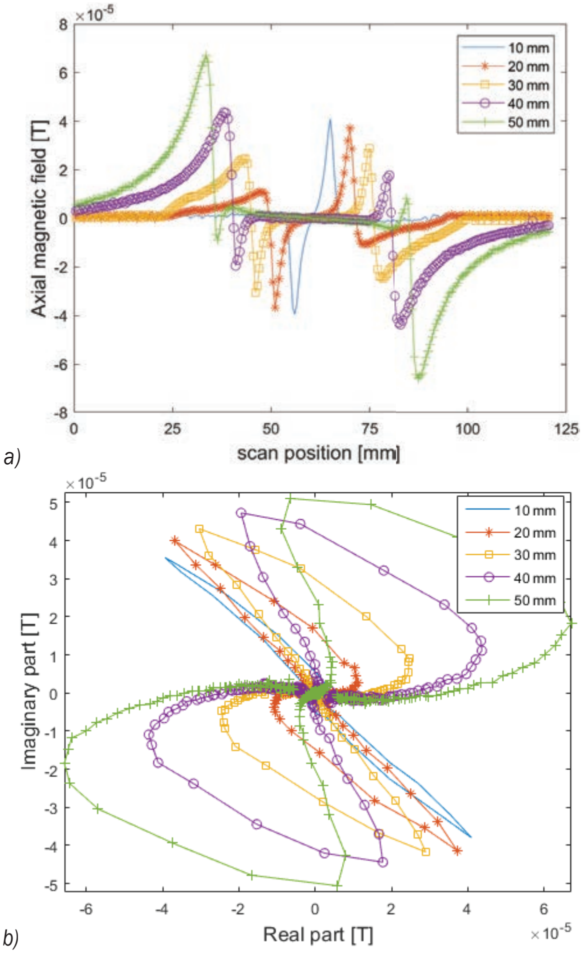

Fig. 12. *a) Axial magnetic field of defects with different lengths, and b) the Lissajous patterns in the impedance plane*

The effects of defect widths were also studied. The width of the defect varies from 1 mm to 4 mm, and the axial magnetic field is also extracted, as shown in Fig. 13a. It can be seen from the figure that the peak and trough of the axial magnetic field curve increase with the increase of the width of the defect.

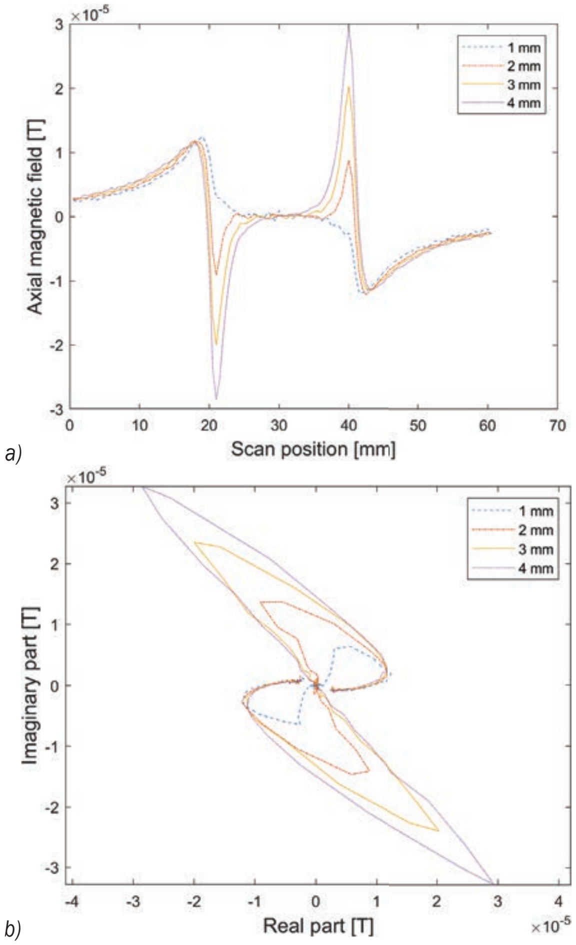

Fig. 13. *a) Axial magnetic field of defects with different widths and b) The Lissajous patterns in the impedance plane*

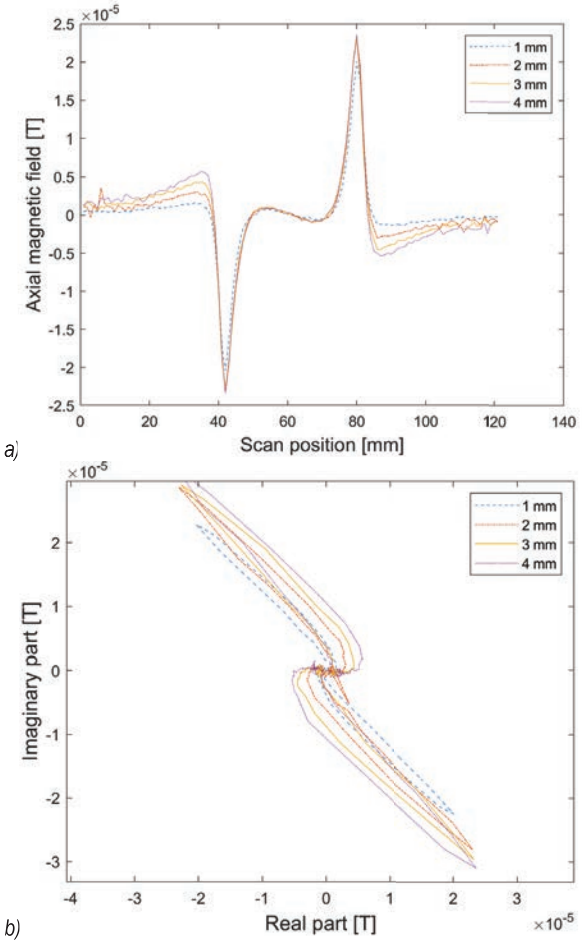

Fig. 14. *a) Axial magnetic field of defects with different depths, and b) the Lissajous patterns in the impedance plane*

Fig. 13b shows the Lissajous patterns of defects with different widths. The sizes of the Lissajous patterns also increase with defect width.

Finally, the effects of defect depth on the characteristic signal is studied. Fig. 14a shows the axial magnetic field of defects with different depths. The depth of the defects varies from 1 mm to 4 mm. The peak value of the axial magnetic field curve is basically unchanged, leading to a less significant change in the Lissajous patterns in Fig. 14b compared to the previous two cases.

4 EXPERIMENTS

An encircling RoFEC system is built to verify the feasibility of the proposed method. The hardware part of the system mainly includes a signal generator, voltage amplifier, lock-in amplifier, the encircling RoFEC probe, data acquisition card and personal computer. It can run independently and complete specific functions. The software part was developed in LabVIEW, including a human-computer interface, data acquisition module, and data processing module. The overall block diagram of the detection system is shown in Fig. 15.

The encircling RoFEC probe is comprised of six excitation windings (shown in Fig. 16a) with the same specifications as the ones used in the FE model and a 50-turn bobbin coil (52 mm in diameter) placed in the centre of the excitation windings around the pipe (shown in Fig. 16b).

Such a bobbin pickup coil in the plane of the rotating field is only sensitive to variations in the axial component of the magnetic field. The coil is self-nulling since when integrated over one circle, the voltage induced in the bobbin coil will be zero at a defect-free position. In addition, as demonstrated in experiments, the phase of the induced voltage in

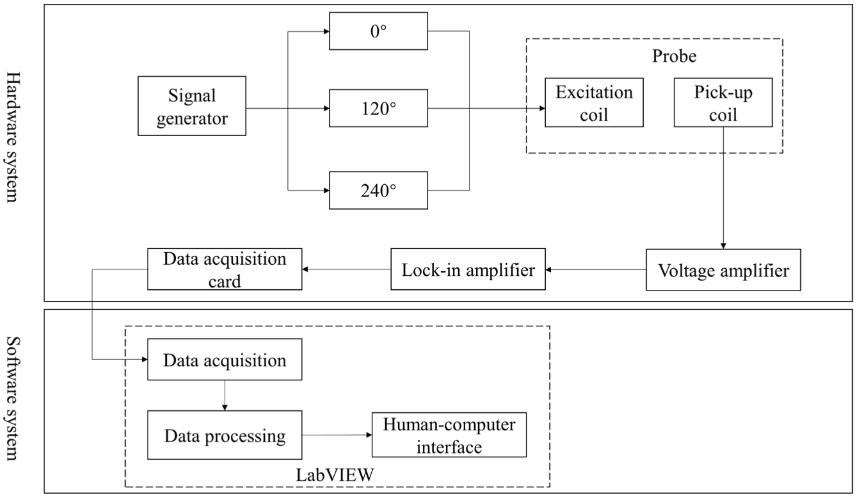

Fig. 15. *Block diagram of the encircling RoFEC system*

the pickup coil is correlated with the circumferential location of the defect in the pipe. Also, under this measurement scheme, the diameter of the bobbin pickup coil is preferably large, so the bobbin pick-coil for the encircling RoFEC probe can have a much bigger diameter than the pipe, leading to a bigger tolerable lift-off distance.

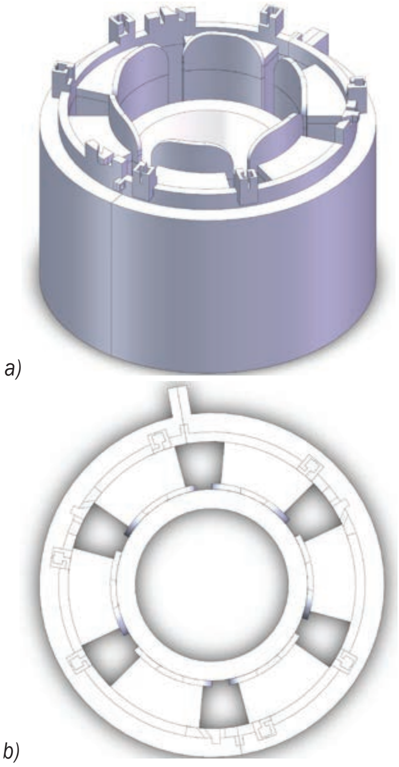

Fig. 16. *Schematic diagram of the encircling RoFEC probe; a) the excitation windings and b) top view of the probe with the bobbin pickup coil in the centre*

The signal generator provided the three-phase sinusoidal excitation (10 kHz, 20 V pk-pk) to generate the rotating electromagnetic field. The voltage amplifier, lock-in amplifier, and data acquisition card were used to process and record the characteristic signal due to defect. The characteristic signal was collected in the computer for further processing and display. In order to realize the axial scanning of the tested pipe, a pipe-scanning platform was also designed. The platform is composed of three sliders, two height adjustment devices, and a slide rail. Two sliders are located at the two ends of the slide rail and are used to fix the two ends of the pipe. The middle slider is used to control the movement of the probe to implement the circumferential scan. The height adjustment device is fixed on the slide rails at both ends for adjusting the height of the pipe. Fig. 17 is the photo of the whole RoFEC system.

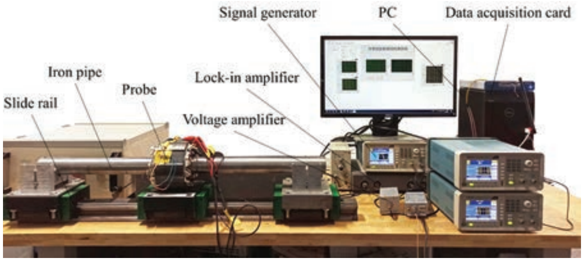

Fig. 17. *RoFEC system*

A steel pipe with a 50 mm outer diameter and 40 mm inner diameter was used as a specimen. Two artificial slots (25 mm × 1 mm × 3 mm) were machined on the outer wall of the pipe, as shown in Fig. 18.

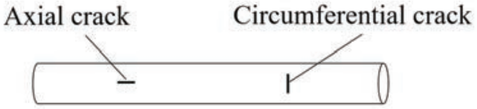

Fig. 18. *Schematic diagram of specimen*

Firstly, the axial defect in the pipe was scanned by the encircling RoFEC system, and the results are shown in Fig. 19. Fig. 19a is the real part of the voltage across the pickup coil, and Fig. 19b is the imaginary part. At the defect-free position, i.e., the starting point of the voltage curve, the measured voltage is basically stable at a near-zero value. When the annular eddy current encounters a crack-like defect, it bypasses each end of the defect in opposite directions, so the measured voltage will have one crest and one trough; this is consistent with the results obtained in the FE model.

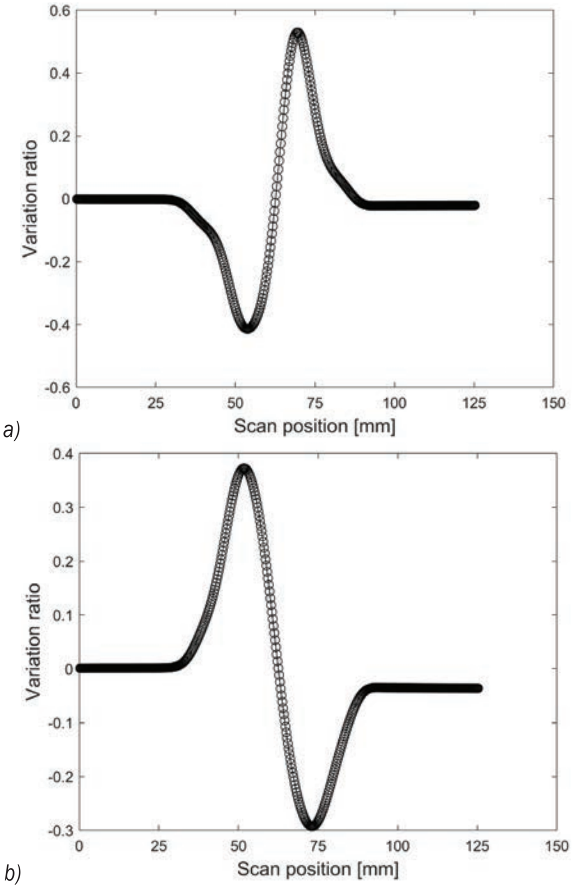

Fig. 19. *Measured voltage for the axial defect; a) real part, b) imaginary part*

The real and imaginary parts of the voltage are then plotted in an impedance plane, as shown in Fig. 20. The plot in the impedance plane integrates the real and imaginary parts and is seen as a Lissajous pattern.

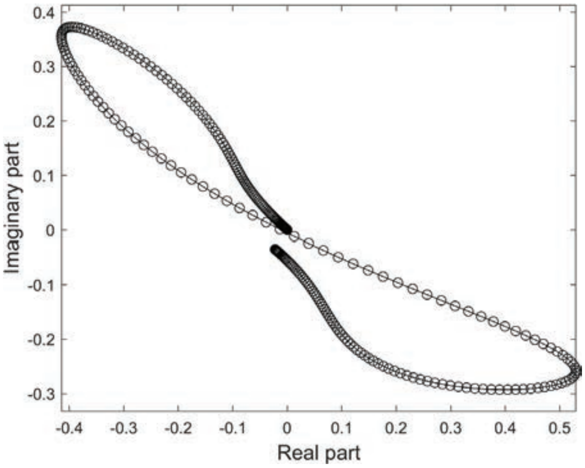

Fig. 20. *Impedance plane plot for the axial defect*

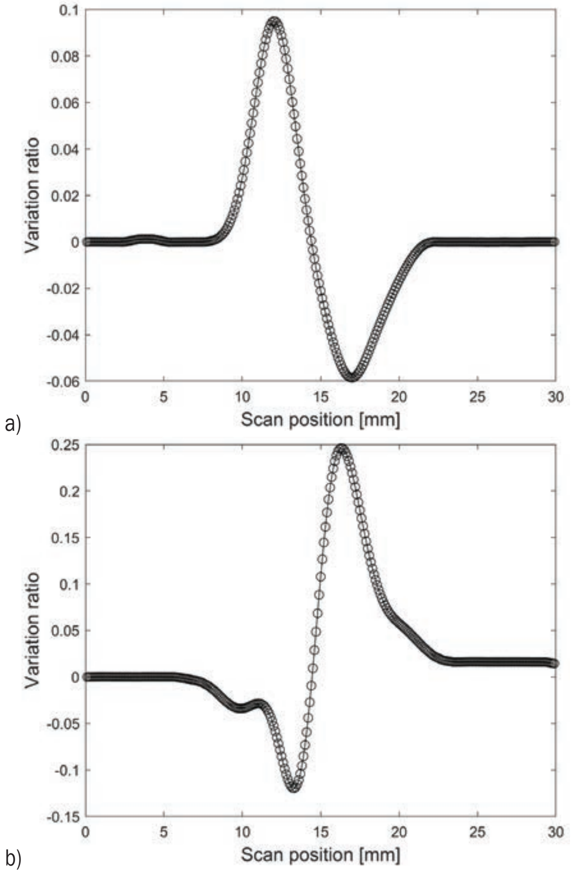

Fig. 21. *Measured voltage for the circumferential defect; a) real part, and b) imaginary part*

The RoFEC system was then used to detect the circumferential defect, and the results are shown in Fig. 21. Fig. 21a is the real part of the voltage across the pickup coil, and Fig. 21b is the imaginary part.

Comparing Figs. 19 and 21, it can be seen that, as indicated by the FE simulation results (Fig. 11), the variation range of the measured voltage is bigger for a circumferential defect.

The real and imaginary parts of the voltage are then plotted in an impedance plane, as shown in Fig. 22. The plot in the impedance is also seen as a Lissajous pattern. The above test results are consistent with the results of the FE model and proved that the RoFEC technique can detect defects in any direction.

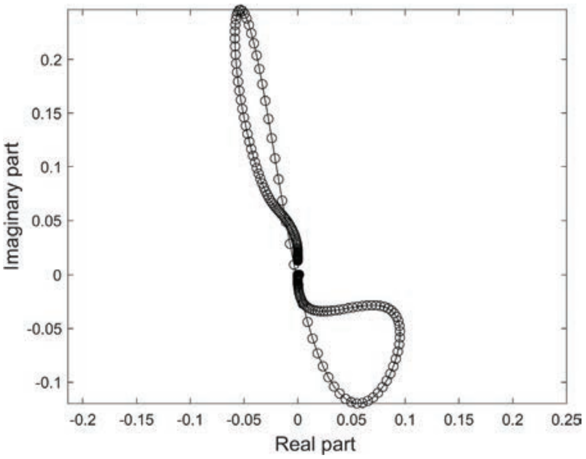

Fig. 22. *Impedance plane plot for the circumferential defect*

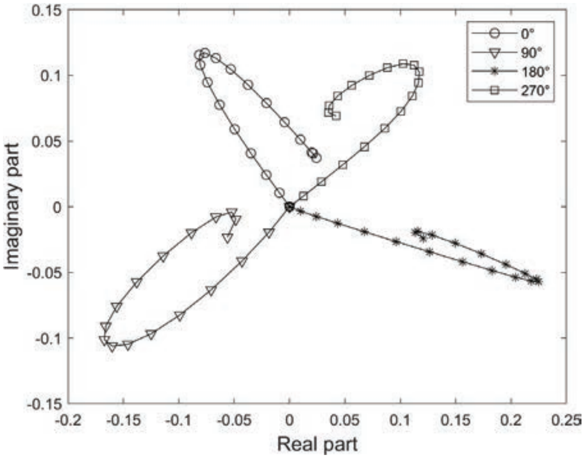

Fig. 23. *Impedance plane plots with the defect at different circumferential locations*

The ability to determine the defect's circumferential location was also verified using the axial defect. In the designed experiments, the pipe was rotated by different angles, and line scans with the axial crack being at 0 degrees, 90 degrees, 180, and 270 degrees with respect to the reference point were performed. The resultant impedance plane plots are shown in Fig. 23. It can be seen that when the circumferential location of the defect on the outer wall of the pipe is different, the angle of the Lissajous pattern changes accordingly. This is also consistent with the FE result, which verified that the encircling RoFEC technique can accurately determine the circumferential location of the defect.

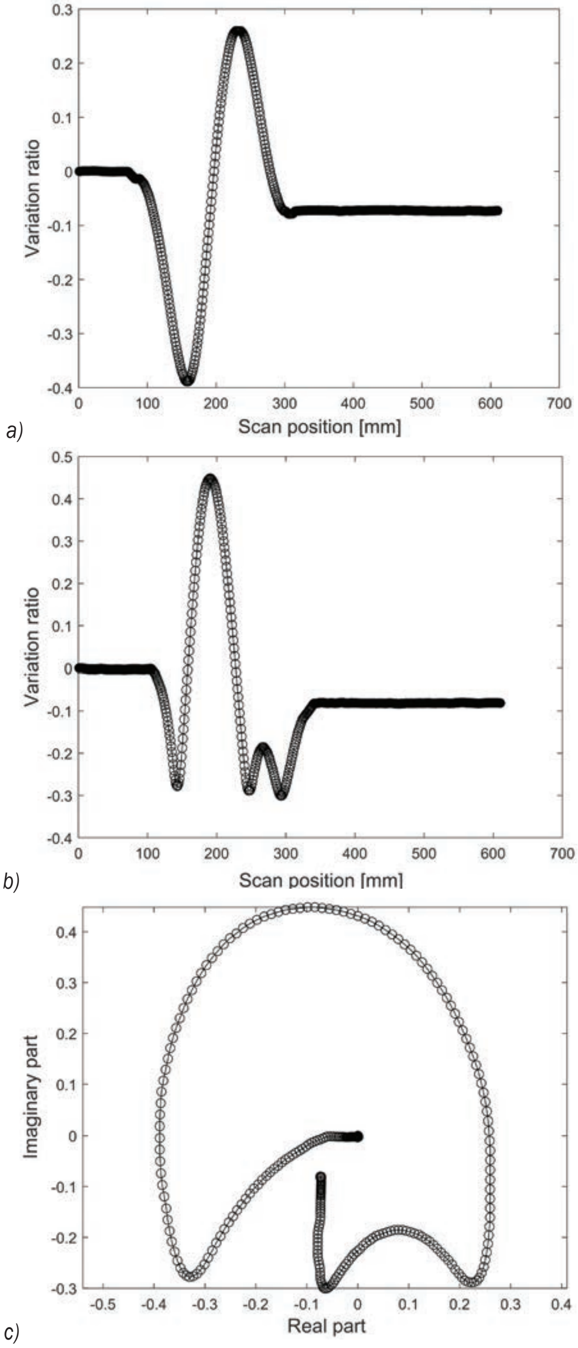

Fig. 24. *Experimental results for the circumferential defect a) Real part of measured voltage b) Imaginary part of measured voltage, and c) Impedance plane plot*

Another experiment on a specimen with a smaller crack was also conducted to test the inspection ability for smaller defects. The specimen is a steel pipe with a 50 mm outer diameter and 40 mm inner diameter. One narrower axial slot (20 mm × 0.3 mm × 1.5 mm) compared to the ones shown in Fig. 18 was machined on the outer wall of the pipe. The encircling RoFEC system scanned the axial slot in the pipe, and the results are shown in Fig. 24. Fig. 24a is the real part of the voltage across the pickup coil, Fig. 24b is the imaginary part, and Fig. 24c is the impedance plane plot. Although the small crack was also detected, the indications are less informative than the bigger defect case. In particular, the impedance plot (shown in Fig. 24c) does not form a "proper" Lissajous pattern and cannot be used to locate the circumferential location of the defect. Such an experiment indicates that the current instrument for the encircling RoFEC technique is only at a proof-of-concept stage, and significant improvement is required.

5 CONCLUSIONS

This paper proposed an encircling RoFEC technique to detect outer wall defects on steel pipes. The working principle of the RoFEC technique was introduced, and the effects of pipe tilt, defect circumferential location, defect orientation and defect size on the inspection performance were analysed in detail using the FE method. An encircling RoFEC system was also built to verify the FE results. The test results showed that the RoFEC technique can effectively detect both axial and circumferential defects. In addition, when the circumferential locations of the defect are different, the angle of the Lissajous pattern in the impedance plane can be used to determine the circumferential location accurately.

Compared with the existing approaches for RoFEC testing from inside the tube **[21]** and **[22]**, in which cases the targeted tubes are non-ferrous materials (e.g. Inconel 600), the encircling RoFEC technique described in this paper focused on the inspection of pipes made of carbon steel, a magnetically permeable material that is more difficult for eddy current related techniques. Another major difference between the encircling and feed-through approaches is the single bobbin pickup coil. Although the single bobbin pickup coil is used in both approaches, the preferences of the coil diameter may be different. For the feed-through approach, the bobbin coil is preferably close to the inner wall to eliminate the lift-off effect, while for the encircling approach, the coil diameter is a design concern. A bobbin coil close to the outer wall of the pipe may not be an optimal choice, and a careful design is required.

It should be noted that this paper aims to demonstrate the feasibility of the encircling RoFEC technique; at present, the encircling RoFEC technique remains at a very early stage, and the current instrument needs to be improved significantly to be able to detect and quantify tiny flaws. Probe design and other influential factors, e.g. lift-off distance of the excitation windings, the diameter of bobbin pick up coil, motion-induced eddy current, and permeability variation due to AC magnetic field, are also worth investigating in further studies.

6 ACKNOWLEDGEMENTS

This work was funded by the National Natural Science Foundation of China (No. 52075549), the Major Scientific and Technological Projects of CNPC (ZD2019-183-004), and the Fundamental Research Funds for the Central Universities (19CX02023A).

7 REFERENCES

[1] Zhou, Z., Tan, J., Wan, F., Peng, B. (2019). Improvement and determination of the influencing factors of coiled tubing fatigue life prediction. *Advances in Mechanical Engineering*, vol. 11, no. 9, art. ID 2072157101, **DOI:10.1177/1687814019880131**.

[2] Brockhaus, S., Ginten, M., Klein, S., Teckert, M., Stawicki, O., Oevermann, D., Meyer, S., Storey, D. (2014). In-line inspection (ILI) methods for detecting corrosion in underground pipelines, in *Underground Pipeline Corrosion*, Orazem, M.E. (ed.), Woodhead Publishing, p. 255-285, **DOI:10.1533/9780857099266.2.255**.

[3] Rifai, D., Abdalla, A., Razali, R., Ali, K., Faraj, M. (2017). An eddy current testing platform system for pipe defect inspection based on an optimized eddy current technique probe design. *Sensors*, vol. 17, no. 3, art. ID 579, **DOI:10.3390/s17030579**.

[4] Yuan, X.A., Li, W., Chen, G., Yin, X., Ge, J. (2017). Circumferential current field testing system with TMR sensor array for non-contact detection and estimation of cracks on power plant piping. *Sensors and Actuators A: Physical*, vol. 263, p. 542-553, **DOI:10.1016/j.sna.2017.07.029**.

[5] Takagi, T., Huang, H., Fukutomi, H., Tani, J. (1998). Numerical evaluation of correlation between crack size and eddy current testing signal by a very fast simulator. *IEEE Transactions on Magnetics*, vol. 34, no. 5, p. 2581-2584, **DOI:10.1109/20.717596**.

[6] Kim, H.M., Heo, C.G., Cho, S.H., Park, G.S. (2018). Determination scheme for accurate defect depth in underground pipeline inspection by using magnetic flux leakage sensors. *IEEE Transactions on Magnetics*, vol. 54, no. 11, p. 1-5, **DOI:10.1109/TMAG.2018.2853618**.

[7] Pham, H.Q., Tran, B.V., Doan, D.T., Le, V.S., Pham, Q.N., Kim, K., Kim, C., Terki, F., Tran, Q.H. (2018). Highly sensitive planar hall magnetoresistive sensor for magnetic flux leakage pipeline inspection. *IEEE Transactions on Magnetics*, vol. 54, no. 6, p. 1-5, **DOI:10.1109/TMAG.2018.2816075**.

[8] Liu, T., Pei, C., Cai, R., Li, Y., Chen, Z. (2020). A flexible and noncontact guided-wave transducer based on coils-only EMAT for pipe inspection. *Sensors and Actuators: A. Physical*, vol. 314, art. ID 112213, **DOI:10.1016/j.sna.2020.112213**.

[9] Liu, Z., Li, A., Zhang, Y., Deng, L., Wu, B., He, C. (2020). Development of a directional magnetic-concentrator-type electromagnetic acoustic transducer for ultrasonic guided wave inspection. *Sensors and Actuators A: Physical*, vol. 303, p. 111859, **DOI:10.1016/j.sna.2020.111859**.

[10] Yang, Q., Xie, S., He, K., Chen, Y., Chen, Z., Uchimoto, T., Takagi, T. (2021). A novel circumferential eccentric eddy current probe and its application for defect detection of small-diameter tubes. *Sensors and Actuators A: Physical*, vol. 331, art. ID 113023, **DOI:10.1016/j.sna.2021.113023**.

[11] Zhao, Y., Qi, P., Xie, Z., Bai, P., Chen, H., Xie, S., Liao, S., Chen, Z. (2020). A new array eddy current testing probe for inspection of small-diameter tubes in Tokamak fusion devices. *Fusion Engineering and Design*, vol. 157, art. ID 111627, **DOI:10.1016/j.fusengdes.2020.111627**.

[12] Alpeisov, E.A., Adzhanov, A.U., Sarsembieva, E.K. (2017). Application of a three-phase sinusoidal current to produce a rotating magnetic field. *International Siberian Conference on Control and Communications*, p. 1-3, **DOI:10.1109/SIBCON.2017.7998480**.

[13] Ye, C., Huang, Y., Udpa, L., Udpa, S.S. (2016). Differential sensor measurement with rotating current excitation for evaluating multilayer structures. *IEEE Sensors Journal*, vol. 16, no. 3, p. 782-789, **DOI:10.1109/JSEN.2015.2488289**.

[14] Ye, C., Udpa, L., Udpa, S. (2016). Optimization and validation of rotating current excitation with GMR array sensors for riveted structures inspection. *Sensors*, vol. 16, no. 9, art. ID 1512, **DOI:10.3390/s16091512**.

[15] Yang, G., Dib, G., Udpa, L., Tamburrino, A., Udpa, S.S. (2015). Rotating field EC-GMR sensor for crack detection at fastener site in layered structures. *IEEE Sensors Journal*, vol. 15, no. 1, p. 463-470, **DOI:10.1109/JSEN.2014.2341653**.

[16] Xin, J., Lei, N., Udpa, L., Udpa, S.S. (2011). Non-destructive inspection using rotating magnetic field eddy-current probe. *IEEE Transactions on Magnetics*, vol. 47, no. 5, p. 1070-1073, **DOI:10.1109/TMAG.2011.2108996**.

[17] Ye, C., Huang, Y., Udpa, L., Udpa, S.S. (2016). Novel rotating current probe with GMR array sensors for steam generate tube inspection. *IEEE Sensors Journal*, vol. 16, no. 12, p. 4995-5002, **DOI:10.1109/JSEN.2016.2556221**.

[18] Ye, C., Xin, J., Su, Z., Udpa, L., Udpa, S.S. (2015). Novel transceiver rotating field non-destructive inspection probe. *IEEE Transactions on Magnetics*, vol. 51, no. 7, p. 1-6, **DOI:10.1109/TMAG.2015.2390144**.

[19] Li, Y., Gao, X., Zhang, Y., You, D., Zhang, N., Wang, C., Wang, C. (2020). Detection model of invisible weld defects by magneto-optical imaging at rotating magnetic field directions. *Optics & Laser Technology*, vol. 121, art. ID 105772, **DOI:10.1016/j.optlastec.2019.105772**.

[20] Gao, X., Du, L., Ma, N., Zhou, X., Wang, C., Gao, P.P. (2019). Magneto-optical imaging characteristics of weld defects under alternating and rotating magnetic field excitation. *Optics & Laser Technology*, vol. 112, p. 188-197, **DOI:10.1016/j.optlastec.2018.11.005**.

[21] Xin, J., Lei, N., Udpa, L., Udpa, S.S. (2013). Rotating field eddy current probe with bobbin pickup coil for steam generator tubes inspection. *NDT & E International*, vol. 54, p. 45-55, **DOI:10.1016/j.ndteint.2012.12.002**.

[22] Lei, N., Udpa, L., Udpa, S., Zeng, Z. (2010). Rotating field eddy current (RoFEC)-probe for steam generator inspection. *International Journal of Applied Electromagnetics and Mechanics*, vol. 33, p. 1279-1285, **DOI:10.3233/JAE-2010-1250**.

[23] Grimberg, R., Udpa, L., Savin, A., Steigmann, R., Vizureanu, P., Bruma, A., Udpa, S.S. (2008). Remote field eddy current control using rotating magnetic field transducer: application to pressure tubes examination. *Research in Non-destructive Evaluation*, vol. 19, no. 4, p. 202-218, **DOI:10.1080/09349840802190090**.

[24] Qka, M., Enokizono, M. (2020). A detection of backside crack using rotational magnetic flux sensor with search coils. *IEEE Transactions on Magnetics*, vol. 32, no. 5, p. 4968-4970, **DOI:10.1109/20.539304**.

[25] Koyama, K., Hoshikawa, H., Sakon, T. (2011). Study on metal detection with electromagnetic induction probe utilizing rotating magnetic field. *Electrical Engineering in Japan*, vol. 177, no. 4, p. 1-11, **DOI:10.1002/eej.21178**.

Strojniški vestnik - Journal of Mechanical Engineering 68(2022)1, 39-55
© 2022 The Authors. CC BY 4.0 Int. Licensee: SV-JME
DOI:10.5545/sv-jme.2021.7328
Original Scientific Paper
Received for review: 2021-07-14
Received revised form: 2021-10-01
Accepted for publication: 2021-12-07

Research on a Real-time Reliability Evaluation Method Integrated with Online Fault Diagnosis: Subsea All-electric Christmas Tree System as a Case Study

Peng Liu – Dagang Shen – Jinfeng Cao*
Qingdao University of Technology, School of Mechanical and Automotive Engineering, China

The subsea all-electric Christmas tree is key equipment in subsea production systems. If a failure occurs, the marine environment will be seriously polluted. Therefore, strict reliability analysis and measures to improve reliability must be performed before such equipment is launched, which is crucial to safe subsea production. A real-time reliability evaluation method for the all-electric Christmas tree mechanical system integrated with the static Bayesian network fault diagnosis stage is proposed in this paper, which realizes the identification of the fault type of the components and the real-time reliability evaluation of the mechanical system under different failure rates of the components. As a supplement to the method, by using mutual information to conduct sensitivity analysis on the reliability of the mechanical system, the importance of the basic events of each component on the reliability of the system is finally given. The proposed method provides significant theoretical support for the maintenance of the subsea all-electric Christmas tree and can be extended to the reliability evaluation of general subsea production systems.

Keywords: reliability analysis, Bayesian network, fault diagnosis

Highlights

- *This article contributes a real-time reliability evaluation method integrated with the online fault diagnosis stage by using dynamic Bayesian networks.*
- *The proposed method identifies component fault types and the real-time reliability evaluation of the mechanical system under different component failure rates in a marine environment.*
- *The problem of inaccurate evaluation results caused by only considering component degradation rate or using sensor data as a single piece of evidence has been overcome by using this method.*
- *The proposed method provides important theoretical support for the maintenance of the mechanical system of the all-electric Christmas tree and can be extended to the reliability evaluation of general subsea production systems.*

0 INTRODUCTION

Process safety, risk analysis, and reliability evaluation have paramount significance in the modern process industries for preventing fatalities and loss of assets [1] and [2]. Even certified and tested equipment may experience problems during operation due to incorrect installation, operating environment, operator error, or lack of maintenance [3] and [4]. Furthermore, once installed, the subsea equipment must be transported back to the shore for maintenance and repair, which is time and resource consuming. The best way to avoid such large maintenance costs is to improve the reliability of subsea equipment by performing a reliability evaluation before launching the equipment. Moreover, a reliability evaluation can guide the maintenance of engineering staff.

Subsea all-electric Christmas trees (XTs) are critical pieces of equipment in subsea production systems [5] and [6]. They are the only viable method for oil and gas development that can be utilized in some areas. The ecosystem is fragile, and oil spills can have irreversible effects; therefore, very reliable and safe subsea XT systems are required [7]. Indeed, safe and reliable subsea production systems will become increasingly important. The research on the reliability evaluation method of XT is paid increasing attention by scholars. In general, reliability evaluation methods of subsea XT can be divided into three categories: model-based, signal-based, and data-driven methods [8] to [11]. The model-based methods focus on building mathematical models of complex industrial systems, while the signal-based methods compare the detected signals with prior information obtained from normal industrial systems and use the detected signals to perform real-time online reliability evaluation [12]. However, for complex industrial and process systems, accurate mathematical models and signals are difficult to obtain, and the XT is a typical complex system. Data-driven methods that rely on historical data for reliability evaluation are particularly suitable for complex industrial systems.

Data-driven methods (e.g., Bayesian Network) have been shown to solve problems in complex systems, which has been used for reliability or risk analyses of XT systems or other subsea equipment

---

*Corr. Author's Address: Qingdao University of Technology, Jialingjiang East Road No. 777, Qingdao, China, caojinfeng@qut.edu.cn

[13]. For example, Wang et al. quantitatively analysed the reliability and availability of a subsea tree system with different repair states using the dynamic Bayesian network (DBN). In addition, the influence of failure rates and degradation probability on reliability and availability has been analysed [14]. Li et al. [15] presented a risk-based accident model to conduct quantitative risk analysis (QRA) for leakage failure of submarine pipeline by using a Bayesian network. The model can provide a more case-specific and realistic analysis consequence compared to the bow-tie method, since it could consider the common cause failures and conditional dependency in the accident evolution process of pipeline leakage. Wang et al. presented an advanced two-step approach using Bayesian networks to analyse the failure probabilities of an urban buried gas pipeline. This novel approach could better reveal the relationships among failure causal factors and could also update the failure probabilities as operational and environmental conditions evolve [16]. Cai and Liu et al. [17] proposed a reliability and resilience evaluation method by combining the Markov model with a Bayesian network and used this method to conduct a risk analysis and reliability evaluation of the subsea oil and gas pipelines. Li et al. [18] proposed a method of quantitative assessment of the risk of gas explosion in an underground coal mine using a Bayesian network. This method overcomes the shortcomings of traditional methods in quantitative evaluation, dynamic control, and dealing with uncertainty. Lyu et al. proposed a Bayesian network model for series, parallel, and voting systems by considering common cause failure (CCF) and coverage factors. The model was used to evaluate the reliability of the subsea XT control system at any time, and the difference between posterior probability and prior probability of each component in the event of system failure was obtained. The effects of CCF and single-component failure rate on system reliability were studied [19]. Zhang et al. [20] used Bayesian networks to quantitatively evaluate the reliability of subsea production systems, including the subsea XT, in the early design stages.

Recently, there has been a growing interest in data-driven and model-based methods to understand and integrate both approaches in order to provide better diagnostic systems and reliability evaluation [21]. For example, Qian et al. [22] proposed a method of integrated extreme learning machine algorithm (data-driven algorithm) and model-based (fault model) for condition monitoring of the wind turbine gearbox. Zou et al. [23] proposed a novel data-driven stochastic manufacturing system model to describe production dynamics, and a systematic method has been developed to identify the causes of permanent production loss in both deterministic and stochastic scenarios. The proposed methods integrate available sensor data with the knowledge of production system physical properties. Simani et al. [24] studied the fault diagnosis and continuous control of wind turbines based on data-driven and model-based robust strategies. Wang et al. [25] discussed feasible integration approaches for the model-driven and data-driven methods based on the existing achievements and proposed integrating both methods for the power system online frequency stability and reliability assessment.

The above-mentioned research has found that the Bayesian method is widely used to evaluate the safety, risk, and reliability of complex system and XTs. It is worth noting that the focus of these studies is to explore the impact of some traditional factors on system reliability, especially for real-time and static evaluation of system reliability. The basic research of these methods has greatly inspired our work; to the best of our knowledge, during the working process of XT, some local faults often occur, some are intermittent, and some are permanent. These faults usually have an important impact on the real-time reliability of XT. Therefore, the real-time reliability evaluation data of the system are different under different fault rate states of the components. To study the influence of the important factor of "fault" on system reliability, a real-time reliability evaluation method integrated with online diagnosis is proposed by using Bayesian networks, and the subsea all-electric XT mechanical system is used as a case study to verify the practicability of the method. Generally, methods of obtaining data include simulation, experimental testing, data reasoning, and expert data. In this paper, an XT testing system [10] is used to collect normal working signals and fault signals of the system. The abnormal signals of the pressure sensors are used to indicate the fault signals to obtain the components' fault information. According to the Weibull distribution law, the reliability change trend of the normal degradation process of the component is obtained. These data ultimately provide probability information for the Bayesian network.

The rest of the paper is organized as follows. Section 1 introduces the basic principles of Bayesian networks. Section 2 proposes the real-time reliability evaluation method integrated with online diagnosis. Section 3 provides a case study of subsea all-electric XT mechanical systems to demonstrate the application of the proposed approach. Section 4 summarizes the work.

1 BASIC THEORY BRIEF DESCRIPTION O F BAYESIAN NETWORK

A Bayesian network is a data-driven reasoning method, which is widely used in the reliability evaluation and fault diagnosis analysis of complex systems. It is a graphical network that uses probabilistic reasoning and includes two parts: a qualitative part and a quantitative part. The qualitative part is represented by a directed acyclic graph, including system variable nodes and directed arcs indicating the causal relationships between the nodes. The quantitative part is the conditional probability tables between child and parent nodes.

According to the conditional independence and the chain rule, $P(U)$ represents the joint probability distribution of the variables $U=\{A_1, A_2, ..., A_N\}$, which can be represented as:

$$P(U)=\prod_{i=1}^{N} P(A_i \mid Pa(A_i)), \tag{1}$$

where $Pa(A_i)$ is the parent node of A_i.

If there is new evidence E, then the posterior probability of the variable can be calculated by the Bayesian formula, as follows:

$$P(U \mid E)=\frac{P(E \mid U)P(U)}{P(E)}=\frac{P(E,U)}{\sum_U P(E,U)}. \tag{2}$$

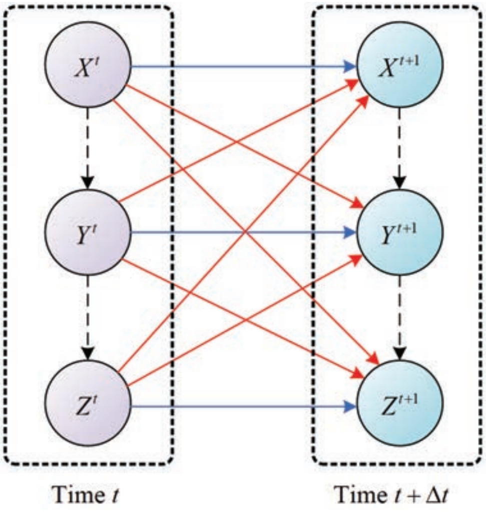

Fig. 1. *Structure of dynamic Bayesian network*

A dynamic Bayesian network is the combination of a static Bayesian network and time information to form a new random model with the processing of time series data. Each time step in the model is called a time slice. The basic structure of a dynamic Bayesian network is shown in Fig. 1. Where t is the current time slice, $t+1$ represents the next time slice, Δt is the interval of time slices, and dotted directed arcs show the relationship between variables in the same time slice, while solid line directed arcs represent that in different time slices. Similar to the static Bayesian network calculation method, the joint probability distribution of the dynamic Bayesian network can be calculated as follows:

$$P(A_{1:T})=\prod_{t=1}^{T}\prod_{i=1}^{N} P(A_t^i \mid Pa(A_t^i)). \tag{3}$$

2 RESEARCH ON REAL-TIME RELIABILITY EVALUATION METHOD OF ALL-ELECTRIC CHRISTMAS TREE

2.1 Theoretical Model of Bayesian Network Reliability Evaluation for All-electric Christmas Tree

The theoretical model of the real-time reliability evaluation of the all-electric Christmas tree consists of two main phases: the fault diagnosis stage based on a static Bayesian network and the real-time reliability evaluation stage based on a dynamic Bayesian network, as shown in Fig. 2. In Fig. 1, both blue and red directed solid arcs indicate the causal relationship between nodes in different time slices. The blue arcs represent the degradation trend of the same component, and the red arcs represent the influence relationship between different components in different time slices. Since this study did not consider the influence and dependency relationships between different components, there are no directed arcs between different components in Fig. 2.

The static Bayesian network fault diagnosis phase consists of three layers: the additional information layer, the fault layer, and the fault symptom layer. $A_1, A_2, \ldots, A_n$ are parent nodes in the additional information layer and also called additional information nodes, which represent the influence of subsea environment and operator experience on the probability of failure of all-electric XT mechanical components, such as corrosion degree, well fluid temperature, operating depth, repair frequency and so on. Child nodes $F_1, F_2, \ldots, F_n$ are located at the fault layer, called fault nodes, which represents the probability of failure of relevant components of the all-electric Christmas tree, such as the probability of valve clogging failure and leakage failure, etc., and

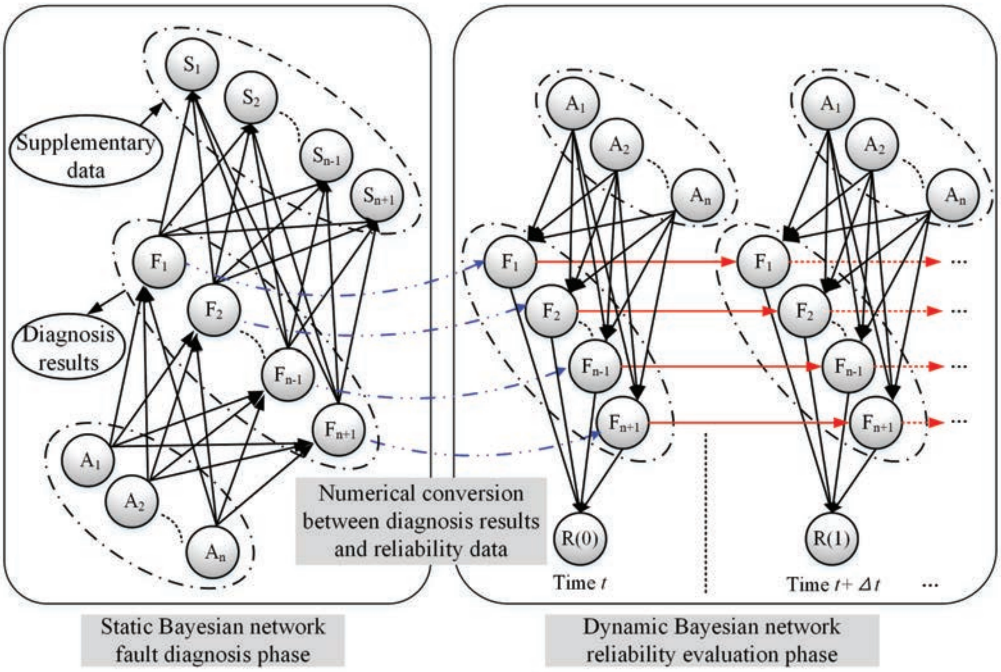

Fig. 2. *Theoretical model of real-time reliability evaluation*

each faulty node has a corresponding fault type. Child nodes $S_1, S_2, \ldots, S_n$ are located in the fault symptom layer, which are called the fault symptom nodes, and mainly from the data acquired by the sensor, such as the change of pressure value of pressure sensor is the most direct characterization of component failure. The supplementary data are the real data of the sensor when the fault occurs, and these data are re-entered into the fault symptom layer to improve fault diagnosis accuracy; the probability of failure of a certain component can be deduced reversely through the static Bayesian network eventually.

The dynamic Bayesian network reliability evaluation phase is composed of multiple time slices, and each time slice includes three layers: the additional information layer, the reliability component layer, and the reliability result layer. The additional information layer is the same as the static Bayesian fault diagnosis stage, and the above additional information not only affects the failure probability of the component but also affects the reliability probability of the component. During the evaluation phase, Child nodes $F_1, F_2, \ldots, F_n$ are located in the reliability component layer, which are the deformation of the fault nodes in the fault diagnosis stage, and for each node, the value is the complement of the fault diagnosis result in $[0, 1]$. The child node $R(x)$ is located in the reliability result layer, and the reliability data in the current time slice of the component is obtained. In each time slice, the reliability results are obtained based on the forward derivation of the Bayesian network. Multiple time slices constitute a dynamic Bayesian network evaluation model, and the arcs between the time slices connect the layers of reliability components located in different time slices and represent the trend of inter-chip transfer, indicating component reliability. The time interval between adjacent time slices is denoted by Δt, which can be 1 hour, 1 day, 1 month, etc.

Based on the theoretical model of real-time reliability evaluation, recording the sensor data at a specific moment, then bringing into the fault diagnosis stage of static Bayesian network, and the real-time component fault diagnosis results can be obtained by reverse derivation. The result is numerically transformed and input into the time slice t of the dynamic Bayesian network reliability evaluation stage, and the influence of additional information is considered. The forward derivation of the Bayesian network in different time intervals is carried out to obtain the component reliability probability in corresponding time slice, and finally the relationship between time and component reliability is obtained.

Previously, the author's scientific research team and CNOOC Energy Development Co., Ltd. Shenzhen Oilfield Construction Branch jointly developed the XT test system to perform fault detection on the Christmas tree, as shown in Fig. 3 **[26]**. The test system is connected to the Christmas tree through hydraulic lines and communication cables to complete valve operating condition detection, production loop detection, annulus loop detection, chemical injection loop detection, and acquires sensor data in real time, as shown in Fig. 4.

In the conditional probability table, the increase in the number of parameters will lead to an exponential increase in the amount of calculation; therefore, the Noisy-OR and Noisy-MAX models are used to determine the conditional probability table. The conditional probability table can be calculated simply and quickly by using Noisy-OR when a node has two states. For the Noisy-OR model, *Y* is considered to be the result of different causal variables, such as $X_1, X_2, ..., X_n$, and these causal variables are considered to be Boolean values: only "true" and "false" status. A conditional probability table including n parameters (e.g., q_1, q_2, …, q_n) can be determined with the Noisy-OR model. The formula for calculating the conditional probability of a parent node being 1 is as follows **[27]** and **[28]**:

$$P\left(Y=1 \mid X_1, X_2, ..., X_n\right)=1-\prod_{i=1}^{n} q_i, \tag{4}$$

Q here q_i is the probability that *Y* is false when X_i is assumed to be true, and all other parent nodes are false.

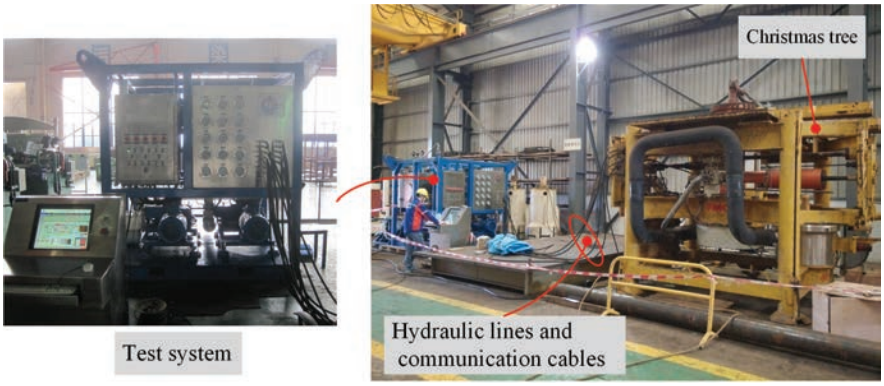

Fig. 3. *Subsea Christmas tree testing system*

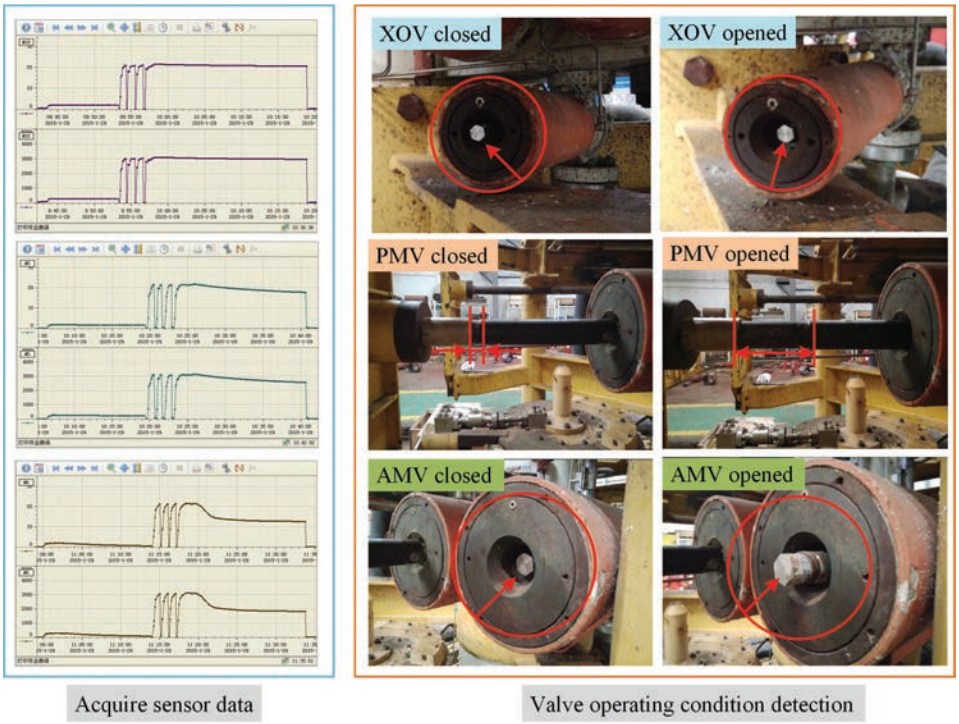

Fig. 4. *Sensor data acquisition*

If there are more than two states in a node, for example, the sensor data includes "high", "low", and "normal" states, which represent high pressure, low pressure, and normal pressure, respectively. It can be calculated simply with the Noisy-MAX model in the conditional probability table. Similarly, Y is considered to be the result of different causal variables; these cause variables such as $x_1, x_2, \ldots, x_n$, but these causal variables are not Booleans. The calculation formula of the conditional probability table is as follows [28]:

$$P\left(Y \leq y \mid X\right)=\prod_{\substack{i=1 \\ x_i \neq 0}}^{n} \sum_{y'=0}^{y} q_{i,y}^{x_i}, \tag{5}$$

$$P\left(Y = y \mid X\right)= \begin{cases} P\left(Y \leq 0 \mid X\right) & if\ y=0 \\ P\left(Y \leq \mathrm{y} \mid \mathrm{X}\right)-P\left(Y \leq \mathrm{y}-1 \mid \mathrm{X}\right) & if\ y>0 \end{cases}, \tag{6}$$

where $X=x_1, x_2, \ldots, x_n$, and y is specific condition boundary.

2.2 Fault Diagnosis Stage Based on Static Bayesian Network

The cumulative number of various fault symptoms at different intervals such as 1,000 hours or 2,000 hours can be recorded by using the XT test system; the symptom data corresponding to these faults are then input into the fault symptom layer. Fault diagnosis is carried out by reverse derivation of static Bayesian network; the diagnosis result of the fault diagnosis method does not clearly indicate that the fault must occur, but it provides the failure probability of the component to guide the maintenance [28]. Generally, the greater the probability of failure, the greater the likelihood of failure of the corresponding component. However, there is a kind of failure. When the failure occurs, it will not cause huge economic losses or casualties but will only cause < temporary reduction in production or the XT cannot work normally. In this paper, the type of failure is defined as safety failure of the mechanical component (hereinafter: safety failure). For example, when the control signals of the surface control subsea safety valve (SCSSV), production main valve (PMV), and production wing valve (PWV) are lost, the valve cannot be closed. However, such failures can usually be resolved by restarting the subsea control module (SCM) without causing great economic losses. The priority of fault maintenance can be determined by taking different measures to deal with safety failure. Combined with the experience of engineers, three judgment rules are defined to determine the diagnosis result, and some engineers applied similar judgment rules to the fault diagnosis of deep-water blowout preventer (BOP) systems [10].

Rule 1: If the type of failure is not a safety failure, when the difference between the posterior probability and the prior probability of the failed node is ≥ 60 %, the failure will be reported.

Rule 2: If the type of failure is not a safety failure, a warning will be issued when the difference between the posterior probability and the prior probability of the fault node is ≥ 30 % and ≤ 60 %.

Rule 3: If the failure type is a safety failure, then when the difference between the posterior probability and the prior probability of the fault node is ≥ 80%, an early warning will be issued.

For the convenience of analysis, the mechanical system of the all-electric XT is symbolized, as shown in Fig. 5. Its working principle is described as follows: under normal operating conditions, SCSSV continuously transports crude oil from the wellhead to the oil storage device through the production loop, and PMV, PWV, PCV (production control valve) and PIV (production isolation valve) all remain open in this case; once a problem occurs in the production loop, the signals of the corresponding sensors (such as PS11, PS12 and FS11) will change, and the signal of the sensor is used to determine whether crossover valve (XOV) needs to be turned on. If XOV is opened, the annulus loop is connected, and AMV is put into operation. At the same time, the valve of the chemical injection loop is always kept open, and the chemical is injected into the production loop.

Using Netica software [29] for Bayesian network modelling and analysis, the nodes of the additional information layer are determined as the parent nodes of the fault nodes, and each parent node has two states (i.e., a high state and a low state), indicating the degree of reasoning of the corresponding additional information. Under the influence of additional information nodes, fault diagnosis is made for the components of the system. The failure layer includes 12 nodes, which represent the failure probability of 12 components (surface control subsea safety valve (SCSSV), PMV, PWV, chemical injection valve 2 (CIV2), XOV, annular main valve (AMV), PCV, PIV, chemical injection valve 2 (CIV1), AMV (annular main valve), AAV (annulus access valve), and MIV (methanol injection valve)).

To make the analysis convenient, the components are divided into five categories according to the structure, function, and parameters of the main components of the all-electric XT. The relationship

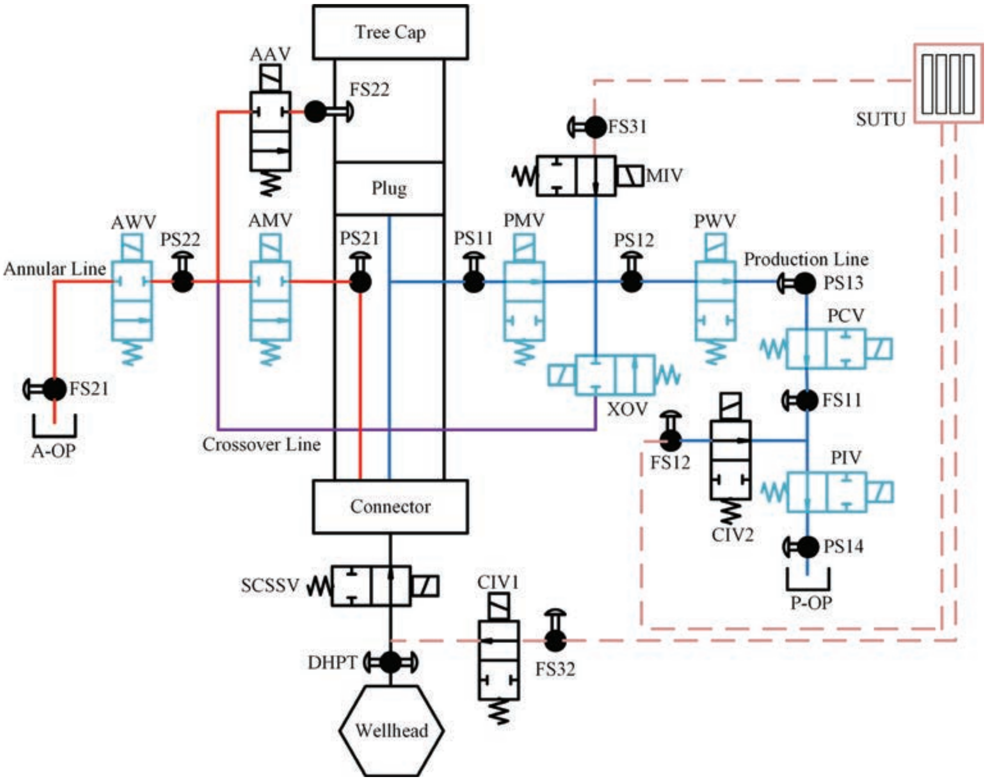

Fig. 5. *Symbolic representation of subsea all-electric XT machine system*

and classification between the additional information node and the fault node are shown in Table 1. For example, "SCSSV_Failure" indicates the SCSSV fault node, "Present" indicates the probability of failure of the corresponding component of the node, and "Absent" indicates the probability of no failure.

The conditional probability tables of the additional information nodes and the fault nodes can be calculated by using the Noisy-OR model of Eq. (4) and establishing a Bayesian network of the relationship between the additional information layer and the fault layer, as shown in Fig. 6. In the initial state, the high and low state probabilities of all additional information nodes are set to 99 % and 1 %, respectively, and the "Absent" state probability and "Present" state probability of the fault node can be derived.

In the XT mechanical system, SCSSV, PMV, PWV, AMV and XOV are the most critical components; therefore, it is very important to guide the repair and maintenance of the XT by focusing on distinguishing the types of faults during the fault

Table 1. *The relationship and classification between additional information node and the fault node*

Fault nodes	State	Additional information (high)			
		Corrosion degree	Well fluid temperature	Operating depth	Repair frequency
SCSSV_Failure	Absent	0.988	0.985	0.986	0.987
	Present	0.012	0.015	0.014	0.013
PMV/PWV /PIV_Failure	Absent	0.988	0.985	0.986	0.987
	Present	0.012	0.015	0.014	0.013
AMV/annular wing valve(AWV)/ AAV/XOV_Failure	Absent	0.988	0.985	0.986	0.987
	Present	0.012	0.015	0.014	0.013
CIV1/CIV2 /MIV_Failure	Absent	0.988	0.985	0.986	0.987
	Present	0.012	0.015	0.014	0.013
PCV_Failure	Absent	0.988	0.985	0.986	0.987
	Present	0.012	0.015	0.014	0.013

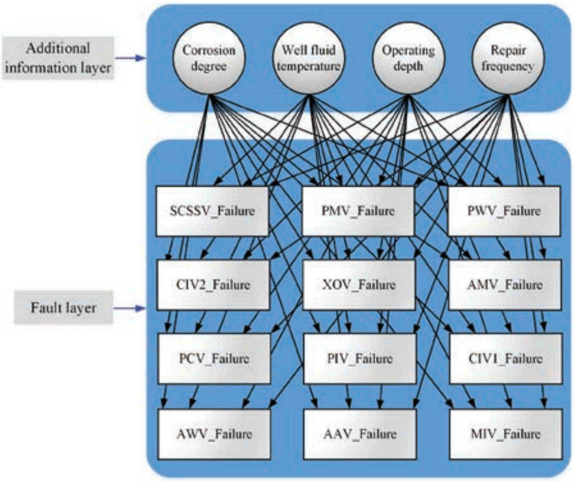

Fig. 6. *Bayesian network of additional information and fault layer*

diagnosis stage. For example, when the Christmas tree is working normally, the valves on the production loop are all open, XOV remains closed, if the control signals of SCSSV, PMV and PWV are lost, the valve cannot be closed; however, this fault can usually be solved by restarting the SCM, which means that only a safety failure has occurred and will not cause much loss; there is no need to salvage the XT from the water to the shore foundation for maintenance. Therefore, the failures of the above five key components are specifically divided into three failure types, namely blocking, leakage and safety-failure (SFailure).

In the fault layer of the Bayesian network, the nodes of the above five key components are replaced, and each replaced node includes four states: Normal, Blocking, Leakage, and SFailure, as shown in Fig. 7 (Netica software figure). Based on the reverse derivation of the static Bayesian network fault diagnosis stage, the fault types of the five key components can be discriminated, according to the judgment rules to report the corresponding message. The relationship between the replaced and replaced nodes is shown in [10].

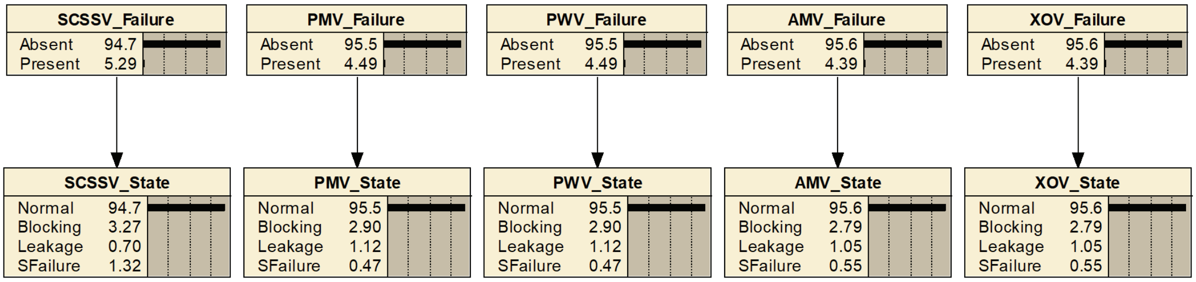

Fig. 7. *Fault nodes replacement*

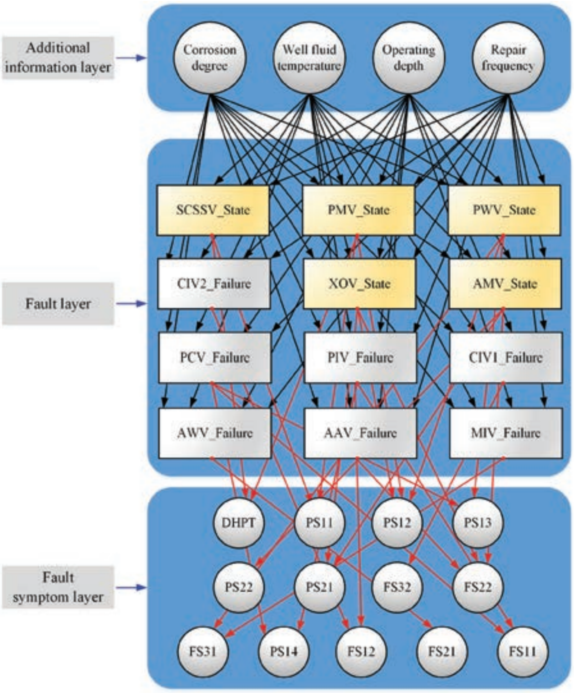

Fig. 8. *Static Bayesian network fault diagnosis phase model of subsea all-electric XT*

The fault diagnosis model of the all-electric XT established based on the static Bayesian network is shown in Fig. 8, the fault symptom layer includes 13 nodes (DHPT, PS11, PS12, PS13, PS14, PS21, PS22, FS11, FS12, FS21, FS22, FS31, FS32), representing the corresponding sensor data, and each node has three states, namely “normal”, “high” and “low”. The sensor value below 10 % of the normal value is in a “low” state, while 10 % above the normal value is in a “high” state. Because each fault symptom node has three states, the Nosiy-MAX model can be used to calculate the conditional probability tables of the fault node and the fault symptom node, as shown in Eqs. (5) and (6). Due to system uncertainties in the static Bayesian network fault diagnosis model, such as the detection accuracy and measurement error of the sensor, the "Absent" state of all fault nodes is set to 99 % instead of 100 % in the initial state [30].

2.3 Reliability Evaluation Stage Based on Dynamic Bayesian Network

The real-time reliability evaluation of the dynamic Bayesian network is carried out on the basis of the fault diagnosis of the static Bayesian network, and the evaluation model is still modelled using Netica software. The model of the dynamic Bayesian network evaluation stage is shown in Fig. 9. Each time slice Time *t* is expanded to four layers: additional information layer, component reliability layer, loop reliability layer and Christmas tree reliability layer. The additional information layer consists of four nodes and is consistent with the fault diagnosis stage of a static Bayesian network. The component reliability layer is the deformation of the fault node in the fault diagnosis stage and includes 12 nodes. The loop reliability layer includes three nodes: PL_R, AL_R and CL_R. The XT reliability layer has only one XT reliability node XT_R.

In the stage of reliability evaluation based on dynamic Bayesian networks, the state of the node "Re" indicates the reliability probability of the component, "Fa" means the failure rate of the component, and in the initial state, set the "Re" of all component reliability nodes to 100 %. All-electric Christmas tree components comply with the life

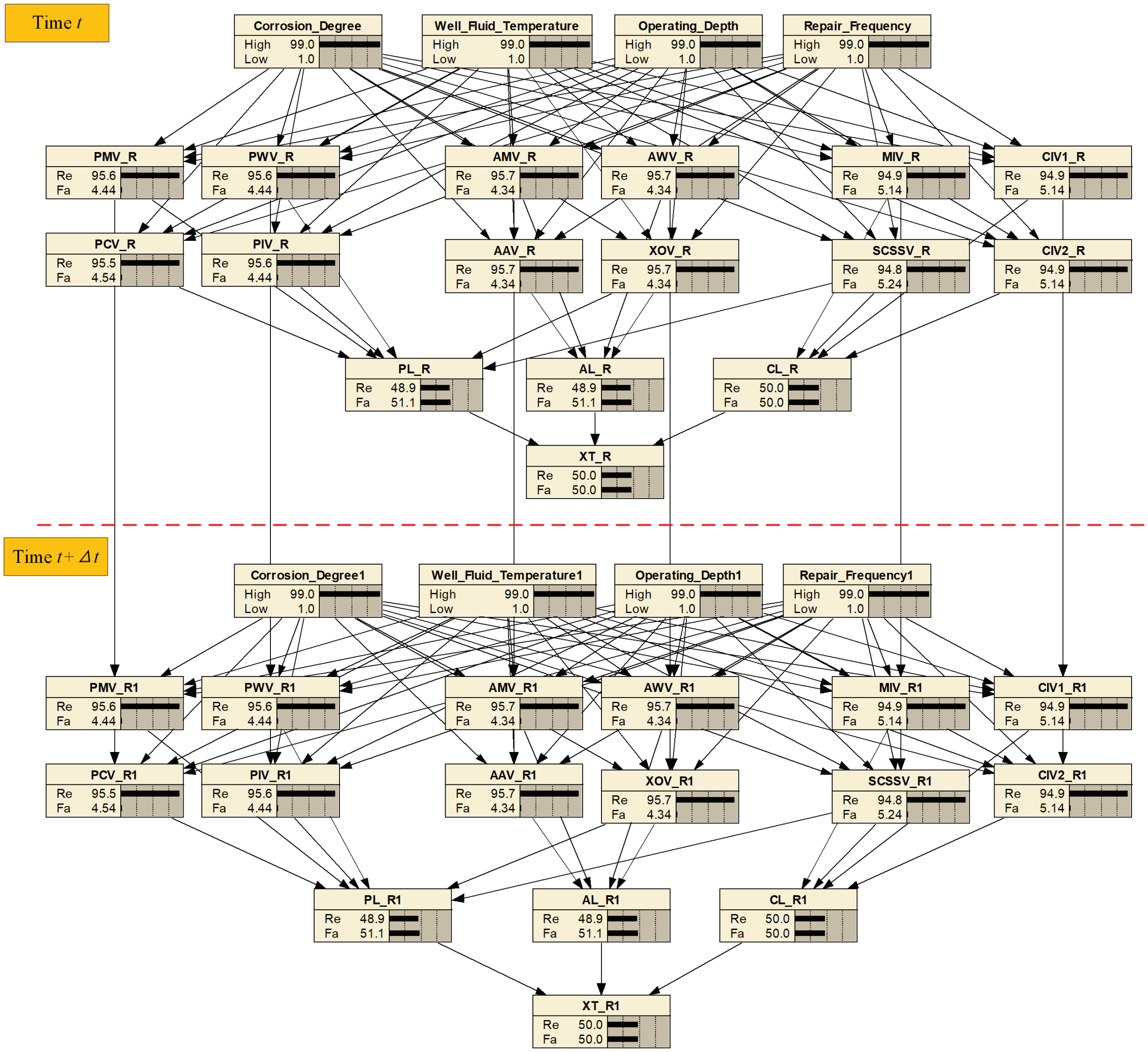

Fig. 9. *Dynamic Bayesian network reliability evaluation phase model of subsea all-electric XT*

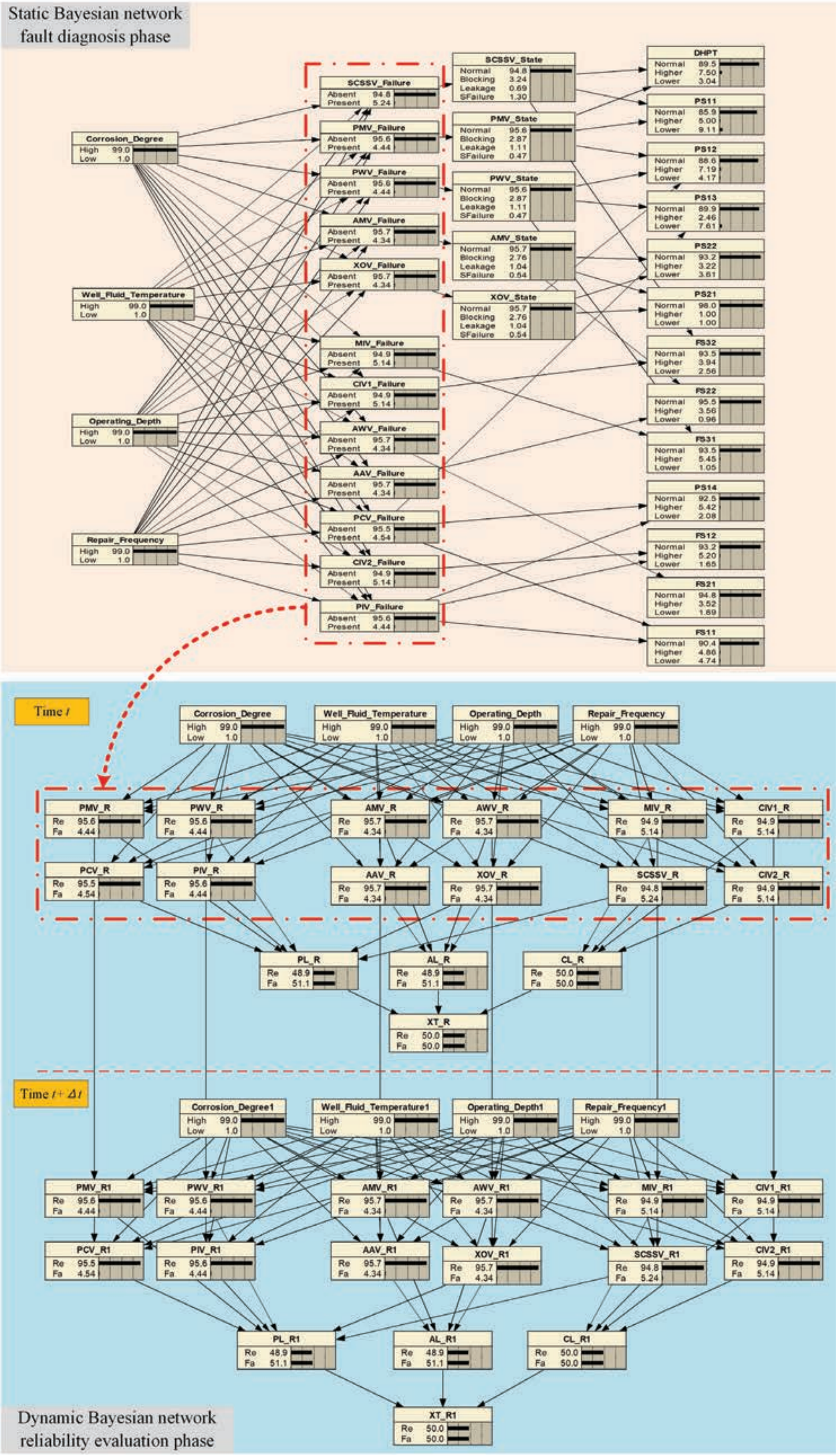

Fig. 10. *Real-time reliability evaluation model of subsea all-electric XT*

cycle law of general electronic control components; therefore, the life cycle of each component conforms to the Weibull distribution; the probability distribution of the life cycle is shown in the following Eq. (7). The proportional parameters $\theta=6800$, and shape parameters $\beta=2.3$ [31] to [33].

$$f(x;\theta,\beta)=\begin{cases}\dfrac{\beta}{\theta}\left(\dfrac{x}{\theta}\right)^{\beta-1}e^{-(x-\theta)^{\beta}} & x\geq 0\\ 0 & x\leq 0\end{cases}. \qquad (7)$$

In the reliability evaluation stage, the three loops of the all-electric XT belong to a series relationship, meaning that if any loop fails, the mechanical system fails. Therefore, the conditional probability tables of the nodes of the loop reliability layer and the Christmas tree reliability layer can be obtained, as shown in Table 2.

Table 2. *CPT for the nodes of the circuit reliability layer and the tree reliability layer*

PL_R(Re) [%]	AL_R(Re) [%]	CL_R(Re) [%]	XT_R(Re) [%]
100	100	100	100
100	100	0	0
100	0	100	0
100	0	0	0
0	100	100	0
0	100	0	0
0	0	100	0
0	0	0	0

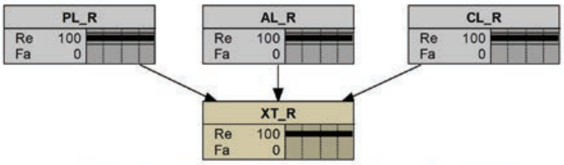

a) PL_R: 100 %, AL_R: 100 %, CL_R: 100 %

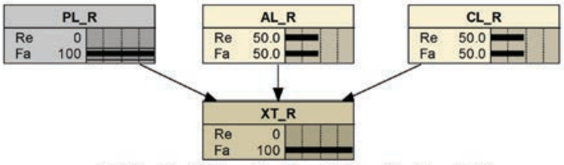

b) PL_R: 0 %, AL_R: 50 %, CL_R: 50 %

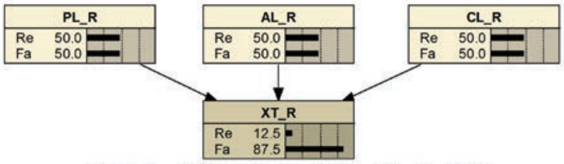

c) PL_R: 50 %, AL_R: 50 %, CL_R: 50 %

Fig. 11. *Bayesian network of circuit reliability layer and tree reliability layer*

The real-time reliability evaluation model of the all-electric XT is shown in Fig. 10. First, the sensor state of the fault symptom layer nodes in the fault diagnosis stage of the static Bayesian network is used to deduce the nodes state of the fault layer in reverse and to obtain component failure rate (probability of “Present”), and whether the component fails is determined by the above judgment rule. Second, the complement of the failure rate of the faulty component is calculated and transformed into the reliability probability of the component and then substituted into the reliability probability of the corresponding node in the component reliability layer of the dynamic Bayesian reliability evaluation stage (probability of “Re”). The reliability probability of the specified time slice interval Δt can be obtained by using dynamic Bayesian network forward derivation.

The probability relationships in Table 3 are substituted into the loop reliability layer and the Christmas tree reliability layer, as shown in Fig. 11. Fig. 11a shows that when the Re probability of the PL_R node, AL_R node and CL_R node are all 100 %, the reliability of the Christmas tree reliability node (XT_R) is 100 %. As shown in Fig. 11b, the reliability probability of any node PL_R, AL_R and CL_R is 0, meaning that when the probability of Fa is 100 %, the Christmas tree mechanical system will fail, meaning that the probability of Fa of XT_R node is 100 %.The reliability probability of the current time slice of the all-electric Christmas tree mechanical system can be derived forwardly through the Bayesian network by obtaining the reliability probability of the three loops, as shown in Fig. 11c.

3 RESEARCH ON REAL-TIME RELIABILITY OF DYNAMIC BAYESIAN NETWORK FOR ALL-ELECTRIC CHRISTMAS TREE

3.1 Verification of Bayesian network model of All-electric Christmas tree

Model verification is an important part of fault diagnosis and reliability analysis. In the static Bayesian network fault diagnosis stage, the Christmas tree test system is used to collect sensor data and determine whether the component has failed, as shown in Fig. 4, and can be compared with fault diagnosis results. The correctness of the fault diagnosis method is verified based on three examples [10], as follows:

(1) When the fault symptom nodes DHPT, PS11, PS12, and PS13 are high, low, low, and low, respectively, the remaining nodes are normal, and SCSSV has safety failure, the fault diagnosis result

is the “SFailure” state probability of SCSSV > 80 %, which is consistent with the actual result.

(2) When the fault symptom nodes DHPT, PS11, PS21, PS22, and FS22 are low, high, high, low and low, respectively, the remaining nodes are normal, and AMV has leakage fault, the fault diagnosis result is the “Leakage” state probability of AMV > 60%. Generally, when the failure probability is greater than 50 %, it indicates that the component has a high risk of fault and should be shut down for maintenance. Therefore, it can be considered that the BN (Bayesian network)-based fault diagnosis method diagnoses that the AMV leakage fault probability is greater than 60 % is consistent with the actual result.

(3) When the fault symptom nodes PS13, PS14, FS11 and, FS32 are low, high, low and high, respectively, and CIV1 failed (the component does not consider safety failure), the fault diagnosis result is the “Present” state probability of CIV1 > 90 %, which is consistent with the actual result.

It is impractical to fully verify the results of the life cycle reliability evaluation of the all-electric XT mechanical system, but Jones et al. proposed a three-axiom-based validation method for reliability evaluation method verification [34]:

Axiom 1. A slight increase/decrease in the prior subjective probabilities of each parent node should certainly result in the effect of a relative increase/decrease of the posterior probabilities of the child node.

Axiom 2. Given the variation of subjective probability distributions of each parent node, its influence magnitude to the child node values should keep consistency.

Axiom 3. The total influence magnitudes of the combination of the probability variations from x attributes (evidence) on the values should always be greater than the one from the set of x-y ($y \in x$) attributes (sub-evidence).

In the initial state, the “Re” state prior probability of the 12 component reliability nodes are all set to 60 %, then the “Re” of the 12 components are increased to 100 % in sequence, and finally the “Re” of the XT_R node are increased in sequence; combined with the three cases in Fig. 12, the Bayesian reliability evaluation model is shown to conform to the Three-axiom-based validation method.

3.2 Real-time Reliability Evaluation of All-electric XT

The value of the time slice interval Δt can be any period when no fault occurs, Δt takes 200 h，400 h，600 h，800 h and 1000 h, etc. The trend of the time slice interval and the reliability of the mechanical system is shown in Fig. 12.

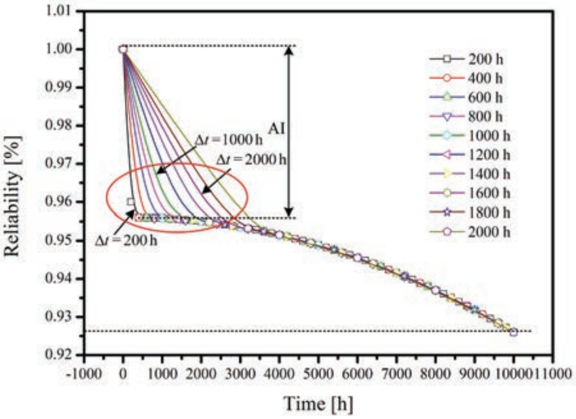

Fig. 12. *Effect of Δt on the tree reliability*

It can be seen from the figure that the time slice interval has little effect on the reliability evaluation of the XT mechanical system; regardless of the value of the time slice interval, the reliability of the mechanical system will eventually become consistent, the reliability of the XT drops rapidly to around 0.958, and then shows a slow downward trend only due to the impact of the additional information layer on the reliability of the mechanical system, and the trend is consistent with the Weibull distribution of the life cycle of the XT. Theoretically, if Δt is reduced by one time, the reliability data points will be doubled. The more data points there are, the more accurate the degradation trend will be depicted. As the degradation curve is fitted by a computer according to the data points, and the number of data points is limited during the 20-year service life of the XT. Therefore, for computers, the impact of increasing limited data points on time costs is not obvious. In other words, the time cost is acceptable. However, the degradation trend of XT reliability is relatively slow, and the degradation trend is not obvious in a short time, so the time slice should be appropriately larger.

The larger the value of the time slice, the better in reducing time cost (although the time cost is acceptable). However, it can be inferred from Fig. 12 that if the value of Δt is too large, the reliability probability point will be lost. If Δt is 2000 h, then data points less than 2000 h will be lost. Therefore, the larger the Δt, the lower the resolution of the obtained reliability degradation curve. If Δt is 10000 h, the obtained reliability curve will become a straight line in Fig. 12. In summary, considering that it can fully describe the degradation trend of system reliability and the slowness of system degradation in a short period, Δt is taken 1000 h in the analysis of this paper.

Evaluating the reliability of the all-electric Christmas tree mechanical system by using the three examples in the previous section, and based on the static Bayesian network fault diagnosis stage, the fault probability of three cases is reversely deduced, as shown in Table 3. The reliability probabilities of a component can be obtained by calculating the complement of component failure probabilities and then substituted into the corresponding node of the dynamic Bayesian network reliability evaluation stage. For example, case 1 in the table, the "Present" probability of the node "PMV_Failure" is 0.0933, which indicates that the reliability probability is 0.9067, then it is replaced to the "Re" state of the node "PMV_R" in the Bayesian network time slice Time t of the reliability evaluation stage, and the forward derivation of reliability is carried out after successive substitution.

Table 3. *Fault diagnosis results of the three cases*

Fault nodes	State	Probability of fault		
		Case 1	Case 2	Case 3
SCSSV_Failure	Present	0.1384	0.3253	0.0696
PMV _Failure	Present	0.0933	0.4691	0.0444
PWV _Failure	Present	0.0647	0.0444	0.0427
PIV_Failure	Present	0.0444	0.0444	0.0444
AMV _Failure	Present	0.0434	0.8561	0.0432
AWV _Failure	Present	0.0434	0.0434	0.0434
AAV _Failure	Present	0.0434	0.0449	0.0449
XOV_Failure	Present	0.0352	0.0367	0.0187
CIV1 _Failure	Present	0.0514	0.0514	0.9411
CIV2 _Failure	Present	0.0514	0.0514	0.4182
MIV_Failure	Present	0.0514	0.0514	0.0514
PCV_Failure	Present	0.0454	0.0454	0.0463

In the state of case 1, the reliability curve of the mechanical system is obtained, as shown in Fig. 13. It is worth noting that in this case, as mentioned above, despite the fault diagnosis result is the "Sfailure" state probability of SCSSV > 80 %, but safety failure is not real failure (need to transfer the XT to land for repair). Safety failure is a temporary failure behaviour; for example, the system crashes due to signal interference. After the interference disappears, the problem can be solved by restarting the system without transferring the XT to land for repair. So it is a self-healing fault. The real failure rate of SCSSV is only 0.1384, as shown in Table 3, which shows that the component still has high reliability, which effectively prevents misjudgement of the fault and avoids the cost of salvage maintenance and detection. Time in the figures represents the time when the failure probability is input into the dynamic Bayesian network; for example, Time = 200 h means that the reverse derivation of the fault diagnosis stage is performed at 200 h. It can be seen from the "no fault" curve that the safety failure of SCSSV has a certain impact on the reliability of the mechanical system, which will cause the reliability of the mechanical system to decrease slowly. When the reliability of the mechanical system drops to 95 % after continuous working for 5000 hours, adequate attention should be paid to safety failure to prevent the failure of the mechanical system. However, if a safety failure occurs, it is detected after 800 hours of system operation (the curve of Time = 800 h); at this time, the safety failure has a greater impact on the reliability of the mechanical system, and if it continues to work, the reliability of the mechanical system will decline rapidly. In summary, the time when the safety failure is detected has a greater impact on the reliability evaluation results of the mechanical system. In addition, it can be seen from the figure that when the mechanical system continues to work for 8000 h, the system reliability presents a rapid decline, and the decline rate is significantly greater than the decline rate of the previous 8000 h. Therefore, when the mechanical system works normally for 8000 h, it is necessary to shut it down for maintenance in order to ensure the stable operation of the system.

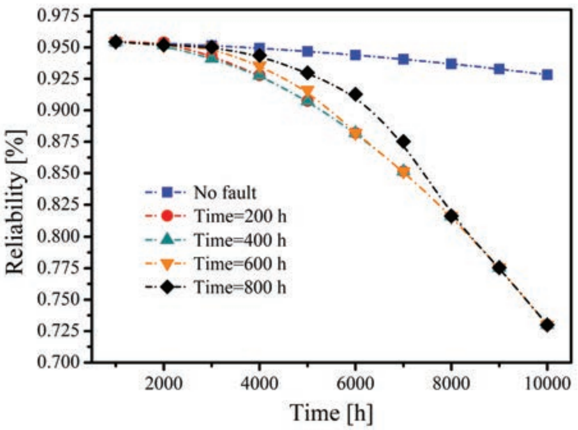

Fig. 13. *Reliability evaluation results of machine system-case 1*

In the state of case 2, when the failure probability of AMV is detected as high as 85.61 %, the reliability of the mechanical system is evaluated, as shown in Fig. 14. Due to AMV failure, the reliability of mechanical system decreases rapidly; at any values of Time (200 h, 400 h, 600 h, 800 h), the mechanical system reliability is less than 10 %, which shows that the failure probability of AMV components has an important impact on the reliability of mechanical systems.

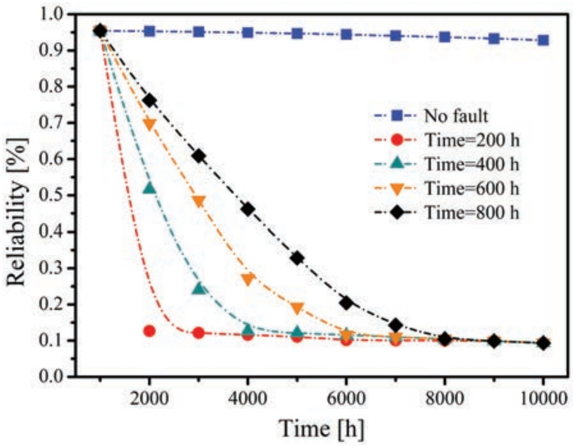

Fig. 14. *Reliability evaluation results of machine system-case 2*

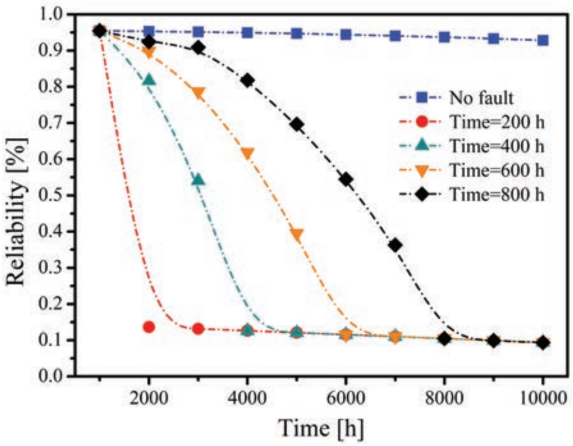

Fig. 15. *Reliability evaluation results of machine system-case 3*

In the state of case 3, when the failure probability of CIV1 is detected to be 94.11 %, the reliability of the mechanical system is evaluated, as shown in Fig. 15. Failure of CIV1 can also cause mechanical system reliability to drop below 10 %; however, the downward trend is significantly less than the impact of AMV on the reliability of mechanical systems. CIV1 is located in the chemical injection loop, and AMV is located in the annulus loop, indicating that the components on the annulus loop have a more obvious influence on the reliability of the mechanical system. In cases 2 and 3, it can be found that if the failure rate of a certain component of the system is too high, the reliability will quickly drop to an extremely low value after the system works for 8000 h. To summarize, whether the system components are malfunctioning or not, 8000 h of continuous system operation is the recommended limit value and should be shut down for maintenance.

3.3 Sensitivity Analysis of All-electric XT

The influence of components on the reliability of the mechanical system is studied by sensitivity analysis, mutual information can be used to analyse the reliability and sensitivity of the XT mechanical system, and mutual information is used to indicate the relationship between two basic events, the reliability of 12 components are considered as 12 basic events, and the reliability of a mechanical system is considered as a basic event, and the mutual information about the reliability of component basic events and mechanical system basic events are calculated in sequence [35]; the calculation formula is as follows:

$$I(X;Y)=\sum_{x\in X}\sum_{x\in Y}P(x,y)\log\frac{P(x,y)}{P(x)P(y)},\qquad(8)$$

where X and Y represent two basic events, $P(x,y)$ is the joint probability distribution function of X and Y, $P(x)$ and $P(y)$ are the edge probability distribution functions of X and Y, respectively. Figs. 16 and 17 are the mutual information values of the reliability of each component and the reliability of the mechanical system for 5,000 hours and 10,000 hours of operation of the mechanical system, respectively.

It can be seen from Fig. 16 that when the mechanical system works for 5000 hours, the SCSSV, PMV, PWV, PCV and PIV components in the production loop have a great influence on the reliability of the mechanical system, SCSSV, PMV, PWV, PCV and PIV components in the production loop have a greater impact on the reliability of the mechanical system, followed by AMV, AWV and AAV components in the annulus loop, and MIV, CIV1 and CIV2 components in the chemical agent injection loop have less impact. The components in the production loop and the annulus loop affect the reliability of the mechanical system by several orders of magnitude higher than the components in the chemical injection loop on the reliability of the mechanical system. Therefore, the reliability of the two-loop components should be guaranteed first. Fig. 17 shows that the mechanical system has the same rule when it works for 10,000 hours; however, with the increase of working time, the mutual information value of the influence of production loop components on the reliability of the mechanical system is increased to more than 0.04239, while the mutual information value of the influence of the chemical injection loop components on the reliability of the mechanical system is reduced to below 0.000104, which indicates that the longer the working time of the mechanical system, the greater the influence of the components on the production loop on the reliability of the mechanical system, More attention should be paid to prevent failures from occurring, so as to avoid major safety accidents.

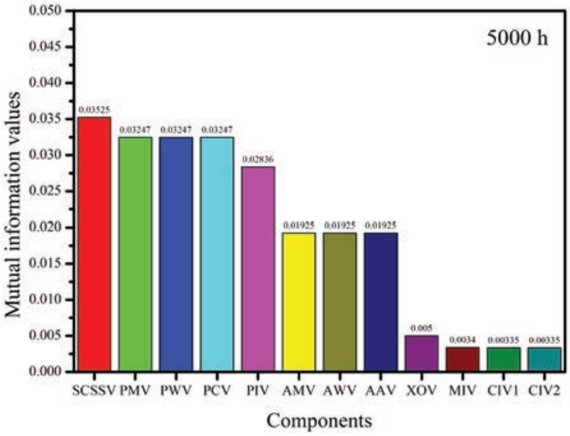

Fig. 16. *Mutual information value of components reliability and machine reliability (5000 h)*

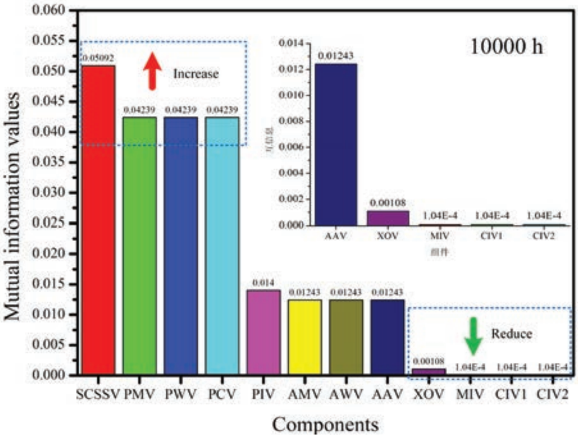

Fig. 17. *Mutual information value of components reliability and machine reliability (10000 h)*

4 CONCLUSION

A real-time reliability evaluation method of an all-electric XT mechanical system incorporating static Bayesian network fault diagnosis stage was proposed in this article. The reliability evaluation model was established, and the influence of the type of failure and component failure rate on the reliability evaluation results under the condition of additional information was studied. The sensitivity of mechanical system reliability was analysed by using mutual information, and the importance of the basic events of each component on the reliability of the mechanical system was revealed. The following conclusions were obtained:

1) The time slice interval had little effect on the reliability evaluation of the XT mechanical system; regardless of the time slice interval, the reliability trend of the mechanical system was basically the same.

2) Safety failure had a certain impact on the reliability of the mechanical system, which would cause the reliability of the mechanical system to decrease slowly. After 5,000 hours of continuous operation, the reliability of mechanical system was reduced to 95 %. However, the time at which the safety failure was detected had a greater impact on the reliability evaluation results of the mechanical system; therefore, it was recommended to use this method to identify, diagnose and real-time reliability assessment of mechanical system faults every 1,000 h.

3) The failure probability of components on the annulus loop included AMV components had a significant impact on the reliability of the mechanical system. If the failure rate of any component were large, it would quickly reduce the reliability of the mechanical system. However, the failure rate of components in the chemical injection loop had less influence on the reliability of the mechanical system.

4) It could be seen from the sensitivity analysis that the longer the working time of the system was, the higher the influence degree of components in the production loop on the system reliability was, while the influence degree of components in the chemical injection loop was lower. Therefore, the failure probability of components in the production loop should be paid more attention during long-term work.

5 ACKNOWLEDGEMENTS

The authors wish to acknowledge the financial support of Shandong Provincial Natural Science Foundation, China (ZR2021QE059), Key R&D Program of Shandong Province (2019GGX101020).

7 REFERENCES

[1] Zhen, X., Vinnem, J. E., Han, Y., Peng, C., Yang, X., & Huang, Y. (2020). New risk control mechanism for innovative deepwater artificial seabed system through online risk monitoring system. *Applied Ocean Research*, vol. 95, art. ID 102054, **DOI:10.1016/j.apor.2020.102054**.

[2] Velayudhan, G., Venugopal, P. R., Gnanasigamony Thankareathenam, E. S., Selvakumar, M., Pudukarai Ramaswamy, T. (2021). Reliability-based design optimization of pump penetration shell accounting for material and geometric non-linearity. *Strojniški vestnik - Journal of Mechanical Engineering*, vol. 67, no. 6, p. 331-340, **DOI:10.5545/sv-jme.2021.7104A**.

[3] Bitanov, A. (2015). *Reliability Study of Subsea Control Module with Focus on Statistical Methods.* MSc thesis, Norwegian University of Science and Technology, Trondheim.

[4] Rozuhan, H., Muhammad, M., Niazi, U.M. (2020). Probabilistic risk assessment of offshore installation hydrocarbon releases leading to fire and explosion, incorporating system and human reliability analysis. *Applied Ocean Research*, vol. 101, art. ID 102282, **DOI:10.1016/j.apor.2020.102282**.

[5] Liu, G., Li, H., Qiu, Z., Leng, D., Li, Z., Li, W. (2020). A mini review of recent progress on vortex-induced vibrations of marine risers. *Ocean Engineering*, vol. 195, art. ID 106704, **DOI:10.1016/j.oceaneng.2019.106704**.

[6] Liu, P., Liu, Y., Wei, X., Xin, C., Sun, Q., Wu, X. (2019). Performance analysis and optimal design based on dynamic characteristics for pressure compensated subsea all-electric valve actuator. *Ocean Engineering*, vol. 191, art. ID 106568, **DOI:10.1016/j.oceaneng.2019.106568**.

[7] Wanvik, P. G. (2015). *Reliability Assessment of Subsea X-Mas Tree Configurations*. MSc. thesis, Norwegian University of Science and Technology, Trondheim.

[8] Qin, B., Li, Z., Qin, Y. (2020). A transient feature learning-based intelligent fault diagnosis method for planetary gearboxes. *Strojniški vestnik - Journal of Mechanical Engineering*, vol. 66, no. 6, p. 385-394, **DOI:10.5545/sv-jme.2020.6546**.

[9] Labovská, Z., Labovský, J., Jelemenský, Ľ., Dudáš, J., Markoš, J. (2014). Model-based hazard identification in multiphase chemical reactors. *Journal of Loss Prevention in the Process Industries*, vol. 29, p. 155-162, **DOI:10.1016/j.jlp.2014.02.004**.

[10] Liu, P., Liu, Y., Cai, B., Wu, X., Wang, K., Wei, X., Xin, C. (2020). A dynamic Bayesian network based methodology for fault diagnosis of subsea Christmas tree. *Applied Ocean Research*, vol. 94, art. ID 101990, **DOI:10.1016/j.apor.2019.101990**.

[11] Panić, B., Klemenc, J., Nagode, M. (2020). Gaussian mixture model based classification revisited: application to the bearing fault classification. *Strojniški vestnik - Journal of Mechanical Engineering*, vol. 66, no. 4, p. 215-226, **DOI:10.5545/sv-jme.2020.6563**.

[12] Feng, G., Wang, D., Garbatov, Y., Soares, C.G. (2015). Reliability analysis based on a direct ship hull strength assessment. *Journal of Marine Science and Application*, vol. 14, p. 389-398, **DOI:10.1007/s11804-015-1328-4**.

[13] Nhat, D.M., Venkatesan, R., Khan, F. (2020). Data-driven Bayesian network model for early kick detection in industrial drilling process. *Process Safety and Environmental Protection*, vol. 138, p. 130-138, **DOI:10.1016/j.psep.2020.03.017**.

[14] Wang, C., Liu, Y., Hou, W., Wang, G., Zheng, Y. (2020). Reliability and availability modeling of Subsea Xmas tree system using Dynamic Bayesian network with different maintenance methods. *Journal of Loss Prevention in the Process Industries*, vol. 64, art. ID 104066, **DOI:10.1016/j.jlp.2020.104066**.

[15] Li, X., Chen, G., Zhu, H. (2016). Quantitative risk analysis on leakage failure of submarine oil and gas pipelines using Bayesian network. *Process Safety and Environmental Protection*, vol. 103, p. 163-173, **DOI:10.1016/j.psep.2016.06.006**.

[16] Wang, W., Shen, K., Wang, B., Dong, C., Khan, F., Wang, Q. (2017). Failure probability analysis of the urban buried gas pipelines using Bayesian networks. *Process Safety and Environmental Protection*, vol. 111, p. 678-686, **DOI:10.1016/j.psep.2017.08.040**.

[17] Liu, Z., Liu, Y., lei Wu, X., Cai, B. (2018). Risk analysis of subsea blowout preventer by mapping GO models into Bayesian networks. *Journal of Loss Prevention in the Process Industries*, vol. 52, 54-65, **DOI:10.1016/j.jlp.2018.01.014**.

[18] Li, M., Wang, H., Wang, D., Shao, Z., & He, S. (2020). Risk assessment of gas explosion in coal mines based on fuzzy AHP and bayesian network. *Process Safety and Environmental Protection*, vol. 135, p. 207-218, **DOI:10.1016/j.psep.2020.01.003**.

[19] Lyu, S., Duan, M., Liang, W., Chen, J., Xie, Z. (2014). Reliability evaluation for subsea x-mas tree control system based on Bayesian networks. *The Twenty-fourth International Ocean and Polar Engineering Conference*, Busan.

[20] Zhang, J., Liu, Y., Lundteigen, M., & Bouillaut, L. (2016). Using Bayesian networks to quantify the reliability of a subsea system in the early design. *Risk, Reliability and Safety: Innovating Theory and Practice: Proceedings of ESREL*, 404.

[21] Tidriri, K., Chatti, N., Verron, S., Tiplica, T. (2016). Bridging data-driven and model-based approaches for process fault diagnosis and health monitoring: A review of researches and future challenges. *Annual Reviews in Control*, vol. 42, 63-81, **DOI:10.1016/j.arcontrol.2016.09.008**.

[22] Qian, P., Ma, X., Cross, P. (2017). Integrated data-driven model-based approach to condition monitoring of the wind turbine gearbox. *IET Renewable Power Generation*, vol. 11, no. 9, p. 1177-1185, **DOI:10.1049/iet-rpg.2016.0216**.

[23] Zou, J., Chang, Q., Arinez, J., Xiao, G., Lei, Y. (2017). Dynamic production system diagnosis and prognosis using model-based data-driven method. *Expert Systems with Applications*, vol. 80, p. 200-209, **DOI:10.1016/j.eswa.2017.03.025**.

[24] Simani, S., Farsoni, S. (2018). *Fault Diagnosis and Sustainable Control of Wind Turbines: Robust Data-Driven and Model-Based Strategies*. Butterworth-Heinemann, Oxford.

[25] Wang, Q., Li, F., Tang, Y., Xu, Y. (2019). Integrating model-driven and data-driven methods for power system frequency stability assessment and control. *IEEE Transactions on Power Systems*, vol. 34, no. 6, p. 4557-4568, **DOI:10.1109/TPWRS.2019.2919522**.

[26] Wu, S., Zhang, L., Zheng, W., Liu, Y., Lundteigen, M.A. (2016). A DBN-based risk assessment model for prediction and diagnosis of offshore drilling incidents. *Journal of Natural Gas Science and Engineering*, vol. 34, p. 139-158, **DOI:10.1016/j.jngse.2016.06.054**.

[27] Li, W., Poupart, P., van Beek, P. (2011). Exploiting structure in weighted model counting approaches to probabilistic inference. *Journal of Artificial Intelligence Research*, vol. 40, p. 729-765, **DOI:10.1613/jair.3232**.

[28] Cai, B., Zhao, Y., Liu, H., Xie, M. (2017). A data-driven fault diagnosis methodology in three-phase inverters for PMSM drive systems. *IEEE Transactions on Power Electronics*, vol. 32, no. 7, p. 5590-5600, **DOI:10.1109/TPEL.2016.2608842**.

[29] Zou, X., Yue, W.L. (2017). A Bayesian Network Approach to Causation Analysis of Road Accidents Using Netica. *Journal of Advanced Transportation*, vol. 2017, art. ID 2525481, **DOI:10.1155/2017/2525481**.

[30] Cai, B., Liu, Y., Ma, Y., Liu, Z., Zhou, Y., Sun, J. (2015). Real-time reliability evaluation methodology based on dynamic Bayesian networks: A case study of a subsea pipe ram BOP system. *ISA Transactions*, vol. 58, p. 595-604, **DOI:10.1016/j.isatra.2015.06.011**.

[31] Rinne, H. (2009). *The Weibull Distribution: A Handbook*. CRC Press, Boca Raton.

[32] Thoman, D.R., Bain, L.J., Antle, C.E. (1969). Inferences on the parameters of the Weibull distribution. *Technometrics*, vol. 11, no. 3, p. 445-460, **DOI:10.1080/00401706.1969.10490706**.

[33] Cohen, A.C. (1965). Maximum likelihood estimation in the Weibull distribution based on complete and on censored samples. *Technometrics*, vol. 7, no. 4, p. 579-588, **DOI:10.1080/00401706.1965.10490300**.

[34] Jones, B., Jenkinson, I., Yang, Z., & Wang, J. (2010). The use of Bayesian network modelling for maintenance planning in a manufacturing industry. *Reliability Engineering & System Safety*, vol. 95, no. 3, p. 267-277, **DOI:10.1016/j.ress.2009.10.007**.

[35] Kraskov, A., Stögbauer, H., Grassberger, P. (2004). Estimating mutual information. *Physical Review E*, vol. 69, no. 6, art. ID 066138, **DOI:10.1103/PhysRevE.69.066138**.

Strojniški vestnik - Journal of Mechanical Engineering 68(2022)1, 56-65
© 2022 The Authors. CC BY-NC 4.0 Int. Licensee: SV-JME
DOI:10.5545/sv-jme.2021.7384
Original Scientific Paper
Received for review: 2021-08-31
Received revised form: 2021-11-02
Accepted for publication: 2021-12-06

Early Detection of Defects in Gear Systems Using Autocorrelation of Morlet Wavelet Transforms

Mouloud Ayad[1,2] – Kamel Saoudi[1,2] – Mohamed Rezki[1] – Mourad Benziane[1,2] – Abderrazak Arabi[3]
[1]University of Bouira, Faculty of Sciences and Applied Sciences, Department of Electrical Engineering, Algeria
[2] University of Bouira, LPM3E Laboratory, Algeria
[3] University of Sétif 1, LIS Laboratory, Algeria

The supervision task of industrial systems is vital, and the prediction of damage avoids many problems. If any system defects are not detected in the early stage, this system will continue to degrade, which may cause serious economic loss. In industrial systems, the defects change the behaviour and characteristics of the vibration signal. This change is the signature of the presence of the defect. The challenge is the early detection of this signature. The difficulty of the vibration signal is that the signal is very noisy, non-stationary and non-linear. In this study, a new method for the early defect detection of a gear system is proposed. This approach is based on vibration analysis by finding the defect's signature in the vibration signal. This approach has used the autocorrelation of Morlet wavelet transforms (AMWT). Firstly, simulation validation is introduced. The validation of the approach on a real system is given in the second validation part.

Keywords: Autocorrelation of Morlet Wavelet Transforms, early fault diagnosis, gear systems, Vibration analysis, Scalograms

Highlights

- *A new approach for early defect detection of a gear system is proposed.*
- *The autocorrelation of Morlet wavelet transforms (AMWT) is used to detect the presence of faults.*
- *The study is based on both simulation and experimental validation.*
- *This approach helps the professionals in the supervision of mechanical systems.*

0 INTRODUCTION

Supervision of industrial systems is an essential task to guarantee performance and reliability. The crucial key of this supervision is understanding the equipment behaviour, and the information extracted can be used for planning maintenance activities. Therefore, the monitoring aims to increase profitability by reducing downtime and increasing the lifetime of the equipment. Consequently, the early detection of defects in mechanical systems is essential for operators and has attracted the attention of many researchers in recent years [1] to [6]. They aim to plan to repair these systems rather than catastrophic damage caused by unexpected defects. The most well-known techniques for the prevention of rotating systems are temperature control (thermography) [7] and [8], oil debris control [9] and [10], acoustic analysis [11] and [12] and vibration signal control (analysis) [13] and [14]. The significant advantage of vibration analysis is that it can detect and identify the defect evolution before it becomes severe and causes catastrophic damage. This can be accomplished by the regular monitoring of the vibration machine. Therefore, the monitoring aim is to increase productivity by reducing downtime and increasing the lifetime of the equipment.

There are several techniques in the literature proposed for early fault detection based on vibration analysis. In general, there are three domains of vibration signal processing for defect diagnosis of rotating machines: time domain, frequency domain, and time-frequency domain. The basic principle of vibration analysis is based on the fact that a change in the mechanical system's conditions can induce a change in the vibrations produced by this system. In simple systems, this change can affect the shape by an increase in the amplitude of the signal. For complex systems, the detection of change in the vibration signal, affected by the deterioration of the system, is very complicated and more sophisticated techniques of detection are required.

A gear system is an essential element usually used in a range of industrial systems. Therefore, accurate and early defect detection and correct diagnoses are vital to normal machinery operations. When a localized defect occurs in gears, the characteristics of periodic impulsive of the signal appear in the time domain, and the corresponding frequency components will be affected. However, an effective signal analysis approach is needed to eliminate noise and interference. In the literature, several approaches are proposed. For example, Matic and Kanovic [13] used the vibration signal analysis based on current signal

*Corr. Author's Address: University of Bouira, 1000, Bouira, Algeria, m.ayad@univ-bouira.dz

analysis by observing fault frequency content to detect a broken bar fault. In **[14]**, a reassigned short-time Fourier transform (RSTFT) is presented to identify the sideband components related to the failure of the broken rotor bar in the induction motors. Wang et al. **[15]** propose an adaptive parameter identification method for gearbox defect detection. It combines the Morlet wavelet and the correlation filtration for characterizing both the cyclic period between adjacent impulses and the impulse response.

In this work, we propose a new approach based on the autocorrelation function of Morlet wavelet transforms. This approach is applied firstly on simulated signals, and secondly on real gear signals for the early detection of defects present in an experimental tested gear system.

The remainder of this present work is planned as follows: in Section 2, the theoretical background of AMWT is given. Next, the simulation validation is introduced in Section 3. In Section 4, the obtained results and the validation of the approach on a real system are given.

1 THEORETICAL BACKGROUND

In this section, we explain the approach proposed for the fault diagnosis of a gear system. This approach is based on the autocorrelation of Morlet wavelet transforms (AMWT). Therefore, we give the background of the Morlet wavelet transform (MWT) and then the autocorrelation of Morlet wavelet transform (AMWT).

1.1 Morlet Wavelet Transform

The wavelet transform can address the problem of temporal and frequency resolution through multi-resolution analysis. As the name signifies, multi-resolution analysis allows for different temporal and frequency resolutions. It provides an excellent frequency resolution (i.e., poor temporal resolution) at low frequencies and an excellent temporal resolution (i.e., a poor frequency resolution) at high frequencies. This analytical approach is particularly advantageous for signals with low-frequency components for an extremely short period and high-frequency components for relatively extended periods. For the non-stationary signals analysis, the wavelet transform is adequate because it provides a simultaneous localization of time and frequency.

For any signal $x(t)$, the continuous wavelet transform (CWT) is given by:

$$\mathrm{CWT}_{x(t)} = |a|^{-1/2} \int_{-\infty}^{+\infty} x(t) \Psi^* \left(\frac{t-b}{a}\right) dt, \tag{1}$$

where * is the symbol of a complex conjugate function; a the parameter of dilation, b the parameter of translation, and Ψ represent the mother wavelet represented by **[15]**:

$$\Psi_{a,b}(t) = |a|^{-1/2}\, \Psi\left(\frac{t-b}{a}\right). \tag{2}$$

The translation parameter controls the shifting position, and the dilation parameter controls the oscillation frequency **[16]** and **[17]**.

The wavelet of Morlet represents functions with the form of small waves created by dilations and translations from the mother wavelet given by **[4]**:

$$\Psi(t) = \exp\left(j2\pi f_c t\right) \exp\left(-t^2 / f_b\right), \tag{3}$$

where f_b is the parameter of bandwidth, and f_c the central frequency of the wavelet.

These two parameters control the form of the Morlet wavelet.

After calculating the CWT, we calculate the scalogram defined as the square of the CWT module.

1.2 Autocorrelation of Morlet Wavelet Transform

Random vibrations are inherently unpredictable, so the future values of the signal can be defined only based on probabilities. We consider the random signal to be the stochastic process realization, i.e., the time evolution of a random variable. We speak about the cyclostationnarity of a stochastic process representing the signal when the government's statistical parameters that govern vary periodically. The autocorrelation function calculates the internal dependencies of the signal. For example, in the case of the sinusoidal signal, the autocorrelation coefficients are highly uniform and homogeneous; therefore, the signal will have a strong autocorrelation. The rotating machine's vibration signals consist of periodic and random components.

The autocorrelation function $Rx(t)$ of a signal $x(t)$, is usually the cross-correlation of the signal $x(t)$ with itself. The cross-correlation of a signal $x(t)$ and $y(t)$ is given by the expression **[18]** and **[19]**:

$$R_{xy(t)} = \sum_{n=0}^{\infty} x(n) y(n+r), \tag{4}$$

where r is a time step.

If $x(n) = y(n)$, the Eq. (4) becomes an autocorrelation function:

$$R_x(t) = E\left[x(t), x(t-\tau)\right], \tag{5}$$

where τ is the specific time step (lag). E [,] is the expectation or averaging operator.

The autocorrelation of an ergodic process is defined by:

$$R_x(t) = \lim_{T \to \infty} \int_0^T x(t)x(t+\tau)dt. \tag{6}$$

The autocorrelation attains its peak in the beginning:

$$\left|R_x(\tau)\right| \leq \left|R_x(0)\right|. \tag{7}$$

The autocorrelation of the wavelet coefficients is the integral of the product of the wavelet transform $WT_{a,b}(t)$ with itself delayed by (τ) according to the following equation:

$$R_{xx}(t) = \int_{-\infty}^{+\infty} WT_{a,b}(t) \times WT_{a,b}(t+\tau)dt. \tag{8}$$

The autocorrelation function reaches its maximum peak at the centre. We call this centre point a maximum peak point (MPP). Suppose the size of a function $x(t)$ is equal to M where $M>1$), the autocorrelation function has a dimension of $2\times(M-1)$. The proposed method for predicting defects of rotating machines consists of calculating the autocorrelation of the Morlet wavelet transform (MWT). In this case, the MWT is a two-dimensional matrix ($M\times N$), and in consequence, the autocorrelation function will also be two dimensional ($\mathbf{O}\times\mathbf{P}$) with $\mathbf{O} = 2\times(M-1)$ and $P = 2\times N-1$.

2 SIMULATION EVALUATION

In this part, the performance of the proposed approach is examined on simulated signals. The vibration signals measured in the gear systems are very complicated and have multi-components: tooth vibration, vibration of gear shaft rotation, gear resonance vibration and vibration due to various gearing defects. To simulate these various vibration components and evaluate the performance and efficiency of the method, we have used the test signals available in the scientific literature. It is noted here that the autocorrelation function is expressed in three dimensions. To make it possible to estimate the values of the autocorrelation function, we have given another visualization based on the contour of the autocorrelation.

2.1 Amplitude and Frequency Modulation

The change in the mechanical conditions of a gear system can produce changes in generated vibration signal [20]. These changes can take the form of an increase in amplitude or frequency, which will lead to amplitude or frequency modulation. In general, frequency modulation is significantly less significant than amplitude modulation [21].

The following equation gives the test signal modulated in frequency and amplitude:

$$s(t) = \left[1 + 0.5 \times \sin(6 \times \pi \times t)\right] \times \sin(100 \times \pi \times t^2). \tag{9}$$

The temporal representations of the signal modulated in frequency and amplitude of Eq. (9) and its MWT scalograms and AMWT autocorrelation are given in Fig. 1.

The scalograms of this signal (Fig. 1a) demonstrate the presence of amplitude and frequency modulation. We observe this modulation: the amplitude modulation results in the amplitude variations of the coefficients and the frequency modulation by their non-linear localisation. The representation of the autocorrelation of a signal modulated in frequency and amplitude is given in Figs. 1c and d. In this case, the MPP point has an amplitude of MPP(1000, 25) = 1.1369177×10^6.

2.2 Simulation of the Gear Vibration Signal

In real systems, to facilitate diagnostic and predictive techniques for gear systems, it is necessary to simulate models in which defects can be implemented under different operating conditions instead of waiting for the natural occurrence of these defects. Many models of meshing signals have been proposed in the literature [18] and [20] to [22]. In our case, we will use two models of the gear signal; it is the gear vibration signal simulated by McFadden [20] and the one introduced by Qin et al. [22]. The first model proposed in the literature is that of McFadden [20]. This model is also used by several researchers: Yin et al. [21], Man et al. [23] and others.

2.3 Case Study 1: Gear Simulated by Qin

For rotating machines, the measured signal is the sum of the components of the signal generated by the different mechanisms of the machines. The monitoring of the machine is allowed by the analysis of the vibration signal. However, the essential defect characteristics are incorporated into the components of the signal. In several cases, obtaining the defect information directly from the original signal is a challenging task. Therefore, the useful components must be separated from the measured signal. The

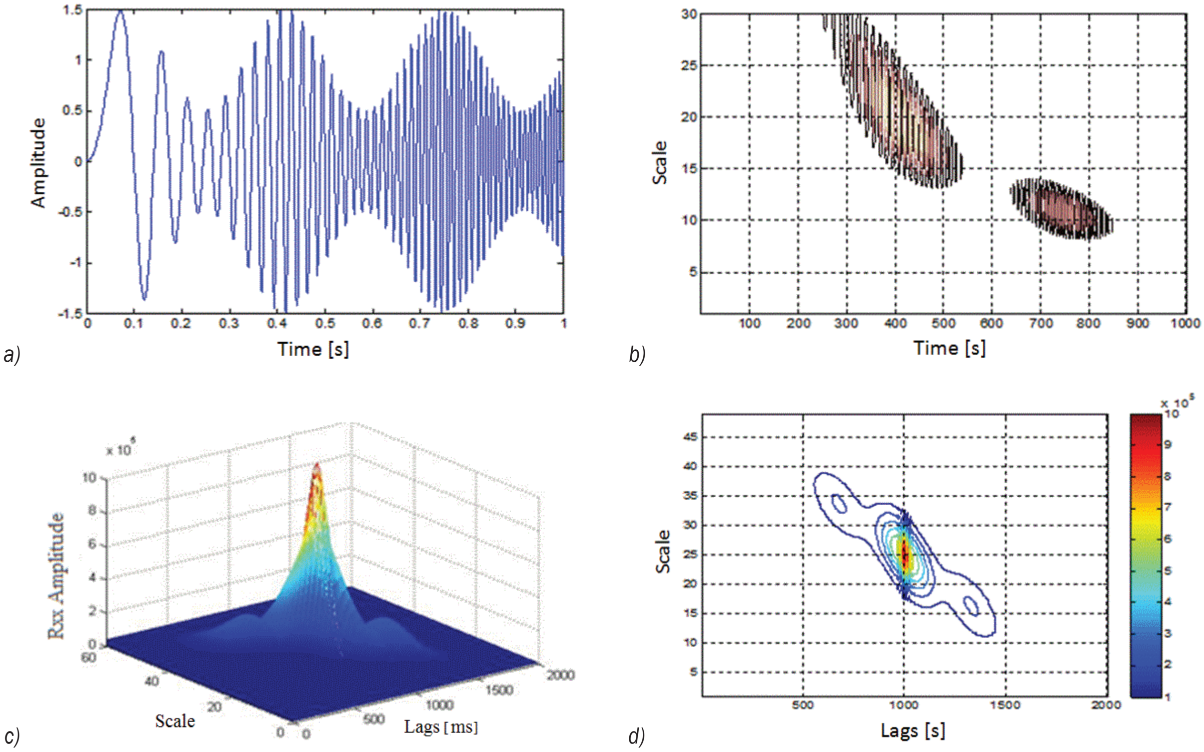

Fig. 1. *Signal modulated in amplitude and frequency; a) temporal representation, b) MWT scalograms, c) AMWT autocorrelation, and d) contour of AMWT autocorrelation*

components of the signal are pulses, harmonics and modulated components [22].

In local defects, for example, crack, tooth break, etc., the impulsive force of gear meshing generates a variation in amplitude and the phase of the vibration signal. These variations generate amplitude and phase modulation. In this case, the spectrum analysis of the envelope is an efficient approach for extracting defect information. The gear vibration signal simulated by Qin et al. [22] is given by $x(t)$:

$$x(t) = x_1(t) + x_2(t) + x_3(t), \tag{10}$$

with:

$$x_1(t) = [0.4 + 0.4\sin(2\pi \times 10t)] \times \cos[2\pi \times 700t + 1.5\sin(2\pi \times 10t)], \tag{11}$$

$$x_2(t) = [1 + \sin(2\pi \times 5t)] \times \cos[2\pi \times 350t + \sin(2\pi \times 5t)], \tag{12}$$

$$x_3(t) = [0.6 + 0.6\cos(2\pi \times 5t)] \times \cos[2\pi \times 200t + 0.6\sin(2\pi \times 5t)]. \tag{13}$$

The sampling frequency is 3 kHz. In general, the gear vibration signal is always accompanied by noise. Hence studying the simulated gear vibration signal with noise is necessary. To this end, we added white noise to the gear vibration signal of Qin et al. [22]. Fig. 2a shows the temporal representation of the defective gear signal simulated by Qin et al. [22], with noise.

In the case in which the signal is embedded in the noise, the effect of the modulation is present on the scalograms. We observe an amplitude peak at the MPP point equal to MPP(1000, 30) = 6.27234110×10^7.

2.4 Case study 2: Gear Defects Simulated by McFadden

The meshing vibration signal is periodic and simultaneously modulated in frequency and amplitude by a periodic signal equal to the period of gear meshing. In general, amplitude modulation is more critical than frequency modulation [21].

Consider a pair of gears that mesh with constant load and speed, with several different teeth. Thus, the vibration signal $x(t)$ of meshing without defect is given by [20]:

$$x(t) = \sum_{m=0}^{M} X_m \cos(2 \cdot \pi \cdot m \cdot Z \cdot f_r \cdot t + \phi_m), \tag{14}$$

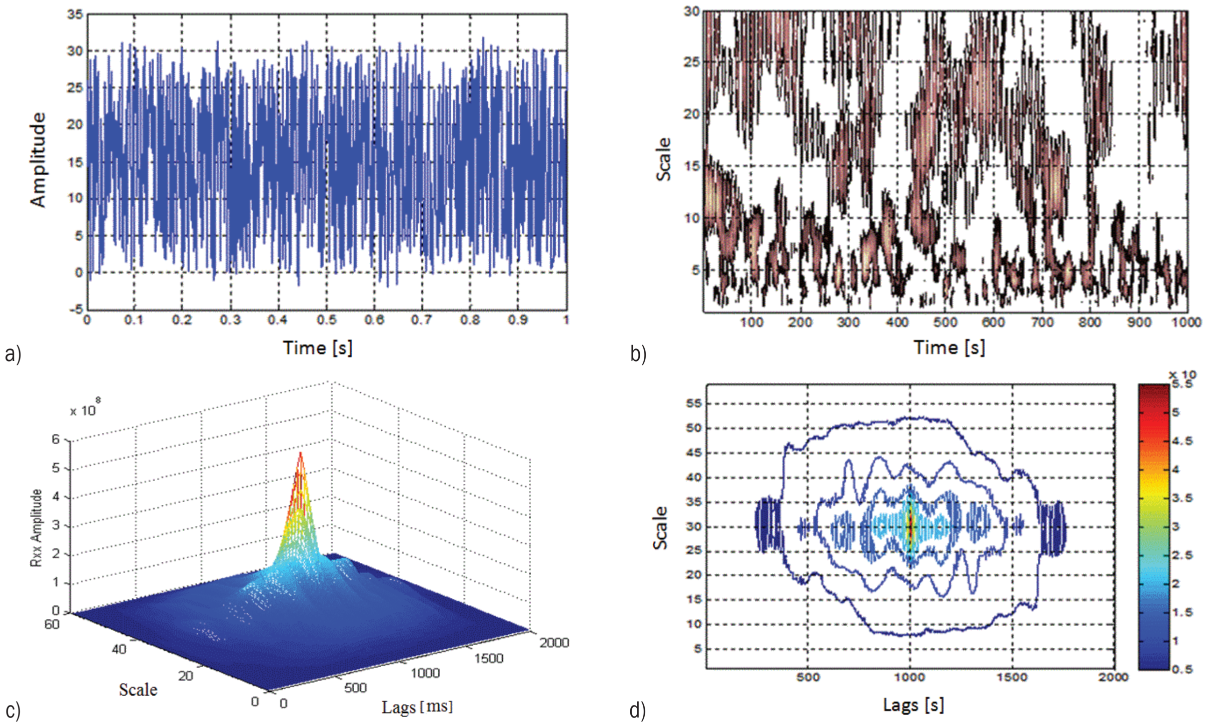

Fig. 2. *Gear vibration signal of Qin; a) temporal representation, b) MWT scalograms, c) AMWT autocorrelation and d) contour of AMWT autocorrelation*

where M is the range of analysis, X_m the amplitude of the harmonic [m], Z the number of teeth, f_r the rotation frequency of the tree, and ϕ_m the phase.

If the gear has a fault (crack, for example), this will affect the meshing signal's phase and amplitude modulation. The modulated signal is given [20], [21] and [23] by:

$$y(t)=\sum_{m=0}^{M}X_m\left[1+a_m(t)\right]\times \cos\left[2.\pi.m.Z.f_r.t+\phi_m+b_m(t)\right], \qquad (15)$$

where

$$a_m(t)=\sum_{n=0}^{p}A_{mn}\cos(2\cdot\pi\cdot m\cdot f_r\cdot t+\alpha_{mn}), \qquad (16)$$

$$b_m(t)=\sum_{n=0}^{p}B_{mn}\cos(2\cdot\pi\cdot m\cdot f_r\cdot t+\beta_{mn}). \qquad (17)$$

$a_m(t)$ and $b_m(t)$ are respectively the functions of amplitude and frequency modulations of the meshing signal caused by the tooth defect.

α_{mn} and β_{mn} are respectively the phases of $a_m(t)$ and $b_m(t)$.

To give this study a near meaning to the real signals, we used the cinematic characteristics of the Centre d'Etudes Techniques des Industries Mécaniques (CETIM) test bench.

Fig. 3 shows the defective gear vibration signal of McFadden with white noise.

The concentration of the scalogram coefficients of the MWT (Fig. 3b) at the moments when the amplitude peaks are at the maximum is the signature of the presence of the defects.

The representation of the autocorrelation of a signal modulated in amplitude is given in Figs. 3c and d.

We observe a set of amplitude peaks and a maximum peak at the MPP point of amplitude equal to MPP(4000, 30) = $4.959990453486705\times10^{19}$.

3 RESULTS AND DISCUSSION

To evaluate the efficacy of AMWT, we have examined the proposed method on accurate signals carried out in CETIM [4], [21] and [25]. The system under study is a gear of two wheels (of 20 and 21 teeth). The system operates for 11 days under identical conditions. Every day, the system was examined, and a report about the state of the gear system was delivered.

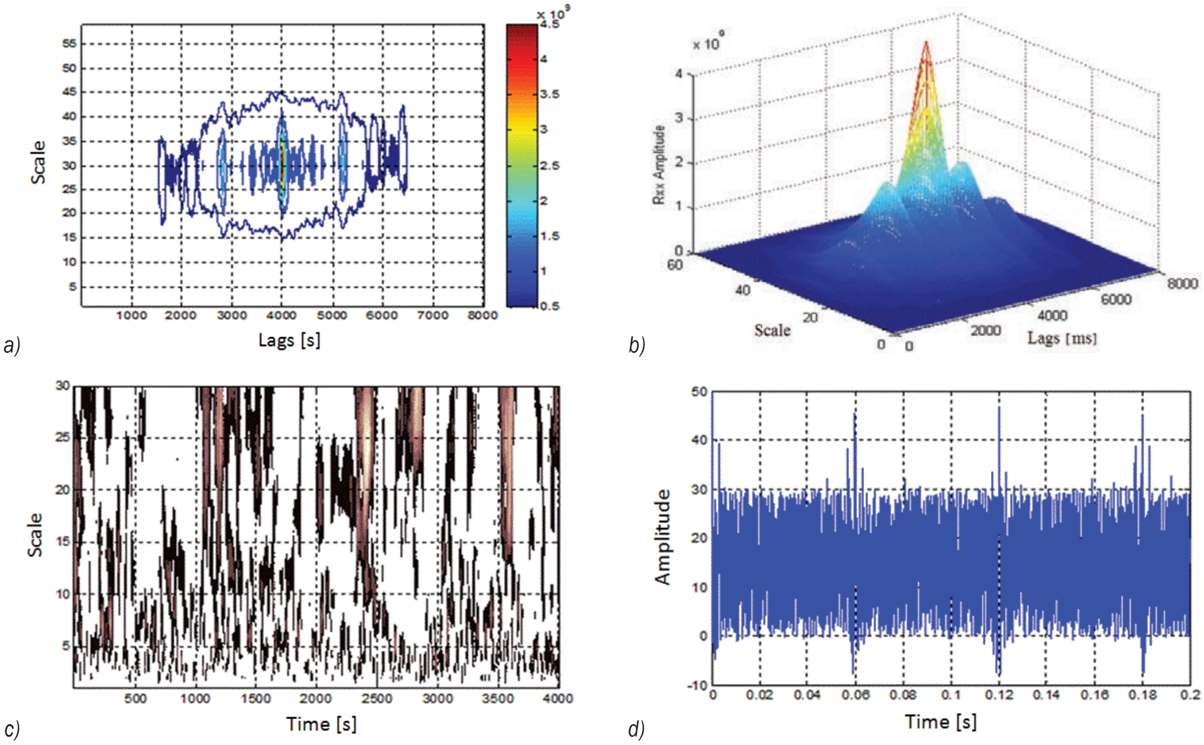

Fig. 3. *Defective gear vibration signal of McFadden; a) temporal representation, b) MWT scalograms, c) AMWT autocorrelation, and d) contour of AMWT autocorrelation*

The studied mechanical system is given in Fig. 4. The expertise report of the experimental system is given in Table 1.

Table 1. *The expertise report of the experimental system* [25]

Day	Observations
1	No anomaly (beginning of the acquisition)
2	No anomaly
3	// //
4	// //
5	Crack of tooth N° (1/2)
6	No evolution
7	Tooth N° (1/2) no evolution, tooth N° (15/16) start of crack
8	Evolution of crack in the tooth N° (15/16)
9	// //
10	// //
11	Crack in all width of the tooth N° (15/16)
12	No anomaly (beginning of the acquisition)

3.1 Temporal and Frequency Spectrums

The representations of the temporal vibration signals of the gear system are given in Figs. 4a, b, c and d. We have given the temporal representation of the days: 9, 10, 11 and 12, i.e., one day before the appearance of the defect and two days after, we arrive to detect the defect on the 10th day.

From Figs. 4a, b, c and d, we observe that the temporal representations of vibratory signals $x(t)$ are approximately similar from the 1st until the 11th day. However, on the 12th day, the behaviour of vibratory signal $x(t)$ is changed, which is translated by a defect of the tooth deterioration (expertise report in Table 1). The change in the behaviour of the signal vibratory in temporal representation is an indication of the presence of the defect. In consequence, the temporal representation does not detect the presence of the defect early stage.

To prove the method's advantages, we have introduced the fast Fourier transform (FFT) as a comparative study.

The corresponding frequency spectrums of the vibratory signals are shown in Figs. 4a', b', c' and d'.

The side lines are very important on the 12th day compared to other days, and this increase is due to the presence of a defect due to the deterioration of a tooth. Thus, the temporal and frequency representation make it possible to diagnose a defect on the last day (12th day) and not in the early stage why the necessity of another approach for the early detection.

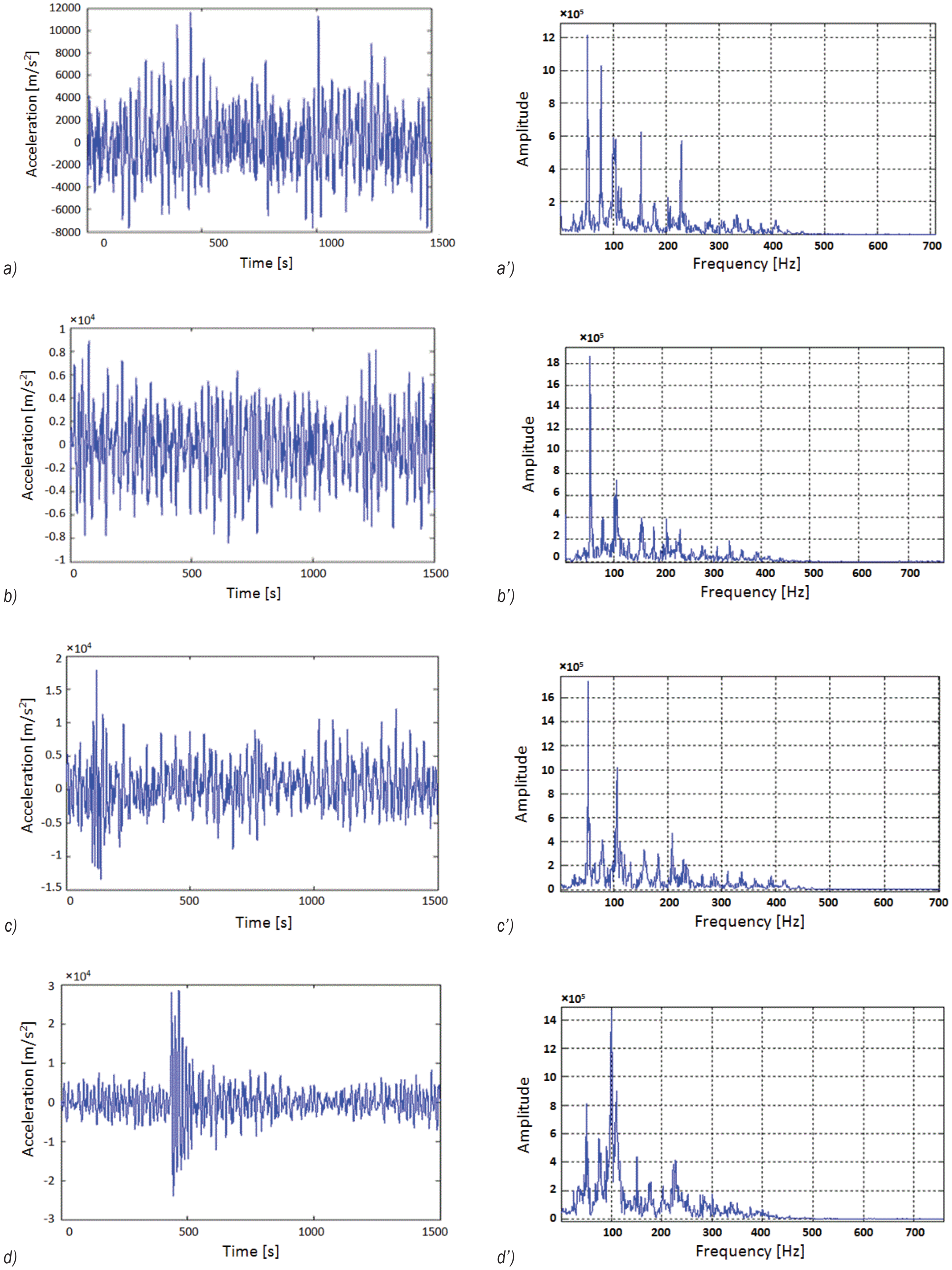

Fig. 4. *Vibration signals and corresponding frequency spectrums of CETIM gear vibration signal; a, a') 9th day, b, b') 10th day, c,c') 11th day, and d, d') 12th day*

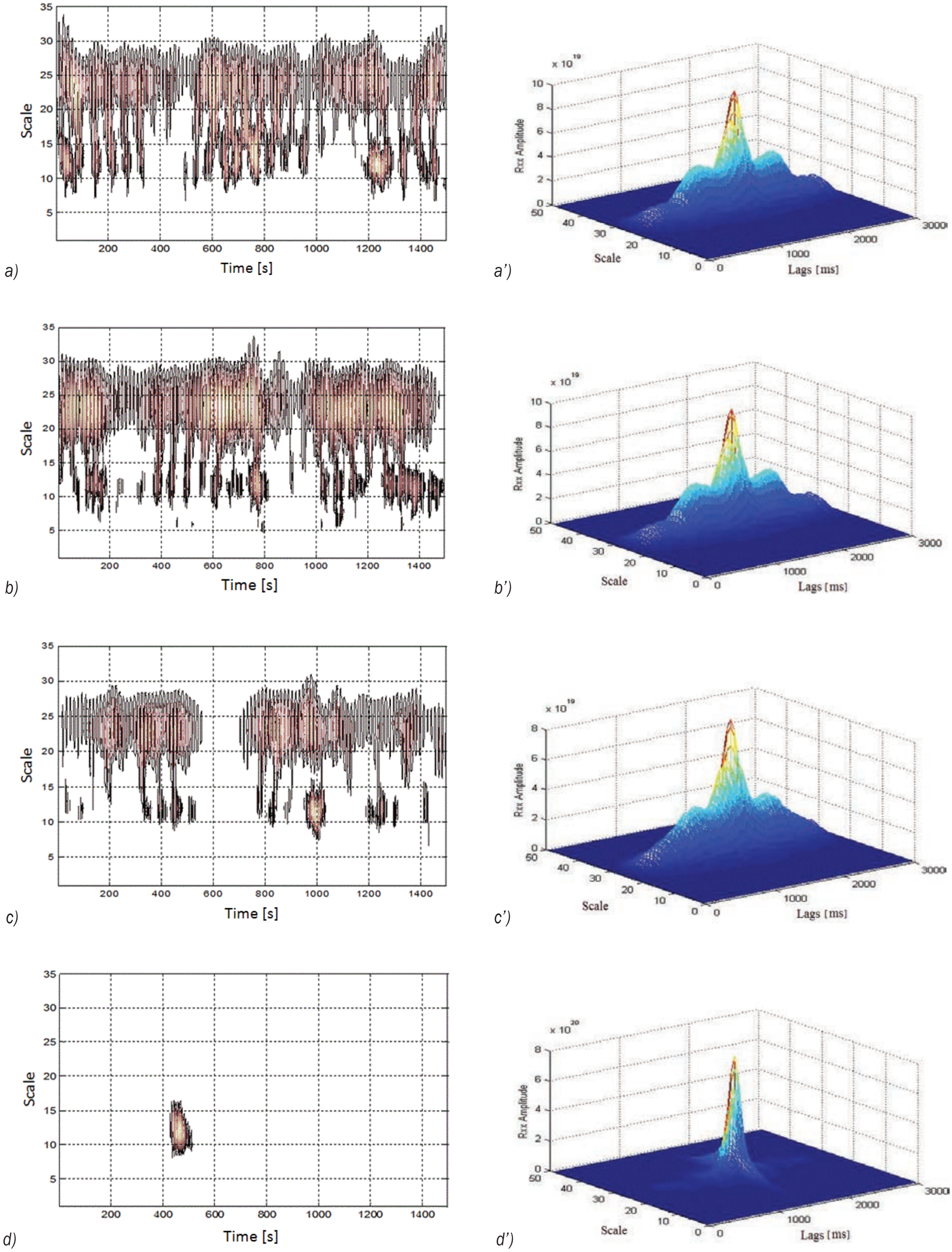

Fig. 5. *Scalograms and corresponding AMWT of CETIM gear vibration signal; a, a') 9th day; b, b') 10th day; c, c') 11th day, and d, d') 12th day*

3.2 Scalograms Representations and the Autocorrelation of the AMWT

In this part, we apply the approach of the autocorrelation function on scalograms obtained by applying the MWT on vibration signal issued from the CETIM gearbox. The representations of the scalograms and the corresponding AMWT are given in Fig. 5.

From Fig. 6, we observe that the AMWT functions have a similar variation and have the same array of magnitude from the 1st day until the 9th day with the MPP peak amplitude of MPP(1500, 25) ≈ 6×10^{19} (Table 2). These minor changes are caused by several of phenomena, as presented in Table 1.

The MPP peak amplitude values of all days are given in Table 2.

The MPP peak amplitude values of Table 2 are obtained from Fig. 5. They are the maximum peak at the centre.

Table 2. *The MPP peak amplitude values*

Day	MPP peak amplitude
5	$(1500, 25) = 6.626733030945805\times10^{19}$
6	$(1500, 25) = 6.090234832595839\times10^{19}$
7	$(1500, 25) = 6.586669410632360\times10^{19}$
8	$(1500, 25) = 6.437468137514745\times10^{19}$
9	$(1500, 25) = 5.090191841432165\times10^{19}$
10	$(1500, 25) = 10.04842673892965\times10^{19}$
11	$(1500, 25) = 9.084636336550063\times10^{19}$
12	$(1500, 25) = 80.54631341778420\times10^{19}$

On the 10th day, the autocorrelation function is increased with an MPP peak amplitude of value MPP $(1500,25)=10.04842673892965\times10^{19}$.

This augmentation in MPP peak amplitude is the signature of the presence of the defect. This augmentation is caused by the progress of the peeling in the tooth N° 15/16 (Table 1).

On the 12th day, the evolution of the crack is in the whole of the entire width of tooth N° 15/16, and the MPP peak amplitude reaches the value of $\mathrm{MPP}(1500,25)=80.54631341778420\times10^{19}$.

Therefore, the autocorrelation function of the AMWT scalograms can detect early the defect.

4 CONCLUSION

In this paper, we have presented a contribution in the field of early diagnosis of gear systems to detect the defects in gear systems in the early stage. This contribution is a new approach to the early defect detection of gear systems. This approach is based on vibration analysis by the application of the AMWT. To prove the efficiency of this approach, simulation validation is given in the first part. Then, in the second part, the validation is done on a real system.

We have seen that the temporal and frequency representation cannot detect the defect in the early stage. However, the AMWT is an effective approach for detecting defects in gear reducers of the rotating machine.

In future work, we will investigate the proposed approach on a range of more representative data. Also, detecting the defect online is very suitable, and this aim will be the focalization of future work.

5 ACKNOWLEDGEMENTS

This research was supported by Algerian Ministry of Higher Education and Scientific Research (PRFU N°: A10N01UN100120220001). The authors gratefully acknowledge the support of CETIM, which provided the vibration signals.

6 REFERENCES

[1] Panić, B., Klemenc, J., Nagode, M. (2020). Gaussian mixture model based classification revisited: application to the bearing fault classification. *Strojniski vestnik - Journal of Mechanical Engineering*, vol. 66, no. 4, p. 215-226, **DOI:10.5545/sv-jme.2020.6563**.

[2] Pang, X., Cheng, B., Yang, Z., Li, F. (2019). A fault feature extraction method for a gearbox with a composite gear train based on EEMD and translation-invariant multiwavelet neighbouring coefficients. *Strojniski vestnik - Journal of Mechanical Engineering*, vol. 65, no. 1, p. 3-11, **DOI:10.5545/sv-jme.2018.5441**.

[3] Do, V.T., Nguyen, L.C. (2016). Adaptive empirical mode decomposition for bearing fault detection. *Strojniski vestnik - Journal of Mechanical Engineering*, vol. 62, no. 5, p. 281-290, **DOI:10.5545/sv-jme.2015.3079**.

[4] Ayad, M., Chikouche Dj., Boukezzoula, N., Rezki M. (2014). Search of a robust defect signature in gear systems across adaptive Morlet wavelet of vibration signals. *IET Signal Processing*, vol. 8, no. 9, p. 918-926, **DOI:10.1049/iet-spr.2013.0439**.

[5] He, L., Hao, L., Qiao, W. (2021). Remote monitoring and diagnostics of pitch bearing defects in a MW-scale wind turbine using pitch symmetrical-component analysis. *IEEE Transactions on Industry Applications*, vol. 57, no. 4, p. 3252-3261, **DOI:10.1109/TIA.2021.3079221**.

[6] Goyal, D., Dhami, S.S., Pabla, B.S. (2020). Non-contact fault diagnosis of bearings in machine learning environment. *IEEE Sensors Journal*, vol. 20, no. 9, p. 4816-4823, **DOI:10.1109/JSEN.2020.2964633**.

[7] Etz, R., Petreus, D., Frentiu, T., Patarau, T., Orian, C. (2015). An indirect method and equipment for temperature monitoring and control. *Advances in Electrical and Computer Engineering*, vol. 15, no. 4, p. 87-95, **DOI:10.4316/AECE.2015.04012**.

[8] de Oliveira A.K.V., Aghaei, M., Rüther, R. (2020). Aerial infrared thermography for low-cost and fast fault detection in utility-scale PV power plants. *Solar Energy*, vol. 211, p. 712-724. **DOI:10.1016/j.solener.2020.09.066**.

[9] Sun, J., Wang, L., Li, J., Li, F., Li, J., Lu, H. (2021). Online oil debris monitoring of rotating machinery: A detailed review of more than three decades. *Mechanical Systems and Signal Processing*, vol. 149, art. ID 107341, **DOI:10.1016/j.ymssp.2020.107341**.

[10] Sheng, S. (2016). Monitoring of wind turbine gearbox condition through oil and wear debris analysis: A full-scale testing perspective. *Tribology Transactions*, vol. 59, no. 1, p. 149-162, **DOI:10.1080/10402004.2015.1055621**.

[11] Yao, J., Liu, C., Song, K., Zhang, X., Jiang, D. (2021). Fault detection of complex planetary gearbox using acoustic signals. *Measurement*, vol. 178, art. ID 109428, **DOI:10.1016/j.measurement.2021.109428**.

[12] Glowacz, A. (2019). Fault detection of electric impact drills and coffee grinders using acoustic signals. *Sensors*, vol. 19, no. 2, p. 269, **DOI:10.3390/s19020269**.

[13] Matic, D., Kanovic, Z. (2017). Vibration based broken bar detection in induction machine for low load conditions. *Advances in Electrical and Computer Engineering*, vol. 17, no. 1, p. 49-54, **DOI:10.4316/AECE.2017.01007**.

[14] Xue, S., Howard, I. (2018). Torsional vibration signal analysis as a diagnostic tool for planetary gear fault detection. *Mechanical Systems and Signal Processing*, vol. 100, p. 706-728, **DOI:10.1016/j.ymssp.2017.07.038**.

[15] Wang, S., Zhu, Z.K., He, Y., Huang, W. (2010). Adaptive parameter identification based on morlet wavelet and application in gearbox fault feature detection. *EURASIP Journal on Advances in Signal Processing*, vol. 2010, art. ID 842879, **DOI:10.1155/2010/842879**.

[16] Daubechies, I. (1990). The wavelet Transform, time-frequency localisation and analysis. *IEEE Transactions on Information Theory*, vol. 36, no. 5, p. 961-1005, **DOI:10.1109/18.57199**.

[17] Olkkonen, H., Olkkonen, J.T. (2010). Shift-invariant B-spline wavelet transform for multi-scale analysis of neuroelectric signals. *IET Signal Processing*, vol. 4, no. 6, p. 603-609. **DOI:10.1049/iet-spr.2009.0109**.

[18] Al-Raheem, K.F., Roy, A., Ramachandran, K.P., Harrison, D.K., Grainger, S. (2009). Rolling element bearing faults diagnosis based on autocorrelation of optimized: wavelet de-noising technique. *The International Journal of Advanced Manufacturing Technology*, vol. 40, no. 3-4, p. 393-402, **DOI:10.1007/s00170-007-1330-3**.

[19] Kankar, P.K., Sharma, S.C., Harsha, S.P. (2013). Fault diagnosis of rolling element bearing using cyclic autocorrelation and wavelet transform. *Neurocomputing*, vol. 110, p. 9-17, **DOI:10.1016/j.neucom.2012.11.012**.

[20] McFadden, P.D. (1987). Examination of a technique for the early detection of failure in gears by signal processing of the time domain average of the meshing vibration. *Mechanical Systems and Signal Processing*, vol. 1, no. 2, p. 173-183, **DOI:10.1016/0888-3270(87)90069-0**.

[21] Yin, J., Wang, W., Man, Z., Khoo, S. (2014). Statistical modeling of gear vibration signals and its application to detecting and diagnosing gear faults. *Information Sciences*, vol. 259, p. 295-303, **DOI:10.1016/j.ins.2013.03.029**.

[22] Qin, Y., Mao, Y., Tang, B. (2013). Vibration signal component separation by iteratively using basis pursuit and its application in mechanical fault detection. *Journal of Sound and Vibration*, vol. 332, no. 20, p. 5217-5235, **DOI:10.1016/j.jsv.2013.04.021**.

[23] Man, Z., Wang, W., Khoo, S., Yin, J. (2012). Optimal sinusoidal modelling of gear mesh vibration signals for gear diagnosis and prognosis. *Mechanical Systems and Signal Processing*, vol. 33, p. 256-274, **DOI:10.1016/j.ymssp.2012.07.004**.

[24] Antoni, J., Randall, R.B. (2006). The spectral kurtosis: application to the vibration surveillance and diagnostics of rotating machines. *Mechanical Systems and Signal Processing*, vol. 20, no. 2, p. 308-331, **DOI:10.1016/j.ymssp.2004.09.002**.

[25] Ayad, M., Kebir, A., Rezki, M., Saoudi, K., Benziane, M., Arabi, A. (2019). Early fault detection of gear system based on Wavelet Packets Transform. *1st International Conference on Sustainable Renewable Energy Systems and Applications*, p. 1-6, **DOI:10.1109/ICSRESA49121.2019.9182269**.

List of reviewers who reviewed manuscripts in 2021

Arne Aalberg, Norway
Mohd Zamzuri Ab Rashid, Malaysia
Boris Aberšek, Slovenia
Wael G. Al-Kouz, Jordan
Mohamad Alsaadi, Turkey
Muhannad Al-Waily, Iraq
Miha Ambrož, Slovenia
Xabier Arrasate, Spain
Mohsen Asghari Ilani, Italy
Mohammed Asmael, Turkey
Maja Atanasijević-Kunc, Slovenia
Csobán Attila, Hungary
Gokhan Aydin, Turkey

Frank E. Baginski, USA
José M. Balthazar, Brazil
Mustapha Barakat, France
Sinan Basaran, Turkey
Christophe Batéjat, France
Michał Batsch, Poland
A.V. Benedetti, Brazil
Ali Cemal Benim, Germany
Anton Bergant, Slovenia
Ellen Bergseth, Sweden
Cristina Maria Biris, Romania
Miha Boltežar, Slovenia
Éd Claudio Bordinassi, Brazil
Drago Bračun, Slovenia
Miran Brezočnik, Slovenia
Vincenc Butala, Slovenia
Miroslav Byrtus, Czech Republic

Michele Calì, Italy
Mirco Daniel Chapetti, Argentina
Jianneng Chen, China
Peng Cheng, USA
S. J. Chu, South Korea
Marco Cirelli, Italy
Andre Luiz De Freitas Coelho, Brazil
Romina Conte, Italy
Giancarlo Cusimano, Italy

Gregor Čepon, Slovenia
Martin Česnik, Slovenia

José Gilberto Dalfré Filho, Brazil
Jos Darling, UK
Sayantan Das Banik, India
Luis Norberto López De Lacalle Marcaide, Spain
Anderson Paulo De Paiva, Brazil
Mariusz Deja, Poland
Tugce Demirdelen, Turkey
Hamed Aghajani Derazkola, Iran
Miha Dežman, Slovenia
Janez Diaci, Slovenia
Burak Dikici, Turkey
Saleemsab Doddamani, India
Oana Dodun, Romania
Maria Lúcia Duarte, Brazil
Matevž Dular, Slovenia

Ahmed Elkaseer, Germany
Andreas Endruweit, UK
SelcUK Erkaya, Turkey

Mousa Farhadi, Iran
Bogdan Filipič, Slovenia
Grzegorz Filo, Poland
Rudinei Fiorio, Belgium
Rastko Fišer, Slovenia
Regiane Fortes-Patella, France
Alfonso Fuentes-Aznar, USA

Roman Gabl, UK
S. Galván, México
Fermin Bañon Garcia, Spain
César García-Hernández, Spain
Adinel Gavrus, France
M. Barzegar Gerdroodbary, Iran
Girdu Constantin Cristinel Girdu, Romania
Srečko Glodež, Slovenia
Adam Glowacz, Poland
Arif Gok, Turkey
Miroslav Gombár, Slovak Republic
Guilherme Ferreira Gomes, Brazil
Ignacio Gonzalez-Perez, Spain
Chandrasekaran Gopalan, India
Darko Goričanec, Slovenia
Danijela Graćanin, Serbia
Damir Grguraš, Slovenia
Niccolí Grossi, Italy
Nenad Gubeljak, Slovenia
Leo Gusel, Slovenia

Sina Shaffiee Haghshenas, Iran
Miroslav Halilovič, Slovenia
Boštjan Harl, Slovenia
Edvard Höfler, Slovenia
Sheng Hong, China
Imre Horvath, The Netherlands
Richárd Horváth, Hungary
Evangelos Vasileios Hristoforou, Greece
Ahmed Hussien, Jordan

Jamshed Iqbal, KSA
Alireza Izadbakhsh, Iran

Jerzy Jackowski, Poland
Omid Jahanian, Iran
Karolis Janusevicius, Lithuania
Juan Carlos Jauregui, Mexico
Juliana Javorova, Bulgaria
Boris Jerman, Slovenia
Marko Jesenik, Slovenia
Matija Jezeršek, Slovenia
Wenming Jiang, China
Xiaoliang Jin, Canada
Elizabeth M. C. Jones, USA
Dragica Jošt, Slovenia

Shunmugesh K, India
Kamil Kahveci, Turkey
Wiktor Kamycki, Poland
Mitja Kastrevc, Slovenia
John D Kechagias, Greece
Marko Kegl, Slovenia
Tomaž Kek, Slovenia
Reda Khama, Algeria

Mohammad Khoshnevisan, USA
Jernej Klemenc, Slovenia
Peder Klit, Denmark
Damjan Klobčar, Slovenia
Pino Koc, Slovenia
Janez Kopač, Slovenia
Borut Kosec, Slovenia
Davorin Kramar, Slovenia
Rainer Krankenhagen, Germany
Grzegorz M. Krolczyk, Poland
Zbigniew Kulesza, Poland
Ashwani Kumar, India
Robert Kunc, Slovenia
Chil-Chyuan Kuo, Taiwan
Janez Kušar, Slovenia

Hojong Lee, USA
Stanislaw Legutko, Poland
Hirpa G. Lemu, Norway
Marco Lepidi, Italy
Zigang Li, China
Yaoyao Liao, China
Bin Lin, China
Alexander Lion, Germany
Jing Liu, China
Youyu Liu, China
Jing Liu, China
Gorazd Lojen, Slovenia
Franco Lombardi, Italy
Edgar López, Mexico
Darko Lovrec, Slovenia
Ivan Lukačević, Croatia

Alarico Macor, Italy
Tanja Mališ, Croatia
Angelos P. Markopoulos, Greece
Zoran Markov, Northern Macedonia
Jure Marn, Slovenia
Filipe Marques, Portugal
Edgar A. Martinez-Garcia, Mexico
Alberto Martini, Italy
Amirreza Masoodi, Iran
Parham Memarzadeh, Iran
M. Fernanda Mendoza-Petit, Spain
Giovanni Meneghetti, Iran
Paolo Mercorelli, Germany
Michal Michalec, Czech Republic
Andrzej Milecki, Poland
P. C. Mioralli, Brazil
Sergey Mironov, Russia
Majid Mirzaei, Iran
Bor Mojškerc, Slovenia
Nikolaj Mole, Slovenia
William Javier Mora Espinosa, Colombia
Mitja Morgut, Italy
Adrián Mota-Babiloni, Spain
Jorge Laureano Moya, Brazil
Jure Murovec, Slovenia

Milan Naď, Slovakia
Marko Nagode, Slovenia
Helena V. G. Navas, Portugal
Andreas Nestler, Germany
Phan Huu Nguyen, Vietnam
Anatolij Nikonov, Slovenia
Musa Norouzian, USA
Lovrenc Novak, Slovenia

Domen Ocepek, Slovenia
Milosav Ognjanović, Serbia
Ivan Okorn, Slovenia
Anna A. Okunkova, Russia
Remi Olatunbosun, UK
Stelian-Emilian Oltean, Romania
Simon Oman, Slovenia
Eneja Osterman, Slovenia
Sabri Ozturk, Turkey

Xinyu Pang, China
Gaioz Partskhaladze, Georgia
Farzad Pashmforoush, Iran
Neven Pavković, Croatia
Rok Pavlin, Slovenia
Kamran Pazand, Iran
Stanislav Pehan, Slovenia
G. Urbikain Pelayo, Spain
Tomaž Pepelnjak, Slovenia
Damian Pietrusiak, Poland
Giuseppe Pintaude, Brazil
Primož Podržaj, Slovenia
Pavel Polach, Czech Republic
Marko Polajnar, Slovenia
Martin Pollák, Slovak Republic
Primož Potočnik, Slovenia
Radu-Emil Precup, Romania
Andrej Predin, Slovenia
Jurij Prezelj, Slovenia
Slavica Prvulović, Serbia
Julius Caesar Puoza, China

Riad Ramadani, Albania
Daniel García-Pozuelo Ramos, Spain
Robert Randall, Australia
Fernando Sabino Fonteque Ribeiro, Brazil
Dario Richiedei, Italy
Samuel Rodman Oprešnik, Slovenia
Črtomir Rozman, Slovenia
Alessandro Ruggiero, Italy
Primož Rus, Slovenia
Riccardo Russo, Italy

Mohammad Reza Safaei, USA
Tadeusz Salacinski, Poland
Gürcan Samtaş, Turkey
Matekar B. Sanjay, India
Mile Savkovic, Serbia
Andrej Senegačnik, Slovenia
A. Senthilkumar, India
Silvio Simani, Italy
Vilmos Simon, Hungary
Anže Sitar, Slovenia
Luka Skrinjar, Slovenia
Janko Slavič, Slovenia
Lidija Slemenik Perše, Slovenia
Luigi Solazzi, Italy
M. Somasundaram, India
Chaosheng Song, China
Jussi Sopanen, Finland
Goncalo Sorger, Finland
Marco Sortino, Italy
Alina Spânu, Romania
Karsten Stahl, Germany
Bojan Starman, Slovenia
Janusz Steller, Poland
Uroš Stritih, Slovenia
Priyanka Sudhakara, India
Róbert Szabolcsi, Hungary
Kamil Szewerda, Poland

Božidar Šarler, Slovenia
Domen Šeruga, Slovenia
Marko Šimic, Slovenia
Brane Širok, Slovenia
Radislav Šmíd, Czech Republic
Roman Šturm, Slovenia

Saied Taheri, USA
Bernard Xavier Kouejou Tchomeni, South Africa
S. Thillikkani, India
Davood Toghraie, Iran
Sandino Torres, Ecuador
Jovan Trajkovski, Slovenia
Roman Trochimczuk, Poland
Tomasz Trzepiecinski, Poland
Paweł Turek, Poland

Faruk Ünker, Turkey

Miro Uran, Slovenia

Gautham V, India
Joško Valentinčič, Slovenia
Octavio Vázquez-Gómez, Mexico
Edgar Ernesto Vera Cardenas, Mexico
Peter Vidmar, Slovenia
Rok Vrabič, Slovenia
Nikola Vukašinović, Slovenia
Djordje Vukelic, Serbia
Željko Vukelič, Serbia

Shu Wang, USA
Xinwei Wang, China
Muhammad Waqas, Pakistan
Andrzej Wieczorek, Poland
Xi Wu, USA
Frederik Wulle, Germany

Zhao-Dong Xu, China

Metin Zeyveli, Turkey
Ying Zhang, China
Xingwei Zhen, China

Peter Zobec, Slovenia
Dejan Zupan, Slovenia
Matevž Zupančič, Slovenia
Franc Zupanič, Slovenia

Krzysztof Kamil Żur, Poland
Dragan Žeželj, Croatia
Uros Župerl, Slovenia
Urban Žvar Baškovič, Slovenia

The Editorial would like to thank all the reviewers in participating in reviewing process.
We appreciate the time and effort and greatly value the assistance as a manuscript reviewer for
Strojniški vestnik – Journal of Mechanical Engineering.

Vsebina

Strojniški vestnik - Journal of Mechanical Engineering
letnik 68, (2022), številka 1
Ljubljana, januar 2022
ISSN 0039-2480

Izhaja mesečno

Razširjeni povzetki (extended abstracts)

Strojniški vestnik - Journal of Mechanical Engineering 68(2022)1, SI 3

Prejeto v recenzijo: 2021-07-14
Prejeto popravljeno:2021-09-29
Odobreno za objavo:2021-12-16

Vključitev poenostavljenega modela mehanskega spoja v numerično analizo

Mitja Glavan[1] — Jernej Klemenc[2] — Vili Malnarič[1] — Domen Šeruga[2,*]
[1] TPV Automotive, Slovenija
[2] Univerza v Ljubljani, Fakulteta za strojništvo, Slovenija

Trenutni trend v avtomobilski, letalski, navtični in drugih podobnih panogah je predvsem zmanjševanje porabe gradiva in posredno zmanjševanje mase prevoznih sredstev. V tem pogledu se danes za konstruiranje vse pogosteje pojavljajo tako imenovana lahka gradiva, kot so visokotrdnostno jeklo, aluminijeve zlitine, kompozitna gradiva in magnezijeve zlitine. Vendar pa zaradi različnih lastnosti teh gradiv njihovo spajanje s tradicionalnimi postopki varjenja ni možno. Danes je zato v uporabi veliko število alternativnih tehnologij spajanja, vsaka pa ima svoje prednosti in slabosti. Uporaba določene tehnologije je torej odvisna od zahtev glede trdnosti končnega izdelka, uporabljenih gradiv, možnosti integracije v proizvodne zmogljivosti in cene.

V raziskavi smo primerjali dve tehnologiji spajanja, ki predstavljata alternativo točkovnemu varjenju. Samorezno kovičenje je tehnologija, ki zagotavlja primerljivo statično trdnost in nekoliko večjo dinamično trdnost v primerjavi s točkovnim varjenjem, medtem ko je prednost zagozdnega spoja bistveno večja dinamična trdnost z izgubo znatnega deleža statične trdnosti.

Za poenostavljeno upoštevanje teh tehnologij v numeričnih analizah v predrazvojnih in razvojnih fazah konstrukcijsko-razvojnega procesa je potrebno razviti ustrezne numerične modele spojev. Poznavanje natančnih parametrov numeričnih modelov spojev prispeva k zmanjšanju razvojnih stroškov, krajšim razvojnim časom in optimizaciji geometrije izdelka pred izdelavo prvega prototipa. Spoji so bili izvedeni na jekleni pločevini S500MC debeline 2 mm. Uporabili smo samorezne kovice premera 5 mm, pri izdelavi zagozdnega spoja pa smo uporabili orodje premera 8 mm. Glede na zahteve standarda DVS/EFB 3480-1 so preizkušanci imeli dve obliki za vnašanje strižnih, odlupnih in kombiniranih obremenitev. Izvedli smo fizikalne preizkuse statične trdnosti spojev na preizkuševališču Zwick/Roell Z150. Na vsakem obremenitvenem nivoju smo zagotovili petkratno ponovitev preizkusa. Za izgradnjo poenostavljenega numeričnega modela z metodo končnih elementov smo uporabili programsko okolje Simulia Abaqus. Pločevine smo modelirali z lupinskimi elementi, spoj pa z linijskimi elementi, ki povezujejo pločevini. Pri velikosti in kakovosti mreže končnih elementov smo sledili industrijskim zahtevam za simulacije trka. Lastnosti pločevin smo popisali z bilinearno napetostno-deformacijsko krivuljo, prav tako pa je bil linijskim elementom dodeljen bilinearen materialni model ter okrogel prerez ustreznega premera.

Vendar pa so se parametri bilinearnih elastoplastičnih lastnosti spoja razlikovali od dejanskih materialnih lastnosti za jekleno pločevino S500 MC in so bolj predstavljali njegov fizični odziv pri obremenjevanju. Vse posebnosti mehanskega spoja so bile torej integrirane in predstavljene z njegovo bilinearno značilnostjo. Parametre mehanskih spojev za potrebe numeričnih analiz smo ocenili z optimizacijsko metodo, ki združuje uporabo metode odzivne površine, rezultate simulacij, rezultate fizikalnih preizkusov in genetski algoritem.

Rezultate simulacij z uporabo optimalnih vrednosti parametrov numeričnih modelov spojev smo nato primerljali z eksperimentalnimi opažanji za oba analizirana spoja.

Opazili smo, da je s predstavljeno metodologijo mogoče simulirati odziv analiziranih mehanskih spojev, predstavljajo pa optimalne vrednosti parametrov spojev vedno kompromis med kakovostjo prileganja eksperimentalnim opažanjem in množico analiziranih obremenitev.

Ključne besede: kovičenje, mehanski spoji, samorezno kovičenje, zagozdni spoj, metoda končnih elementov, optimizacija parametrov, odzivna površina, genetski algoritem

---

*Naslov avtorja za dopisovanje: Univerza v Ljubljani, Fakulteta za strojništvo, Aškerčeva 6, 1000 Ljubljana, Slovenija, domen.seruga@fs.uni-lj.si

Strojniški vestnik - Journal of Mechanical Engineering 68(2022)1, SI 4

Prejeto v recenzijo: 2021-08-08
Prejeto popravljeno: 2021-10-11
Odobreno za objavo: 2021-11-29

Adaptivni robot za mašenje netesnosti na cevovodih: raziskava oprijema in zmogljivosti prečkanja ovir

Hongwei Yan[1,*] – Jian Li[1] – Ziming Kou[2] – Yi Liu[1] – Pengcheng Li[1] – Lu Wang[1]
[1]Kitajska severna univerza, Šola za strojništvo, Kitajska
[2]Tehniška univerza v Taiyuanu, Kolidž za strojništvo in transport, Kitajska

Večina prenosnih cevovodov je zakopanih pod zemljo zaradi zaščite pred zunanjimi dejavniki. Postopek odprave netesnosti na podzemnih cevovodih vključuje odkopavanje, iskanje mest netesnosti ter zapiranje in popravilo po sekcijah. Pri tem se pojavljajo težave z iskanjem netesnosti, omejenim prostorom za ročno delo itn. V pričujoči študiji je bil raziskan adaptivni robot za mašenje netesnosti na cevovodih, ki lahko opravlja naloge iskanja, mašenja in hitrega popravila poškodb. Robot hitro zamaši in popravi poškodbo, s tem pa zagotovi nemoten transport nafte oz. plina in prepreči širjenje luknje. Robot mora biti zmožen stabilnega premikanja po cevovodu in prečkanja ovir do določene višine.

Z raziskavami trga in pregledom literature so bile določene minimalne zahteve za projektiranje, nato pa je bil oblikovan tridimenzionalni model robota. Način delovanja in sestavi oz. enote robota so bili izbrani tako, da je robot izpolnil cilje raziskave. Z analizo sil na modelu je bilo preučeno optimalno stanje delovanja robota v cevovodu, kakor tudi glavni dejavniki, ki vplivajo na prečkanje ovir. S teoretično analizo je bil preučen vpliv različnih dejavnikov na zmogljivost prečkanja ovir. Prečkanje je bilo analizirano s simulacijami in z eksperimentalno verifikacijo. Opredeljeno je optimalno delovanje robota in določena je največja višina ovire, ki jo ta lahko prečka.

V jedru članka so podani konstrukcija robota za mašenje netesnosti z vijačnim pogonom, analiza in raziskava dejavnikov, ki vplivajo na prečkanje ovir, in najboljše stanje delovanja.

Postavljen je model prečkanja ovir z geometrijsko analizo. Ugotovljena je bila pozitivna korelacija med pogonskim kolesom in zmožnostjo prečkanja ovir. Z dinamično analizo in povezano mehaniko sta bili preučeni stabilnost gibanja in zmogljivost prečkanja ovir. Za uspešnejše prečkanje ovir je mogoče spremeniti velikost pogonskega kota, če pogonsko kolo ne zdrsne.

Članek zaradi omejenega prostora analizira samo zmogljivost prečkanja ovir in najboljše stanje delovanja robota v ravnih cevovodih. Poudarjen je vpliv odklonskega kota na način delovanja robota. Roboti se bodo med gibanjem po cevovodih srečevali z različnimi oblikami. Pogonsko kolo na eni strani tako denimo ob prehodu skozi T-kos obvisi v zraku, kar pomembno vpliva na gibanje robota. Vplivi takih stanj pogonskih koles na gibanje in na funkcijske odvisnosti bodo predmet prihodnjih raziskav.

Z zasnovo robota za mašenje cevovodov z več neodvisnimi enotami se izboljša prilagodljivost posameznih komponent. Robot je primeren za zaznavanje netesnosti v cevovodih in pametno ukrepanje v nuji. V primeru netesnosti lahko hitro zapre in popravi mesto puščanja za neprekinjen tok nafte in plina, odprtina pa se ne širi. Kot vijačnice pogonskega kolesa upravlja poseben krmilni modul, s čimer se izboljšata vodljivost gibanja in stabilnost sistema. Zasnova adaptivnega robota za mašenje podzemnih cevovodov je pomemben prispevek k raziskavam in razvoju opreme za preprečevanje in nadzor netesnosti cevovodov.

Ključne besede: netesnost cevovoda, robot za mašenje, prečkanje ovir, optimalen pogonski kot, analiza s simulacijo

---

*Naslov avtorja za dopisovanje: Kitajska severna univerza, Šola za strojništvo, Kitajska, aweigeyan@nuc.edu.cn

Strojniški vestnik - Journal of Mechanical Engineering 68(2022)1, SI 5

Prejeto v recenzijo: 2021-06-11
Prejeto popravljeno: 2021-11-06
Odobreno za objavo: 2021-12-06

Odkrivanje napak na zunanji steni jeklenih cevi s tehniko testiranja z vrtinčnimi tokovi, ki nastanejo pod vplivom vrtilnega magnetnega polja (RoFEC)

Xiaokang Yin* – Zhuoyong Gu – Wei Wang – Xiaorui Zhang – Xin'an Yuan –Wei Li – Guoming Chen
Središče za konstrukcije na morju in varnostno tehniko, Kitajska univerza za nafto, Kitajska

Tehnika testiranja z vrtinčnimi tokovi, ki nastanejo pod vplivom vrtilnega elektromagnetnega polja (RoFEC), je v zadnjih letih pritegnila veliko pozornosti zaradi mnogih prednosti, ki jih ponuja pri kontroli cevnih konstrukcij. Večina objavljenih raziskav obravnava odkrivanje napak na notranji steni kovinskih cevi z vstavnimi sondami, ki pa niso vedno primerne za iskanje napak na zunanjih stenah. V članku je opisana tehnika RoFEC za preiskave s pomikom preizkušanca skozi instrument in njena uporabnost za odkrivanje napak na zunanji steni cevi.

Predstavljeno je osnovno načelo delovanja tehnike RoFEC s pomikom preizkušanca skozi instrument. V paketu COMSOL je bil zgrajen tridimenzionalni model po metodi končnih elementov za analizo porazdelitve vrtilnega elektromagnetnega polja ter preučevanje interakcij med napakami in vrtinčnimi tokovi. Za karakteristični signal je bila izbrana aksialna komponenta magnetnega polja, ki nastane zaradi napake. Pridobljena je bila iz modelov za analizo vplivnih dejavnikov pri odkrivanju napak, kot so naklon cevi, obodni položaj ter orientacija in velikost napak. Zasnovan je bil sistem RoFEC s šestimi vzbujalnimi navitji in eno tipalno tuljavo, ki je bil nato uporabljen za kontrolo jeklene cevi z napakami v aksialni in obodni orientaciji.

Glavne raziskovalne metode so bile modeliranje s končnimi elementi, analiza elektromagnetnega polja, analiza impedančne ravnine in eksperimentalna verifikacija.

Modeli po MKE so pokazali pomemben vpliv nagiba cevi, obodnega položaja napak ter orientacije in velikosti napak na zmogljivost kontrole. Zgrajen je bil sistem RoFEC za verifikacijo rezultatov analize po MKE. Rezultati eksperimentov so pokazali, da tehnika RoFEC učinkovito odkriva aksialne in obodne napake. Pri različnih položajih napak na obodu je mogoče uporabiti kot Lissajousovega vzorca v impedančni ravnini za določitev točnega mesta napake. Za razliko od obstoječih pristopov pri testiranju RoFEC s sondo v cevi, ki so namenjeni kontroli cevi iz neželeznih materialov, je opisana tehnika RoFEC namenjena cevem iz ogljikovega jekla. To je magnetno permeabilen material, ki se ga je težje lotiti s tehnikami na osnovi vrtinčnih tokov. Druga velika razlika med skoznjim in vstavnim sistemom je v enojni tipalni tuljavi. Ta je v obeh primerih samo ena, razlika pa je v premeru. Pri vstavni sondi mora biti tuljava čim bližje notranji steni zaradi odprave vpliva spremenljive oddaljenosti na meritve, medtem ko je premer tuljave pri skoznjem sistemu stvar izvedbe. Rešitev s tuljavo blizu zunanje stene cevi ni nujno optimalna.

Članek predstavlja uporabnost tehnike RoFEC, ki je trenutno v zgodnji fazi razvoja. Instrument bo treba še občutno izboljšati za odkrivanje in kvantifikacijo drobnih napak. V prihodnjih študijah bo mogoče razdelati konstrukcijo sistema in druge vplivne dejavnike, npr. oddaljenost vzbujalnih navitij od preizkušanca, premer tipalne tuljave, vrtinčni tok, induciran z gibanjem, in variabilno permeabilnost zaradi izmeničnega magnetnega polja.

Članek predstavlja tehniko RoFEC za odkrivanje napak v zunanji steni jeklenih cevi, sistematično analizo vplivnih dejavnikov in razvoj sistema za kontrolo. Skoznja tehnika RoFEC je potencialno uporabna za industrijo nafte in plina za kontrolo navitih cevi med obratovanjem.

Ključne besede: neporušne preiskave, vrtilno elektromagnetno polje, vrtinčni tok, modeliranje s končnimi elementi, vplivni dejavniki, skoznji instrument, mesto napake

---

*Naslov avtorja za dopisovanje: Središče za konstrukcije na morju in varnostno tehniko, Kitajska univerza za nafto, 66 West Changjiang Road, Qingdao, Kitajska, Xiaokang.yin@upc.edu.cn

Strojniški vestnik - Journal of Mechanical Engineering 68(2022)1, SI 6

Prejeto v recenzijo: 2021-07-14
Prejeto popravljeno: 2021-10-01
Odobreno za objavo: 2021-12-07

Raziskava metode za sprotno vrednotenje zanesljivosti v kombinaciji z diagnosticiranjem napak na primeru podvodnega električnega božičnega drevesa

Peng Liu – Dagang Shen – Jinfeng Cao*
Tehniška univerza v Čingdau, Šola za strojništvo in avtomobilsko tehniko, Kitajska

Podvodna električna božična drevesa (glava vrtine, XT) so pomemben del opreme in na nekaterih področjih tudi edina rešitev za pridobivanje nafte in plina na morju. Morski ekosistemi so krhki in v primeru razlitja nafte lahko nastopijo nepovračljive posledice. Za varno pridobivanje nafte in plina na morju so zato nujni stroga analiza in ukrepi za zagotavljanje zanesljivosti še pred prevzemom tovrstne opreme v obratovanje.

V članku je podan predlog za sprotno vrednotenje zanesljivosti mehanskega podsistema električnih božičnih dreves skupaj z diagnosticiranjem napak s statičnim Bayesovim omrežjem. Metoda zagotavlja identifikacijo vrste napak na komponentah in sprotno vrednotenje zanesljivosti mehanskega podsistema pri različnih stopnjah odpovedi komponent. Z analizo občutljivosti ocene zanesljivosti mehanskega sistema na osnovi skupnih informacij je podan tudi vpliv dogodkov posameznih komponent na zanesljivost sistema.

Rezultati so pokazali, da interval časovnih rezin le malo vpliva na vrednotenje zanesljivosti mehanskega podsistema božičnega drevesa, saj je trend zanesljivosti ne glede na interval praktično enak. Varnostne odpovedi imajo določen vpliv na postopno upadanje zanesljivosti mehanskega podsistema. Ta se po 5000 urah neprekinjenega obratovanja zmanjša na 95 %. Čas razkritja varnostne odpovedi je imel večji vpliv na rezultate vrednotenja zanesljivosti mehanskega podsistema in zato je priporočeno izvajanje te metode za identifikacijo in diagnostiko napak ter sprotno vrednotenje zanesljivosti mehanskega sistema na vsakih 1000 h. Analiza občutljivosti je pokazala, da imajo pri daljšem času obratovanja sistema večji vpliv na zanesljivost sistema komponente v proizvodni zanki, medtem ko je bil vpliv komponent v zanki za vbrizgavanje kemikalij manjši. Verjetnost odpovedi komponent v proizvodni zanki zato terja večjo pozornost med dolgotrajnim obratovanjem.

Prispevek članka je metoda za integracijo vrednotenja zanesljivosti s sprotno diagnostiko napak ob uporabi dinamičnih Bayesovih omrežij. Metoda omogoča identifikacijo vrst napak na komponentah in sprotno vrednotenje zanesljivosti mehanskega podsistema pri različnih stopnjah odpovedi komponent na morju. S tem je odpravljena težava zaradi nenatančnosti rezultatov vrednotenja, ki je povezana z upoštevanjem zgolj stopnje degradacije komponent ali uporabo zgolj senzorskih podatkov. Predlagana metoda je pomembno teoretično orodje za vzdrževanje mehanskega podsistema električnih božičnih dreves in jo bo v prihodnje mogoče razširiti za vrednotenje zanesljivosti vseh podvodnih proizvodnih sistemov.

Ključne besede: električno božično drevo, analiza zanesljivosti, Bayesovo omrežje, diagnostika napak, vrednotenje zanesljivosti, analiza občutljivosti

---

*Naslov avtorja za dopisovanje: Tehniška univerza v Čingdau, Šola za strojništvo in avtomobilsko tehniko, Jialingjiang East Road No. 777, Qingdao, Kitajska, caojinfeng@qut.edu.cn

Strojniški vestnik - Journal of Mechanical Engineering 68(2022)1, SI 7
© 2022 Avtorji. CC BY-NC 4.0 Int.

Prejeto v recenzijo: 2021-08-31
Prejeto popravljeno: 2021-11-02
Odobreno za objavo: 2021-12-06

Zgodnje odkrivanje okvar na zobniških prenosnikih z Morletovo valčno transformacijo

Mouloud Ayad[1,2] – Kamel Saoudi[1,2] – Mohamed Rezki[1] – Mourad Benziane[1,2] – Abderrazak Arabi[3]

[1] Univerza v Bouiri, Fakulteta za znanost in aplikativne vede, Alžirija
[2] Univerza v Bouiri, Laboratorij LPM3E, Alžirija
[3] Univerza v Sétifu, Laboratorij LIS, Alžirija

Pričujoči članek predstavlja prispevek na področju zgodnjega diagnosticiranja okvar na zobniških prenosnikih.

Nadzor nad industrijskimi sistemi je danes ključnega pomena, z napovedovanjem okvar pa se je mogoče izogniti številnim težavam. Če napake niso odkrite v dovolj zgodnji fazi, se degradiranje sistema nadaljuje, kar lahko privede do velike gospodarske škode. Okvare v industrijskih sistemih vplivajo na vedenje in na lastnosti signalov vibracij. Take spremembe so znamenje za prisotnost okvar. Izziv predstavlja zgodnje odkrivanje vzorcev sprememb, saj so signali vibracij močno obremenjeni s šumom, nestacionarni in nelinearni.

Podan je predlog metode za iskanje vzorcev okvar z analizo signalov vibracij na osnovi avtokorelacije Morletovih valčnih transformacij (AMWT). Pristop je bil najprej uporabljen na simuliranih signalih in nato še na realnih signalih iz eksperimentalnega zobniškega prenosnika. Najprej je opisano teoretično ozadje metode AMWT, temu pa sledi njena validacija s simulacijami. Končno so podani rezultati in validacija pristopa na realnem sistemu.

Učinkovitost metode AMWT je bila ovrednotena s signali realnega zobniškega prenosnika, ki ga sestavljata zobnika z 20 in 21 zobmi. Sistem je obratoval 11 dni v nespremenjenih pogojih, vsak dan pa je bil pregledan in izdelano je bilo poročilo o stanju sistema.

Signali vibracij v časovni domeni in pripadajoči frekvenčni spektri prvih 11 dni ne nakazujejo prisotnosti okvar. Od prvega do enajstega dne so si signali vibracij v časovni domeni podobni, dvanajsti dan pa je prišlo do spremembe zaradi poškodbe na zobu. Iz signalov v časovni in frekvenčni domeni je bilo okvaro mogoče diagnosticirati šele zadnji (dvanajsti) dan, zato je za zgodnje odkrivanje okvar potreben drugačen pristop.

Morletova valčna transformacija ima od prvega do devetega dne na skalogramih podobno variabilnost in amplitudo. Deseti dan pa je nastopilo povečanje avtokorelacijske funkcije, ki je znamenje za prisotnost okvare. Avtokorelacijska funkcija na skalogramih AMWT je zato uporabna za zgodnje odkrivanje napak.

Prispevek in novost članka je v uporabi avtokorelacije na Morletovi valčni transformaciji. Glede na objavljeno literaturo gre za nov pristop.

Ključne besede: avtokorelacija Morletovih valčnih transformacij, zgodnje diagnosticiranje napak, zobniški prenosniki, analiza vibracij, skalogrami

---

*Naslov avtorja za dopisovanje: Univerza v Bouiri, 1000, Bouira, Alžirija, m.ayad@univ-bouira.dz

Guide for Authors

All manuscripts must be in English. Pages should be numbered sequentially. The manuscript should be composed in accordance with the Article Template given above. The suggested length of contributions is 10 to 20 pages. Longer contributions will only be accepted if authors provide justification in a cover letter. For full instructions see the Information for Authors section on the journal's website: http://en.sv-jme.eu .

SUBMISSION:

Submission to SV-JME is made with the implicit understanding that neither the manuscript nor the essence of its content has been published previously either in whole or in part and that it is not being considered for publication elsewhere. All the listed authors should have agreed on the content and the corresponding (submitting) author is responsible for having ensured that this agreement has been reached. The acceptance of an article is based entirely on its scientific merit, as judged by peer review. Scientific articles comprising simulations only will not be accepted for publication; simulations must be accompanied by experimental results carried out to confirm or deny the accuracy of the simulation. Every manuscript submitted to the SV-JME undergoes a peer-review process.

The authors are kindly invited to submit the paper through our web site: http://ojs.sv-jme.eu. The Author is able to track the submission through the editorial process - as well as participate in the copyediting and proofreading of submissions accepted for publication - by logging in, and using the username and password provided.

SUBMISSION CONTENT:

The typical submission material consists of:

- A **manuscript** (A PDF file, with title, all authors with affiliations, abstract, keywords, highlights, inserted figures and tables and references),
- Supplementary files:
  - a **manuscript** in a WORD file format
  - a **cover letter** (please see instructions for composing the cover letter)
  - a ZIP file containing **figures** in high resolution in one of the graphical formats (please see instructions for preparing the figure files)
  - possible **appendicies** (optional), cover materials, video materials, etc.

Incomplete or improperly prepared submissions will be rejected with explanatory comments provided. In this case we will kindly ask the authors to carefully read the Information for Authors and to resubmit their manuscripts taking into consideration our comments.

COVER LETTER INSTRUCTIONS:

Please add a **cover letter** stating the following information about the submitted paper:

1. Paper **title**, list of **authors** and their **affiliations**. **One** corresponding author should be provided.
2. **Type of paper**: original scientific paper (1.01), review scientific paper (1.02) or short scientific paper (1.03).
3. A **declaration** that neither the manuscript nor the essence of its content has been published in whole or in part previously and that it is not being considered for publication elsewhere.
4. State the **value of the paper** or its practical, theoretical and scientific implications. What is new in the paper with respect to the state-of-the-art in the published papers? Do not repeat the content of your abstract for this purpose.
5. We kindly ask you to suggest at least two **reviewers** for your paper and give us their names, their full affiliation and contact information, and their scientific research interest. The suggested reviewers should have at least two relevant references (with an impact factor) to the scientific field concerned; they should not be from the same country as the authors and should have no close connection with the authors.

FORMAT OF THE MANUSCRIPT:

The manuscript should be composed in accordance with the Article Template. The manuscript should be written in the following format:

- A **Title** that adequately describes the content of the manuscript.
- A list of **Authors** and their **affiliations**.
- An **Abstract** that should not exceed 250 words. The Abstract should state the principal objectives and the scope of the investigation, as well as the methodology employed. It should summarize the results and state the principal conclusions.
- 4 to 6 significant **key words** should follow the abstract to aid indexing.
- 4 to 6 **highlights;** a short collection of bullet points that convey the core findings and provide readers with a quick textual overview of the article. These four to six bullet points should describe the essence of the research (e.g. results or conclusions) and highlight what is distinctive about it.
- An **Introduction** that should provide a review of recent literature and sufficient background information to allow the results of the article to be understood and evaluated.
- A **Methods** section detailing the theoretical or experimental methods used.
- An **Experimental section** that should provide details of the experimental set-up and the methods used to obtain the results.
- A **Results** section that should clearly and concisely present the data, using figures and tables where appropriate.
- A **Discussion** section that should describe the relationships and generalizations shown by the results and discuss the significance of the results, making comparisons with previously published work. (It may be appropriate to combine the Results and Discussion sections into a single section to improve clarity.)
- A **Conclusions** section that should present one or more conclusions drawn from the results and subsequent discussion and should not duplicate the Abstract.
- **Acknowledgement** (optional) of collaboration or preparation assistance may be included. Please note the source of funding for the research.
- **Nomenclature** (optional). Papers with many symbols should have a nomenclature that defines all symbols with units, inserted above the references. If one is used, it must contain all the symbols used in the manuscript and the definitions should not be repeated in the text. In all cases, identify the symbols used if they are not widely recognized in the profession. Define acronyms in the text, not in the nomenclature.
- **References** must be cited consecutively in the text using square brackets [1] and collected together in a reference list at the end of the manuscript.
- **Appendix(-icies)** if any.

SPECIAL NOTES

Units: The SI system of units for nomenclature, symbols and abbreviations should be followed closely. Symbols for physical quantities in the text should be written in italics (e.g. *v*, *T*, *n*, etc.). Symbols for units that consist of letters should be in plain text (e.g. ms^{-1}, K, min, mm, etc.). Please also see: http://physics.nist.gov/cuu/pdf/sp811.pdf .

Abbreviations should be spelt out in full on first appearance followed by the abbreviation in parentheses, e.g. variable time geometry (VTG). The meaning of symbols and units belonging to symbols should be explained in each case or cited in a **nomenclature** section at the end of the manuscript before the References.

Figures (figures, graphs, illustrations digital images, photographs) must be cited in consecutive numerical order in the text and referred to in both the text and the captions as Fig. 1, Fig. 2, etc. Figures should be prepared without borders and on white grounding and should be sent separately in their original formats. If a figure is composed of several parts, please mark each part with a), b), c), etc. and provide an explanation for each part in Figure caption. The caption should be self-explanatory. Letters and numbers should be readable (Arial or Times New Roman, min 6 pt with equal sizes and fonts in all figures). Graphics (submitted as supplementary files) may be exported in resolution good enough for printing (min. 300 dpi) in any common format, e.g. TIFF, BMP or JPG, PDF and should be named Fig1.jpg, Fig2.tif, etc. However, graphs and line drawings should be prepared as vector images, e.g. CDR, AI. Multi-curve graphs should have individual curves marked with a symbol or otherwise provide distinguishing differences using, for example, different thicknesses or dashing.

Tables should carry separate titles and must be numbered in consecutive numerical order in the text and referred to in both the text and the captions as Table 1, Table 2, etc. In addition to the physical quantities, such as *t* (in italics), the units [s] (normal text) should be added in square brackets. Tables should not duplicate data found elsewhere in the manuscript. Tables should be prepared using a table editor and not inserted as a graphic.

REFERENCES:

A reference list must be included using the following information as a guide. Only cited text references are to be included. Each reference is to be referred to in the text by a number enclosed in a square bracket (i.e. [3] or [2] to [4] for more references; do not combine more than 3 references, explain each). No reference to the author is necessary.

References must be numbered and ordered according to where they are first mentioned in the paper, not alphabetically. All references must be complete and accurate. Please add DOI code when available. Examples follow.

Journal Papers:

Surname 1, Initials, Surname 2, Initials (year). Title. *Journal*, volume, number, pages, DOI code.

[1] Hackenschmidt, R., Alber-Laukant, B., Rieg, F. (2010). Simulating nonlinear materials under centrifugal forces by using intelligent cross-linked simulations. *Strojniški vestnik - Journal of Mechanical Engineering,* vol. 57, no. 7-8, p. 531-538, DOI:10.5545/sv-jme.2011.013.

Journal titles should not be abbreviated. Note that journal title is set in italics.

Books:

Surname 1, Initials, Surname 2, Initials (year). Title. Publisher, place of publication.

[2] Groover, M.P. (2007). *Fundamentals of Modern Manufacturing*. John Wiley & Sons, Hoboken.

Note that the title of the book is italicized.

Chapters in Books:

Surname 1, Initials, Surname 2, Initials (year). Chapter title. Editor(s) of book, book title. Publisher, place of publication, pages.

[3] Carbone, G., Ceccarelli, M. (2005). Legged robotic systems. Kordić, V., Lazinica, A., Merdan, M. (Eds.), Cutting Edge Robotics. Pro literatur Verlag, Mammendorf, p. 553-576.

Proceedings Papers:

Surname 1, Initials, Surname 2, Initials (year). Paper title. Proceedings title, pages.

[4] Štefanić, N., Martinčević-Mikić, S., Tošanović, N. (2009). Applied lean system in process industry. *MOTSP Conference Proceedings*, p. 422-427.

Standards:

Standard-Code (year). Title. Organisation. Place.

[5] ISO/DIS 16000-6.2:2002. *Indoor Air – Part 6: Determination of Volatile Organic Compounds in Indoor and Chamber Air by Active Sampling on TENAX TA Sorbent, Thermal Desorption and Gas Chromatography using MSD/FID.* International Organization for Standardization. Geneva.

WWW pages:

Surname, Initials or Company name. Title, from http://address, date of access.

[6] Rockwell Automation. Arena, from *http://www.arenasimulation.com,* accessed on 2009-09-07.

EXTENDED ABSTRACT:

When the paper is accepted for publishing, the authors will be requested to send an **extended abstract** (approx. one A4 page or 3500 to 4000 characters or approx. 600 words). The instruction for composing the extended abstract are published on-line: http://www.sv-jme.eu/information-for-authors/ .

COPYRIGHT:

Authors submitting a manuscript do so on the understanding that the work has not been published before, is not being considered for publication elsewhere and has been read and approved by all authors. The submission of the manuscript by the authors means that the authors automatically agree to publish the paper uder CC-BY 4.0 Int. or CC-BY-NC 4.0 Int. when the manuscript is accepted for publication. All accepted manuscripts must be accompanied by a Copyright Agreement, which should be sent to the editor. The work should be original work by the authors and not be published elsewhere in any language without the written consent of the publisher. The proof will be sent to the author showing the final layout of the article. Proof correction must be minimal and executed quickly. Thus it is essential that manuscripts are accurate when submitted. Authors can track the status of their accepted articles on https://en.sv-jme.eu/.

PUBLICATION FEE:

Authors will be asked to pay a publication fee for each article prior to the article appearing in the journal. However, this fee only needs to be paid after the article has been accepted for publishing. The fee is 380 EUR (for articles with maximum of 6 pages), 470 EUR (for articles with maximum of 10 pages), plus 50 EUR for each additional page. The additional cost for a color page is 90.00 EUR (only for a journal hard copy; optional upon author's request). These fees do not include tax.

Strojniški vestnik -Journal of Mechanical Engineering
Aškerčeva 6, 1000 Ljubljana, Slovenia, e-mail: info@sv-jme.eu

9 770039 248001
ISSN 0039-2480

http://www.sv-jme.eu

Contents

Papers